A FORCE SENSING INSOLE TO QUANTIFY IMPACT LOADING TO THE FOOT

DEVELOPMENT OF A FORCE SENSING INSOLE TO QUANTIFY IMPACT LOADING TO THE FOOT IN VARIOUS POSTURES

By JOHN VAN TUYL, B.A.Sc.

A Thesis Submitted to the School of Graduate Studies in Partial Fulfilment of the Requirements for the Degree Master of Applied Science

McMaster University © Copyright by John Van Tuyl (2014)

McMaster University Master of Applied Science (2014) Hamilton, Ontario (Mechanical Engineering)

Title: Development of a force sensing insole to quantify impact loading to the foot in various postures

Author: John Van Tuyl, B.A.Sc.

Supervisor: Cheryl E. Quenneville, B.A.Sc., M.A.Sc., Ph.D

Pages: xviii, 165

ABSTRACT

Lower leg injuries commonly occur in both automobile accidents and underbody explosive blasts, which can be experienced in war by mounted soldiers. These injuries are associated with high morbidity. Accurate methods to predict these injuries, especially in the foot and ankle, must be developed to facilitate the testing and improvement of vehicle safety systems.

Anthropomorphic Test Devices (ATDs) are one of the tools used to assess injury risk. These mimic the behavior of the human body in a crash while recording data from sensors in the ATD. Injury criteria for the lower leg have been developed with testing of the leg in a neutral posture, but initial posture may affect the likelihood of lower leg injury.

In this thesis, the influence of initial posture on key injury assessment criteria used in crash testing with ATDs was examined. It was determined that these criteria are influenced by ATD leg posture, but further work is necessary to determine if the changes in outcome correspond to altered injury risk in humans when the ankle is in the same postures.

In order to better quantify the forces acting on various areas of the foot and correlate those with injury, allowing for development of new criteria, a purpose built force sensor was created. An array of these sensors was incorporated into a boot and used to instrument an ATD leg during impact testing. The sensors provided useful information

regarding the force distribution across the sole of the foot during an impact. A numerical simulation of the active material in the sensor was also created to better understand the effect of shear loading on the sensor.

This work furthers the understanding of lower leg injury prediction and develops a tool which may be useful in developing accurate injury criteria for the foot and lower leg.

ACKNOWLEDGMENTS

Kelly and Mum were supportive through the winds, storms, and doldrums I encountered during this voyage into academia. They are important to me.

I appreciate the guidance of Dr. Quenneville and Dr. Wohl throughout this project. Dr. Quenneville provided feedback and good advice. She read so many drafts, but still corrected my statistically anomalous tendency to use the wrong word without letting it affect (effect?) her. Dr. Wohl has given me many a pep talk or bit of wisdom, often not relating to academia, but always valued.

A big "Thanks!" to the past and present members of the lab: Vivega, Cheryl, Chris, Maryam, and Zahra. You made it fun. Throughout this project, Mark, Mike, Ron, and Joe were always patient and helpful instructors in the machine shop. I always looked forward to a day in the shop.

Tim Burkhart at Western University was instrumental in assisting with the pneumatic impactor and the data collection for many parts of this project. General Dynamics Land Systems- Canada allowed us to use their Anthropomorphic Test Device leg; a key piece of equipment for this thesis. Finally, I must acknowledge McMaster University and the Ontario Graduate Scholarship. These two source of funding made graduate school possible for me.

CONTENTS

1 Introduction 1
1.1 Statement of Problem 1
1.2 Injury Mechanisms to the Lower Limbs 3
1.2.1 Blast Injury 3
1.2.2 Vehicle Crashes 4
1.2.3 Mechanisms of Injury 5
1.3 ATD Testing and Injury Criteria 6
1.3.1 ATDs and other Surrogates 6
1.3.2 Injury Criteria 11
1.3.3 Out of Position Loading 16
1.4 Footwear in Testing 17
1.5 Integrating Force Sensors into Boots 20
1.5.1 Instrumented Sole 21
1.5.2 Instrumented Insole 24
1.5.3 Force Sensors for use in Instrumented Boots 25
1.6 Specific Aims 28
1.7 References 28
2 The Effect of Posture on Forces and Moments Measured in an ATD Lower Leg 33
2.1 Introduction 33
2.2 Methods 35
2.3 Results 40
2.4 Discussion 46
2.4.1 Effect on Injury Criteria 46

2.4.2 Moments Measured in the ATD 48
2.4.3 Limitations 54
2.5 Conclusions 55
2.6 References 56
3 Development of an Instrumented Boot 58
3.1 Introduction 58
3.2 Methods 60
3.2.1 Sensor Design and Construction 60
3.2.2 Instrumentation 65
3.2.3 Quasi-Static Calibration of the Sensor 67
3.2.4 Dynamic Testing of the Sensor 70
3.2.5 Boot Construction 71
3.2.6 Quasi-static Testing of the Assembled Boot 73
3.2.7 Dynamic Testing of the Assembled Insole and Leg 76
3.3 Results 79
3.3.1 Quasi-Static Calibration 79
3.3.2 Dynamic Testing of the Sensor 83
3.3.3 Quasi-static Testing of the Boot 85
3.3.4 Dynamic Testing of the Boot 89
3.4 Discussion 97
3.4.1 Sensor Quasi-Static Calibration 97
3.4.2 Dynamic Testing of the Sensor 99
3.4.3 Quasi-Static Testing of the Boot 101
3.4.4 Dynamic Testing of the Boot 103

3.4.5 Future Directions 105
3.5 References 106
4 Numerical Modelling of the Sensor Response 108
4.1 Introduction 108
4.2 Methods 110
4.3 Results 115
4.3.1 Normal Force 115
4.3.2 Shear Strain 119
4.4 Discussion 120
4.5 References 123
5 Discussion 125
5.1 Initial Ankle Posture in ATD Testing 125
5.2 Developing the Instrumented Boot 127
5.3 Summary 131
5.4 References 132
Appendix A- Anatomical Terms 133
Appendix B- MATLAB® Code for Analyzing ATD Posture Impacts without Boot 135
Appendix C- Hybrid III (Denton) Leg Schematic 140
Appendix D- Calibration Fixture, Lower Tibia Load Cell 141
Appendix E- Thor-Lx Lower Tibia Load Cell Diagram 142
Appendix F- LabView® Data Acquisition Block Diagram for Sensors 143
Appendix G- MATLAB® Code For Sensor Calibration Curves 144
Appendix H- MATLAB® Code to Average Multiple Sensor Calibration Curves 146
Appendix I- MATLAB® Code to Analyze Quasi-Static Boot Tests 147
Appendix J- MATLAB® Code to Analyze Dynamic Boot Tests 151

Appendix K- Calibration Curve Summary 156

Appendix L- MATLAB® Code for Force Visualization 157

Appendix M- MATLAB® Code for Piezoresistance Numerical Simulation 160

LIST OF TABLES

Table 1.1- The injury criteria used by the Insurance Institute for Highway Safety (2009). 15

Table 3.1- The order of testing for the plates under quasi-static load. 69

Table 3.2- Load thresholds used in the quasi-static tests. 75

Table 3.3- The postures tested under dynamic conditions. 78

Table 3.4- The slope of the load cell curve and percent work captured for each test. 85

Table 3.5- The average percent of the total load that each sensor recorded over the course of the quasi-static testing. 86

Table 3.6- Neutral Testing Before and After Impact Testing. 89

Table 3.7- The factor of difference between the peak force recorded by the boot and the peak F_{zLower} load cell channel. 93

Table 3.8- The average percent of the total load that each sensor recorded at the peak total boot force during neutral posture impact testing. 94

Table 5.1- A summary of the reduction of peak F_{zLower} forces caused by the boot. 131

LIST OF FIGURES

Figure 1-1- The major bones, tendons, and ligaments of the ankle (adapted from Inaba 1995). 5

Figure 1-2- The Hybrid III (A), Thor-Lx (B), and MiL-Lx (C) ATD leg models 9

Figure 1-3- The parts of the Hybrid III leg. 11

Figure 1-4- The coordinate system for the ATD. Axes indicate direction of force on foot which produces positive output in the upper and lower load cells. Compressive F_z forces are reported as a magnitude throughout this work. 12

Figure 1-5- The geometry of the Hybrid III ATD leg and the moment arms (in mm) created about the load cells when impacted parallel to the long axis, shown in red. 13

Figure 1-6- The *Quantum II* size 11 safety boot manufactured by Kodiak 19

Figure 1-7- A shoe instrumented with several single-axis load cells (Kljajić & Krajnik 1987). 21

Figure 1-8- A design with two, six-axis load cells attached to the sole and hinged in the middle of the foot (Chao & Yin 1999). 22

Figure 1-9- A shoe with two, six-axis load cells attached to the sole (Liedtke et al. 2007). 23

Figure 1-10- A spiked track shoe with a load cell built into one spike (Si et al. 2011).....24

Figure 2-1- A) The pneumatic impactor with the ATD leg mounted in a neutral posture. B) The ankle positioner in a neutral posture. 36

Figure 2-2- A plot of a complete impact event recorded by the F_{zLower} channel. 40

Figure 2-3- The effect of ankle flexion on upper peak A) F_z and B) TI_{Adj}. a= sig diff from -5°, b=sig diff from 20°, c=sig diff from 0°, d=sig diff from 10° ($p<0.05$). 42

Figure 2-4– The effect of ankle inversion and eversion on upper peak A) F_z and B) TI_{Adj}. a= sig diff from -20°, b=sig diff from -15°, c=sig diff from -10°, ...43

Figure 2-5- The effect of tibia angle on upper peak A) F_z and B) $TI_{Adj.}$ a= sig diff from 0°, b=sig diff from -5° ($p<0.05$). 44

Figure 2-6- Calculated impact durations over a range of inversion/eversion postures. 45

Figure 2-7- The calculated M_{xLower} moment arm over inversion/eversion postures. 49

Figure 2-8- The calculated M_{xLower} moment arm over plantar/dorsiflexion. 49

Figure 2-9- A simplified drawing (dimensions in mm) of the current arrangement used to attach the load cell (blue) to the ankle joint (red). 51

Figure 2-10- A) The ankle retention bolt showed signs of wear on the medial side at *X*. B) Paint removal at *Y* indicates that contact forces were not evenly distributed over the mating surfaces of the ankle joint. 52

Figure 3-1- The steel plates used in the construction of the sensors, before being blasted with glass beads (left) and after being blasted (right). 62

Figure 3-2- The three sensor geometries (dimensions in mm). 62

Figure 3-3- A representative diagram of pressure distribution during normal walking (Hudson 2014) with an overlay of the sensor layout. 63

Figure 3-4- The completed sensor. 64

Figure 3-5- Eight voltage dividers in parallel were used (three voltage dividers are shown). R1, R3, and R5 are reference resistors, while R2, R4, and R6 represent the sensors, which vary in resistance with applied pressure. 65

Figure 3-6- The voltage divider circuit board. 66

Figure 3-7- Quasi-static calibration of the sensor on the material testing machine. 68

Figure 3-8- The sensors and their relative positions as they were 72

Figure 3-9- The boot and leg installed in the material testing machine. 74

Figure 3-10- The boot and ATD leg in a neutral posture in the pneumatic impactor. 76

Figure 3-11- Representative calibration curve of A) test 1 for plate 1, a large plate and B) test 2 for plate 2, a small plate. The red line is the experimental data, and the black line is the fit. 80

Figure 3-12- The three calibration curves from the tests on plate 1 were averaged and fit with a curve. 81

Figure 3-13- Average calibration curves for testing before and after impacts, and with eccentric loads. 82

Figure 3-14- Two drop tests comparing the force recorded in the sensor and the load cell. The impact was modulated with A) corrugated cardboard and B) rubber. In A the factor of difference was 5, while in B the factor of difference was 3.75. 84

Figure 3-15- The force recorded by the material tester load cell and the total force recorded by the boot sensors during A) Test 8 and B) Test 5. 88

Figure 3-16- The distribution of forces over the sole of the foot during the impact. 91

Figure 3-17- The force curve from the F_{zLower} channel of the ATD and the total measured boot force for a neutral impact. 92

Figure 3-18- The percent of peak force that sensor four carried across tested postures in plantar/dorsiflexion. 95

Figure 3-19- The peak F_{zLower} and boot force in dorsi/plantarflexion. Symbols denote significant differences ($p<0.05$). 96

Figure 3-20- The peak F_{zLower} and boot force in inversion/eversion. Symbols denote significant differences ($p<0.05$). 96

Figure 3-21- Permanent deformation (A) on the underside of the insole after testing. ...102

Figure 4-1- Simulated current through a volume of conductive, uniform, spherical particles (a volume approximately 1/5 of that which was used in the simulation is shown in this figure for clarity). 116

Figure 4-2- The relationship between change in resistance and applied force. Experimental and scaled numerical simulation results are plotted. 117

Figure 4-3- The average ratio of resistance to initial resistance as more simulations (number shown in legend) were added. Convergence occurred at approximately 100 simulations. These results are scaled by the same factor as above. 118

Figure 4-4- A semi-log plot showing the average ratio of resistance to initial resistance as more simulations (number shown in legend) were added. Convergence occurred at approximately 1500 simulations. 119

Figure 4-5- The ratio of resistance to initial resistance was near unity 120

Figure 5-1- The peak force measured in F_{zLower} with and without the boot, and ten times the peak forces measured by the boot, at various postures. 130

LIST OF ABBREVIATIONS AND SYMBOLS

a- Cross sectional area of a conductive particle

ATD- Anthropomorphic Test Device

DAQ- Data Acquisition Device

e- Electron charge

F_c- Critical axial force value used in the Tibia Index

F_x- Force meausred along the x-axis of the ATD leg

F_y- Force meausred along the y-axis of the ATD leg

F_z- Axial compression force measured in the ATD leg

h- Planck's Constant

HSD- Honest Significant Difference

I- Electrical Current

J- Electrical Current Density

M_c- Critical moment value used in the Tibia Index

m- Electron mass

M_x- Moment about the x-axis in the lower ATD load cell

M_y- Moment about the y-axis in the lower ATD load cell

PSR- Pressure Sensing Resistor

R- Resistor

s- surface to surface distance between conductive particles

SD- Standard Deviation

TI- Peak Tibia Index

TI_{Adj}- Peak Adjusted Tibia Index

V- Voltage

X_{Lower}- Used to denote the ankle load cell on the ATD

X_{Upper}- Used to denote the knee load cell on the ATD

φ- *En*ergy barrier to electron transfer

DECLARATION OF ACADEMIC ACHIEVEMENT

I participated in or completed independently all data collection.

I performed all the data analysis described in this work.

I created protocols for data collection.

I created all of the programs used in this document, drawing from built in functions and shared code.

I designed and manufactured jigs and testing fixtures, as well as modifying some existing fixtures.

1 Introduction

1.1 Statement of Problem

High force, short duration impacts can cause severe injuries to the legs and feet. These injuries are commonly seen in soldiers who are riding in vehicles which are subject to an explosive blast on the modern battlefield, and are associated with high morbidity (Ramasamy et al. 2013). Similarly, debilitating injuries to the lower leg can occur in occupants of motor vehicles involved in serious accidents (Richter et al. 2001). The accurate determination of the forces and moments developed in the lower leg and foot by these impacts is an important step towards understanding the mechanisms of injury and in the design of better safety systems.

The use of Anthropomorphic Test Devices (ATDs) to simulate humans in safety tests is well established (Mertz 1994; Welbourne and Shewchenko 1998). Forces and moments measured in ATDs during testing are compared to established injury criteria. This allows for prediction of the injuries a human in the same crash would suffer. These criteria have been developed mainly by subjecting cadaveric specimens to controlled impacts and cataloging the types of injuries the specimens sustained (*e.g.*, Funk et al. 2002). Lower limb injury criteria used with ATDs have been developed based on neutral postures of the leg and ankle, but the effect of initial ankle posture on measured forces and moments in the leg has been shown to significantly affect ATD behavior in blast loading and in

vehicle accidents using computer simulations (van der Horst et al. 2005), real world injury review (Lestina et al. 1992), and cadaveric impacts (Crandall et al. 1998). In real world accidents the posture of the leg is not controlled, and can assume any position within the normal range of motion.

The effect of initial posture on the forces and moments measured in the legs of ATDs during impact events has not previously been investigated. This may influence the outcome of injury assessment, which could influence safety ratings.

In a normal situation, a person subject to a blast or automobile accident will be wearing some form of footwear. However, in ATD testing and the development of injury criteria, footwear use is not consistent (Gallenberger 2013). This is true even though a heavy, thick work boot will transmit forces differently than a light, thin dress shoe.

The lack of measured force magnitude and location on the sole of the foot prevents these differences from being well described, and also prevents the development of injury criteria which are specific to the feet.

1.2 Injury Mechanisms to the Lower Limbs

1.2.1 Blast Injury

Explosive blasts generate shockwaves that can interact with rigid bodies (*e.g.,* vehicle hulls) and produce high magnitude, short duration accelerations (Dong et al. 2013). When humans are in contact with these rigid bodies, the accelerations can create very high, injurious forces in tissues. Injuries of this type were first been noted by Keating in 1944. He found that during World War Two, mariners who were leaning or standing on the hull of naval vessels in close proximity to exploding mines developed a "deck slap" injury (Elston et al. 2013).

This mechanism of injury is often associated with injury to the lower extremities because these body parts are most often in direct contact with surfaces exposed to explosive blast. In modern warfare, the injury is most commonly seen in mounted soldiers who are subject to an under-vehicle explosive blast (Dougherty et al., 2009; Ramasamy et al., 2011; Ramasamy et al. 2013). The extremity injury caused by an explosion is the most common modern injury in warfare, with the lower extremity injury accounting for about half of these injuries (Belmont, Schoenfeld, and Goodman 2010; Owens et al. 2007).

Injuries caused by explosive blast have been grouped into four categories (Ramasamy et al. 2011):

1- Direct injury caused by the shockwave

2- Injury due to ejecta and other missiles

3- Injury that occurs due to acceleration of the body

4- Burns, inhalation of hot gases

Lower extremity injuries being examined in this work are primarily due to the 3rd mechanism; these occur when the hull of a vehicle deforms, and energy is transferred into the legs and feet of a soldier in the vehicle.

1.2.2 Vehicle Crashes

Although the motivation for this research stems from combat injuries, severe lower leg injuries can also occur in vehicle crashes. Accelerations during vehicle crashes are generally lower, and impact durations longer than in blast events, but injuries to the lower extremities are still a major concern (Bir et al. 2006; van der Horst et al. 2005). The tools and techniques developed in studying blast impacts can be applied to the study of car crashes.

Injuries to the foot are most common in frontal impacts, and occur in car drivers in about 1.3% of car crashes (Otte et al. 1992). Ankle/hindfoot injuries have been identified as the

most significant group of injuries to the lower limb because these are associated with the most significant long term impairment (Morris et al. 1997).

1.2.3 Mechanisms of Injury

The foot is a remarkably complex structure. There are 26 bones in each foot, along with cartilage, tendons, and ligaments. Figure 1-1 shows some of the major structures in the ankle. Throughout this thesis, anatomical terms are used to define the positions and orientations of various parts of the ATD, or to reference human anatomy. Appendix A gives an overview of these terms.

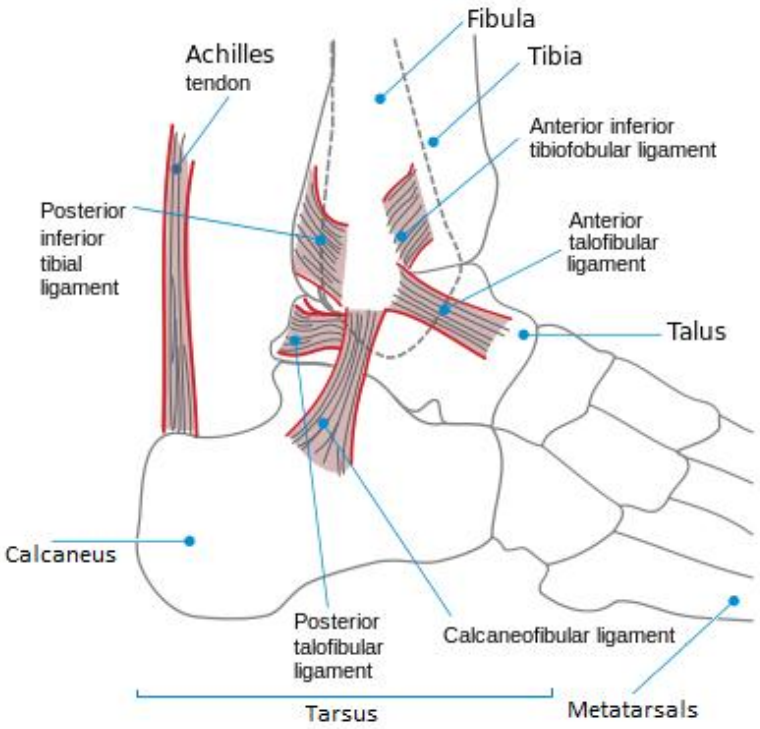

Figure 1-1- The major bones, tendons, and ligaments of the ankle (adapted from Inaba 1995).

In accidents, there are innumerable ways in which the foot can be damaged (Lestina et al. 1992). In the hindfoot, the calcaneus is often fractured when force is concentrated on the heel of the foot (Crandall et al. 1998). The talus bone and malleoli, which are prominences on both sides of the ankle, can also fracture. During axial loading, pilon fractures, where the talus is driven into the distal tibia causing a comminuted fracture, can occur. This is an especially damaging fracture, which is often associated with high forces (Wiler 2008). A Lisfranc fracture occurs when the metatarsal bones are displaced from the tarsus. The mechanism for this injury is often attributed to high contact forces between the midfoot and the pedals in a vehicle (Morris et al. 1997).

In the forefoot, injuries to the metatarsals and phalanges (toe bones) can occur (Otte et al. 1992). Generally, forefoot injuries have been found to be associated with lower morbidity than hindfoot injuries.

1.3 ATD Testing and Injury Criteria

1.3.1 ATDs and other Surrogates

Cadaveric specimens provide the most realistic representation of a living human for use in the development of injury criteria. This is because human tissue is difficult to represent using engineered materials; it is anisotropic, viscoelastic, and non-homogenous (Iyo et al. 2004).

However, this type of testing requires special ethical consideration, is expensive, and due to the difficulties of acquiring appropriate cadaveric specimens, only a limited number of trials can be completed. Cadaveric specimens tend to be taken from an older demographic, which is not necessarily representative of the individuals who are at risk from injury due to impact loading. Also, varying age and gender creates variability in the mechanical properties and resulting mechanical behavior of cadavers. The viscoelastic nature of tissue makes it difficult to determine the mechanical properties; quasi-static and dynamic loading may produce different outcomes (Schreiber et al. 1998). Even preserving a cadaveric specimen can affect the biofidelity of the specimen. The biomechanical properties of tendons, for example, are not maintained after embalming (Fessel et al. 2011), although for bone deep freezing or embalming appears not to affect bulk mechanical properties (Topp et al. 2012). For these reasons, there are several engineered surrogates available for assessing potential injury in a controlled impact test.

The Frangible Surrogate Leg (Adelaide T&E Systems, Torrensville, South Australia, Australia) was developed to physically mimic the lower leg during blast explosions; it looks like a leg, but has synthetic components to mimic the bones, cartilage, connective tissue and soft tissue in the leg (NATO 2007). Like cadaveric specimens, the leg can only be used for one destructive test because it will fracture. The benefit of the frangible leg is that it provides a more repeatable standard and could be manufactured for less than the cost of a cadaveric leg. The drawback is that the materials selected did not mimic some

tissue properties. To the author's knowledge this surrogate is no longer used due to its unrealistic fracture mechanisms.

Anthropomorphic Test Device (ATD) testing is the least expensive, most widely practiced method to predict injury in a controlled event. Commonly known as a 'crash test dummy', the device plays a critical role in the assessment of occupant safety in vehicle tests. The ability to accurately assess the risk of lower leg injury using ATDs is highly desirable to facilitate improvements of safety systems in automotive and military vehicle design.

The ATD is an instrumented representation of a human. It is available in different sizes to represent different demographics; ATDs that are sized to represent the anthropometry of women, men, and children in different body size groups are available. The most commonly used ATD lower leg is the Hybrid III Leg, also known as the Denton Leg, which is the standard leg on the Hybrid III ATD (Humanetics Innovative Solutions, Plymouth, MI, USA). The 50^{th} percentile male version of this ATD has a leg and foot with a combined mass of 5.68±0.09 kg (Mertz 1994).

ATDs have been shown to transmit load differently than cadaveric specimens, especially during high impulse, short duration loading (Quenneville & Dunning 2012). Much of this discrepancy is attributed to the difference in stiffness between human tissue and the material of which the ATD is constructed (rubber, aluminum, and steel). To reduce this discrepancy, several ATD legs have been developed that are specifically designed for use in safety testing of the lower leg (Quenneville & Dunning 2012). Both the Thor-Lx and

the MiL-Lx (Figure 1-2) (Humanetics Innovative Solutions, Plymouth, MI, USA) are considered to be more biofidelic, which may make them more suitable for injury assessment in the lower leg (Kuppa et al. 1998; Quenneville & Dunning 2012).

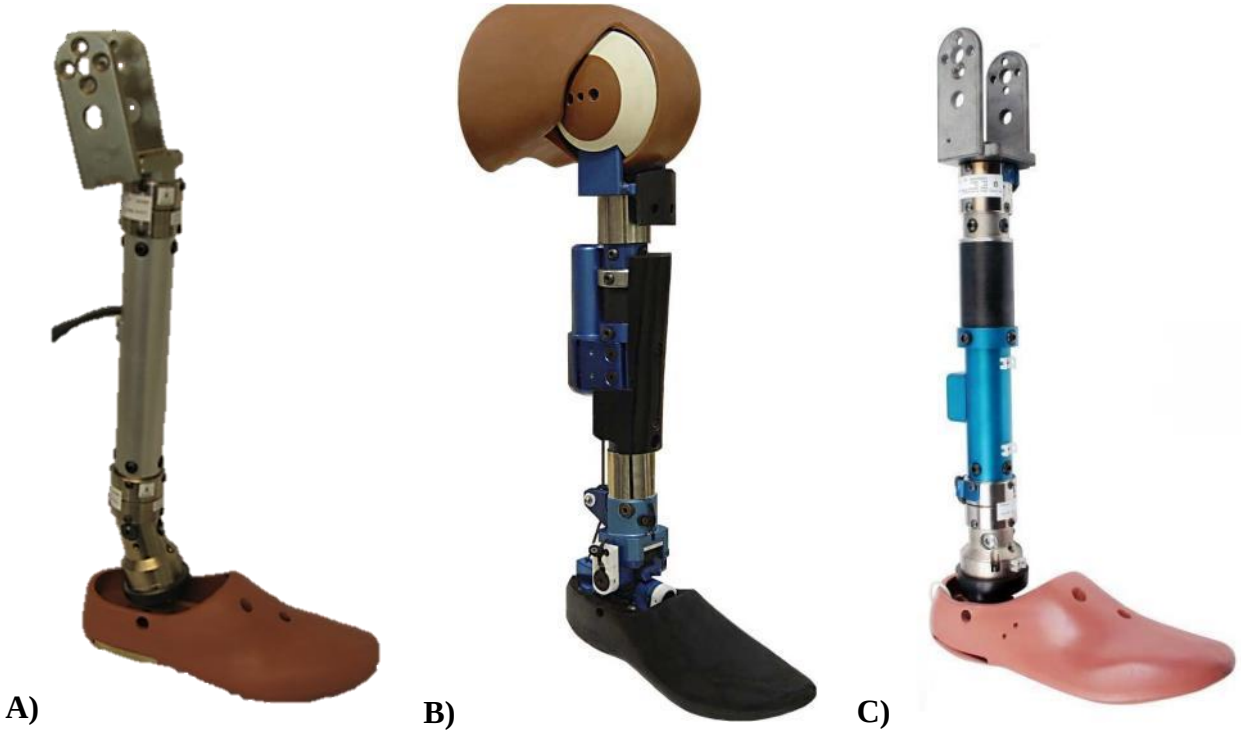

Figure 1-2- The Hybrid III (A), Thor-Lx (B), and MiL-Lx (C) ATD leg models (Humanetics Innovative Solutions 2014).

The Thor-Lx better matches the stiffness of a cadaveric leg by incorporating a compliant element, simulates loading by the Achilles tendon, and better mimics the location of articulations in the human ankle joint. The Thor-Lx also incorporates instrumentation to track the position of the ankle throughout the impact. The MiL-Lx is especially suited for blast impact loading, incorporating a longer compliant element and eliminating the tendon because muscle loading is thought to be not as influential in injury prediction during blast

loading as in crash testing (McKay 2010). However, considering the amount of work that has been invested in developing injury criteria using the Hybrid III and the widespread industry use of this tool, it is likely that the Hybrid III will still be used extensively for crash testing in the foreseeable future.

The Hybrid III leg is remarkably simple in design (Figure 1-3). The ankle is represented by a ball joint, which has a rubber collar to limit the range of motion of the foot to the natural range of motion in humans and to create some cushion on the limits of the joint motion. The stiffness of the joint can be adjusted with a screw, which creates friction forces on the ball joint. There are several load cells that can be mounted on the Hybrid III leg. The standard configuration is a five-axis load cell mounted just above the ankle joint (the distal, or lower load cell) and another five axis load cell just below the knee clevis (the proximal, or upper load cell).

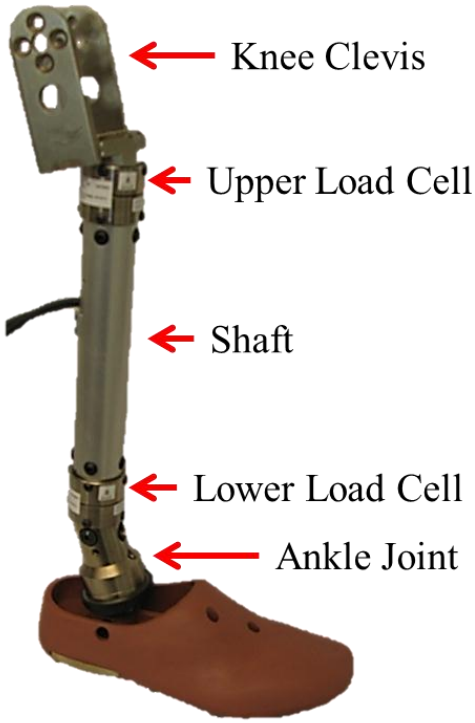

Figure 1-3- The parts of the Hybrid III leg.

1.3.2 Injury Criteria

In automotive testing, the two main injury criteria used in tests with ATDs are the Peak Axial Force (F_z) and the Tibia Index (TI) (Mertz, 1994; Insurance Institute for Highway Safety, 2009). In military testing, the Peak Axial Force is most often used (NATO/PfP 2006). Other instrumentation for the leg, such as a force sensor in the toe of the foot and accelerometers in the leg, is available, but criteria developed with these inputs are not widely used. The Tibia Index (Eq. 1.1) addresses the contribution of a bending moment as well as an axial force in the fracture risk of the tibia.

Tibia Index:

$$TI = \frac{\sqrt{{M_x}^2 + {M_y}^2}}{M_C} + \frac{F_z}{F_{z_C}} \qquad \text{Eq. 1.1}$$

$$Where: M_C = 225\ Nm, F_{z_C} = 35.9\ kN$$

In this equation, M_x and M_y are moments about the x and y axes, respectively. F_z is the measured axial force. M_c and F_{zC} are critical values that are used to weigh the measured values; there has been some debate over the appropriate critical values to use, so in the absence of consensus the original values (noted above) will be used throughout this work (Funk et al. 2004).

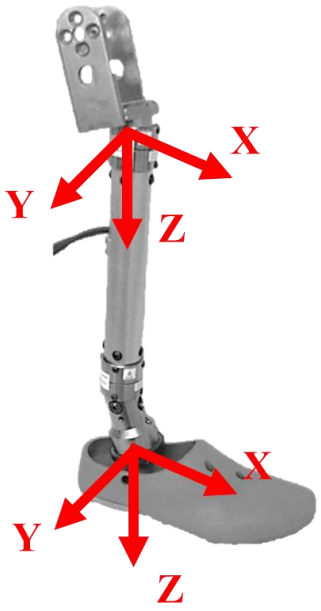

Figure 1-4- The coordinate system for the ATD. Axes indicate direction of force on foot which produces positive output in the upper and lower load cells. Compressive F_z forces are reported as a magnitude throughout this work.

The coordinate system for the Hybrid III leg is shown in Figure 1-4. The leg has two angled components (the knee clevis and ankle mount); this causes the long shaft of the leg to sit at an angle in relation to the neutral axis of the leg, which runs from the knee clevis to ankle joint. This is in contrast with the human tibia, which connects the knee and ankle in a relatively straight line. This angle creates an offset, which induce moments in the load cells under a load that would be purely axial in the human leg. Figure 1-5 shows the moment arms created by this unusual geometry.

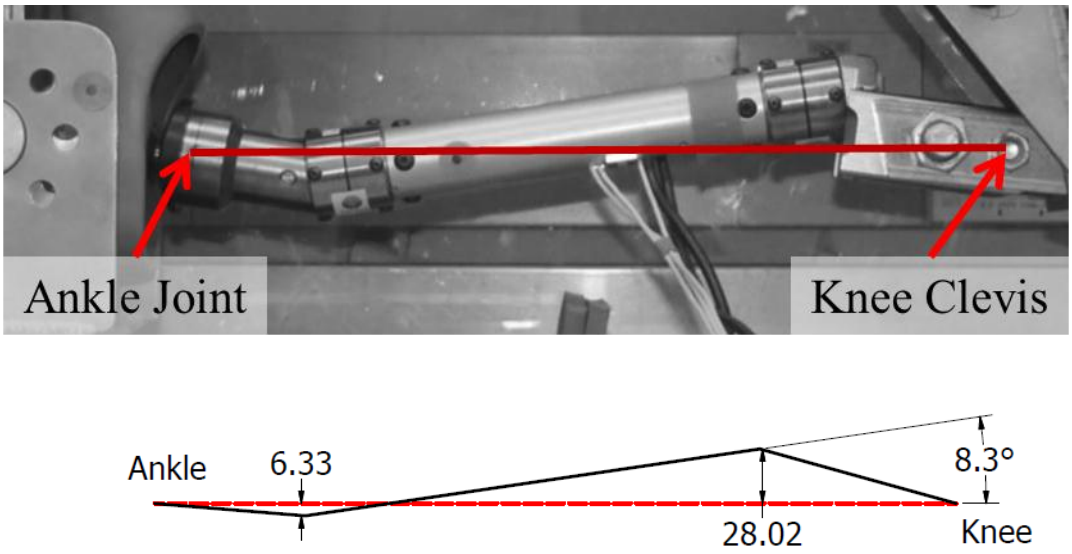

Figure 1-5- The geometry of the Hybrid III ATD leg and the moment arms (in mm) created about the load cells when impacted parallel to the long axis, shown in red.

To account for the bending moments that have been noted in the load cells under axial loading, an Adjusted Tibia Index (TI_{Adj}) has been developed (Eq. 1.2 and Eq. 1.3) (Zuby, Nolan, and Sherwood 2001; Welbourne and Shewchenko 1998). The TI_{Adj} also incorporates a factor to account for the fact that only a component of the axial force is measured, due to the angle that the load cell makes with respect to the long axis of the Hybrid III leg. The Adjusted Tibia Index has been widely adopted in crash testing.

Adjusted Tibia Index (Upper):

$$\mathrm{TI_{Adj}} = \frac{\sqrt{{M_x}^2 + \left(M_{y_{upper}} - 0.02832F_z\right)^2}}{M_C} + \frac{F_z}{F_{z_C}} \qquad \text{Eq. 1.2}$$

Adjusted Tibia Index (Lower):

$$\mathrm{TI_{Adj}} = \frac{\sqrt{{M_x}^2 + \left(M_{y_{lower}} + 0.006398F_z\right)^2}}{M_C} + \frac{F_z}{F_{z_C}} \qquad \text{Eq. 1.3}$$

$$Where: M_C = 225\ Nm\ and\ F_{z_C} = 35.9\ kN$$

Although multiple different limits to these injury criteria have been proposed, a set of standard limits in car crash testing is shown in Table 1.1 (Insurance Institute for Highway Safety 2009). For military testing, NATO recommends an injury criterion of a maximum compressive force of 5.4 kN measured in the lower load cell (NATO/PfP 2006). Other

specific injury criteria for blast impacts are still being developed (Quenneville et al. 2011). The military field does not widely use either the TI or TI_{Adj}.

Table 1.1- The injury criteria used by the Insurance Institute for Highway Safety (2009).

Parameter	*Good-Acceptable*	*Acceptable-Marginal*	*Marginal-Poor*
Adjusted Tibia Index (TI_{Adj})	0.8	1	1.2
Tibia Axial Force (kN)	4	6	8

To develop these criteria, axial impacts of varying magnitudes were performed on both ATD legs and cadaveric legs, and injuries to the cadaveric legs were statistically correlated with measured forces in the ATD.

There has been a limited amount of work in developing criteria for joint injuries. A limit of 4 kN compression on the tibial plateau was established as the injury criterion for the knee, and this same value was then inferred to the ankle (Mertz 1994). Both of these values were set based on the work by Hirsch and Sullivan (1965). Hirsch's experiments were based on a small sample of individuals of mixed age and gender, and the rate of loading was much slower (16.35 N/s) than that seen in blast loading (1 MN/s, for a 5.4 kN impact with a 10 ms duration). This early contribution to the field is not commonly used,

but does show that the need for joint-specific injury criteria was identified early on in the history of safety testing using ATDs.

1.3.3 Out of Position Loading

The human foot and ankle are formed by multiple bones and articulations. Changing the posture of the ankle changes the load path through the foot, which could affect the location and severity of injuries to the human foot, ankle, or leg. There has been limited work on developing injury criteria for the leg when it is in a non-neutral position. In 2005, van der Horst et al. performed controlled impacts using a Hybrid III ATD, and modelled those impacts in a numerical simulation. All of the experimental work was conducted with a neutral seating posture, while numerical simulations were performed with the ATD in four different seating postures. Simulations with the leg in a neutral posture, as well as simulations with the leg slightly extended from normal seating posture with the feet flat on the floor (plantarflexion of the ankle) produced the highest axial forces in the leg. Impacts with the legs slightly extended from normal seating posture but with the ankle in a neutral posture produced lower axial forces. However, the authors of this study acknowledged that without postmortem studies, it is not possible to estimate if the modeled forces correlated with injury risk because the mechanisms of injury may vary.

Crandall et al. (1998) performed out-of-posture impacts on 50 cadaveric lower limbs and recorded the injuries produced in each post-impact. They attempted to achieve a

biofidelic response by leaving the leg mainly intact (the exception being the installation of a load cell in the tibia diaphysis and a mounting plate on the calcaneus), and mounting the specimen at the femur with a fixture that mimicked the stiffness and range of motion of the hip. A pendulum-type impactor was used to strike the leg, with the drop height and mass varied to achieve different impact parameters. The ankle was positioned over a range of initial postures in dorsi/plantarflexion and in/eversion. They found that initial dorsiflexion of the ankle was associated with a decreased risk of injury. They suggested this was because the ankle joint has a higher contact area in this posture, and is therefore exposed to lower stresses in comparison to a neutral or plantar-flexed foot. It was found that initial in/eversion angle, forces measured in the tibia, and Tibia Index were poor predictors of injury. Foot contact force, the rate of force onset, and the acceleration measured in the heel were found to be the best predictors of injury. It was also found that injury occurred early in the impact, when forces were at their highest but the position of the ankle was still within its normal range of motion. It should be noted that in this study, the number of specimens in each test group was small, and that they produced only 11 injuries in the 50 impacts. This may indicate that the testing energies were too low.

1.4 Footwear in Testing

Footwear has the capacity to extend the rise time to peak loading and also to absorb some energy during an impact (Newell et al. 2012). The stiffness of the boot and the viscoelastic nature of the materials in it both affect the ability of footwear to attenuate

blast loading. Despite the ability of footwear to substantially affect the measures in the lower leg during impact loading, there is no standard for footwear to be used during ATD testing. For blast testing, the NATO document "Procedures for Evaluating the Protection Level of Logistics and Light Armored Vehicles" recommends that *"Footwear should be the same as that required under normal conditions by the crew or passengers of the vehicle under test, and should be in good condition"* (NATO/PfP 2006). In vehicle testing, the occupant is not dressed in standard footwear, only that which is 'typical', which can cover a range of footwear. This inconsistency represents a confounding factor which could be addressed by creating more descriptive standards for footwear use in safety testing.

One of the goals of the current work is to develop an instrumented boot to further the understanding of force distribution and magnitude on the feet during impact testing. Understanding the normal construction of protective footwear is necessary to determine the most appropriate location to place instrumentation without substantially changing a boot's form or function. A typical work boot was the subject of the work presented here (Figure 1-6).

Figure 1-6- The *Quantum II* size 11 safety boot manufactured by Kodiak used in this work.

The sole of the boot is the element that directly contacts the ground; it is commonly made of synthetic rubber. The insole sits inside the boot and directly under the foot, cushioning and supporting it. The shank is a stiff element, often made of steel or fiber-reinforced polymer, which sits on top of the sole to control the rigidity of the boot. The toe cap is steel or fiber-reinforced polymer, and protects the toes from crushing injuries. Safety boots often include a puncture-resistant steel or fiber-reinforced polymer plate under the insole to protect from puncture by nails or other sharp objects underfoot; this often doubles as the shank of the boot.

Footwear has been identified as a major factor which affects the peak forces measured in the leg. McKay and Bir (2010) suggested that a boot can reduce Peak Axial Force by 8-28%, depending on the impact conditions. Quenneville and Dunning (2012)

demonstrated the ability of a standard hiking boot to reduce Peak Axial Force due to blast impact in the leg by up to 65%. A study of two different combat boots that are standard issue to troops in the United Kingdom showed that the rate and magnitude of loading can affect a boot's ability to attenuate blasts (Newell et al. 2012). Developing boots specifically for blast attenuation and issuing these boots to soldier may help to prevent these injuries in the future.

1.5 Integrating Force Sensors into Boots

Footwear can be easily mounted on both ATD legs and cadaveric specimens, and is representative of real world situations because a vehicle occupant is usually dressed in some form of footwear. Force measurement in the feet of ATDs and cadaveric specimens is not currently practiced. However, integrating a force sensor in a boot would allow for an understanding of the location and magnitude of impact as it is applied to the foot. This would be beneficial for creating comprehensive injury criteria that address injury to the foot as well as the leg. It would also advance the understanding of the mechanism of injuries sustained in these events, and provide the ability to instrument both cadaveric specimens and ATDs in the same manner.

Force sensors have been integrated into footwear for a variety of reasons. Gait studies, sport science, custom orthotics, and even disease diagnosis have all motivated the search for a reliable way to record force magnitude and distribution underfoot. There are two broad strategies employed to implement these sensors: the first is to place sensors

between the ground and the sole of the footwear and the second is to place sensors between the foot and the sole of the shoe, either above or below the insole.

1.5.1 Instrumented Sole

An instrumented sole was made by Kljajić and Krajnik (1987) (Figure 1-7). They incorporated multiple single-axis load cells into the sole of a shoe to allow for evaluation of gait. The design allowed for identification of the centre of force during walking, as well as the total force, but would have created force concentrations at specific points over the foot. This likely affected the gait during walking, as the contact was at points rather than being distributed over an area. The load cells may also have given erroneous readings when subjected to shear forces, which are more common on the exterior of the shoes, thus limiting the applicability of this device.

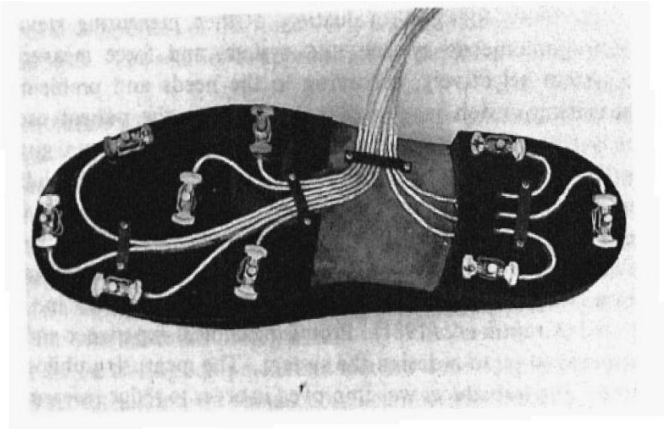

Figure 1-7- A shoe instrumented with several single-axis load cells (Kljajić & Krajnik 1987).

The use of six-axis load cells to instrument shoes has been attempted more recently. The first group to try this linked the load cells together with a hinge (Figure 1-8); this constrained the movement of the cells and consequently the foot (Chao & Yin 1999). This design would significantly change the gait of the foot and, more importantly for the present purposes, the transmission of forces to the foot.

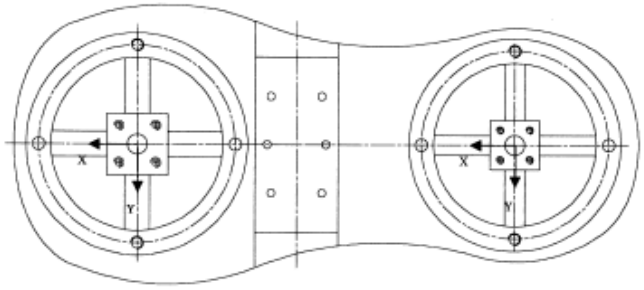

Figure 1-8- A design with two, six-axis load cells attached to the sole and hinged in the middle of the foot (Chao & Yin 1999).

A more recent attempt to incorporate load cells into the sole of a shoe allowed free movement of two load cells relative to the other (Figure 1-9) (Liedtke et al. 2007). Each load cell was mounted on an aluminum plate; one load cell was attached to the sole under the ball of the foot, and the other under the heel. This system did allow for a more natural gait, but the bulky load cells likely changed the gait and load distribution on the foot. Also, due to the increased heel height caused by the load cells, which were 15.7 mm thick (excluding plates and mounting hardware), larger moments in the leg due to shear forces on the sole of the shoe would be expected (ATI Industrial Automation 2014).

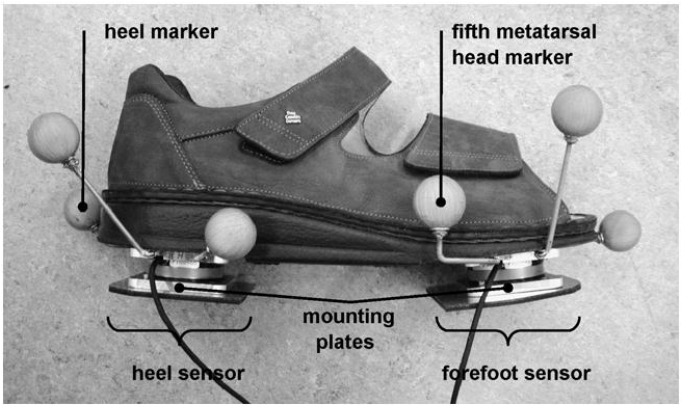

Figure 1-9- A shoe with two, six-axis load cells attached to the sole (Liedtke et al. 2007).

Si, Yan, and Liu (2011) developed a spiked track and field shoe that used piezoelectric sensors to measure forces on one spike (Figure 1-10). Unfortunately, only preliminary tests were carried out using this shoe, and therefore it is not clear if the design performed as intended. The shoe would likely not be able to fully quantify forces, as alternate loading paths with un-instrumented areas would be established as soon as the spike settled into the ground.

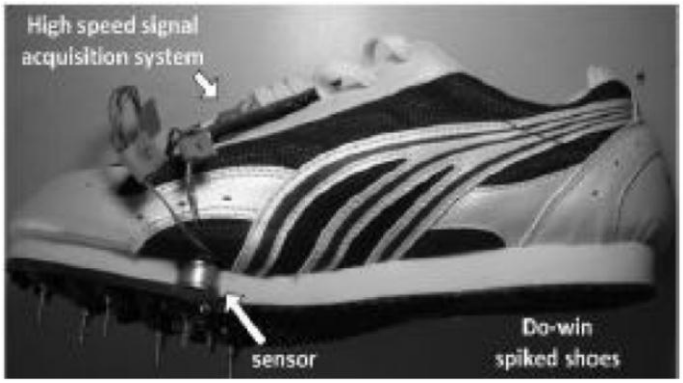

Figure 1-10- A spiked track shoe with a load cell built into one spike (Si et al. 2011).

Upon review, none of these concepts were considered to be adequate for recording forces due to blast impacts. These concepts were designed to record forces that would be expected during normal ambulation or during sport, not during injurious events. The magnitude of the force in impacts would be high enough to necessitate much larger load cells, which would have substantial effects on the dynamics of the foot and leg. Also, using only one or two load cells would make it difficult to quantify the distribution of forces on the foot and identify risk of injury to a specific region of the foot (*e.g.*, forefoot or hindfoot).

1.5.2 Instrumented Insole

Instrumented insoles have been developed to measure pressure on the sole of the foot while walking. These commonly incorporate Pressure Sensitive Resistors (PSRs) into the insole of the shoe (Razak et al. 2012; Wertsch et al. 1992). Some also incorporate

gyroscopes or accelerometers in an attempt to quantify the kinematics of the foot (Kirtley 2001). These insoles are light and low profile, and have been used successfully to assess gait and to determine a general pressure distribution on the foot.

Pressure sensitive resistors can measure forces at particular locations, but in most applications they are not the exclusive load path between the sole and the foot; a few PSRs distributed over an area only gives a general indication of the pressure distribution. This means that it is very difficult to determine the absolute force between the foot and the sole, which makes these insoles unappealing for determining force magnitude for injury prediction.

A piezoelectric insole was previously developed that can fully quantify the forces acting across the sole of the foot (Hennig et al. 1982). However, for reasons that are not readily apparent, the work on this design was discontinued. It is possible that the fragility of piezoelectric elements and the complex instrumentation required for this design made it impractical.

1.5.3 Force Sensors for use in Instrumented Boots

There are many types of commercially-available force sensors. Strain gauge based load cells are constructed by mounting a strain gauge on a precisely designed and constructed elastic member. When the load cell is loaded, the elastic member deflects, and the strains measured can be used to calculate the applied load. Although these load cells can be extremely accurate, they are difficult to implement in footwear, as demonstrated by some

of the designs mentioned in Section 1.6.1, as they tend to be bulky and are relatively fragile. If the elastic member is plastically deformed by excessive force, the load cell is destroyed, which necessitates them being designed to ensure they are in a state of stress below the yield stress of the material of which they are constructed.

Capacitive force sensors are another promising tool; however, they require specialized instrumentation and are relatively fragile (Dobrzynska & Gijs 2013). These sensors use change of capacitance to measure load, most frequently caused by changing the distance between plates in a parallel plate capacitor. Measuring the capacitance requires a precisely generated current and more complicated data collection and analysis, making it challenging to implement them for the current purpose.

Pressure sensitive paper, often known by the trademark Prescale™, is a product that changes color when subjected to pressure. The intensity of the color change can be used to determine the applied pressure. The product comes as two sheets, a developing sheet and a sensing sheet (Sensor Products Inc 2011). The sheets are placed together and pressure is applied. On the sensing sheet microbubbles of ink burst at specific pressures, which then react with the developing paper to create the color change. The sheet can either be interpreted visually for a general sense of the pressure distribution, or it can be digitized and computer software can be used to provide more quantitative measures of the total force applied. This sensor can be used to measure impacts of very short duration, and it is as thin as two sheets of paper, lightweight, and gives a full pressure distribution (Ogawa & Yokoyama 2000). Unfortunately, the pressure sensitive paper does not

provide a means to resolve time differences between impact events; the paper only indicates the peak pressure applied in each area over the entire duration of a test. This makes it a potentially interesting option for single controlled impacts, but less appealing for use in real world crash testing, where multiple impacts of different magnitudes may occur over the duration of the test. Because pressure sensitive paper is only good for one use, it is also costly.

Pressure sensing resistors (PSRs) are a straightforward choice for integration into a boot because they are robust and easily instrumented. There are multiple types of PSRs. A simple type uses a domed, elastic pad that contacts a flat, stiff plate. As the force increases the pad deforms, increasing the contact area and thus decreasing the resistance across the sensor. This type is simple to implement, but has a relatively limited force range because the pad will eventually deform to the point where it completely covers the contact area or fails.

The second type of PSR uses a piezoresistive material. This material changes resistance with applied pressure due to strain, and is often a polymer. The piezoresistive polymer is generally inexpensive, thin, reusable, and robust. Instrumentation is simple and is easily compatible with Data Acquisition Systems (DAQs) used in crash testing.

1.6 Specific Aims

The specific aims of this thesis are to:

- Assess the effect of initial ATD posture on the ability to accurately quantify injury to the lower leg using established techniques.
- Develop an instrumented boot capable of recording the magnitude and distribution of forces applied to the sole of the foot.
- Validate the ability of the instrument boot to record impacts by mounting it on an ATD and impacting it in a controlled manner at multiple ankle postures.
- Develop a numerical model to investigate shear loading on the active material in the piezoresistive force sensor used in the aforementioned boot.

1.7 References

ATI Industrial Automation. (2014). F/T Sensor- Mini45. Retrieved June 02, 2014, from http://www.ati-ia.com/products/ft/ft_models.aspx?id=Mini45

Belmont, P. J., Schoenfeld, A. J., & Goodman, G. (2010). Epidemiology of combat wounds in Operation Iraqi Freedom and Operation Enduring Freedom: orthopaedic burden of disease. Journal of Surgical Orthopaedic Advances, 19(1), 2–7.

Bir, C., Barbir, A., Dosquet, F., Wilhelm, M., van der Horst, M., & Wolfe, G. (2006). Validation of lower limb surrogates as injury assessment tools in floor impacts due to anti-vehicular land mines. In IRCOBI Conference (Vol. 173, pp. 279–288). Madrid, Spain.

Chao, L.-P., & Yin, C.-Y. (1999). The six-component force sensor for measuring the loading of the feet in locomotion. Materials & Design, 20, 237–244.

Crandall, J. R., Kuppa, S. M., Klopp, G. S., Hall, G. W., Pilkey, W. D., & Hurwitz, S. R. (1998). Injury mechanisms and criteria for the human foot and ankle under axial impacts to the foot. International Journal of Crashworthiness, 3(2), 147–62.

Dobrzynska, J. a, & Gijs, M. a M. (2013). Polymer-based flexible capacitive sensor for three-axial force measurements. Journal of Micromechanics and Microengineering, 23, 1–11.

Dong, L., Zhu, F., Jin, X., Suresh, M., Jiang, B., Sevagan, G., Cai, Y., Li, G., & Yang, K. H. (2013). Blast effect on the lower extremities and its mitigation: a computational study. Journal of the Mechanical Behavior of Biomedical Materials, 28, 111–24.

Dougherty, A. L., Mohrle, C. R., Galarneau, M. R., Woodruff, S. I., Dye, J. L., & Quinn, K. H. (2009). Battlefield extremity injuries in Operation Iraqi Freedom. Injury, 40, 772–7.

Elston, J. P., Pyo, J., & Deben, S. E. (2013). Reconstructive and Prosthetic Options for the Wounded Warrior. Current Orthopaedic Practice, 24(2), 114–119.

Fessel, G., Frey, K., Schweizer, A., Calcagni, M., Ullrich, O., & Snedeker, J. G. (2011). Suitability of Thiel embalmed tendons for biomechanical investigation. Annals of Anatomy, 193, 237–41.

Funk, J. R., Crandall, J. R., Tourret, L. J., MacMahon, C. B., Bass, C. R., Patrie, J. T., Khaewpong, N., & Eppinger, R. H. (2002). The Axial Injury Tolerance of the Human Foot/Ankle Complex and the Effect of Achilles Tension. Journal of Biomechanical Engineering, 124, 750–7.

Funk, J. R., Rudd, R. W., Kerrigan, J. R., & Crandall, J. R. (2004). The Effect of Tibial Curvature and Fibular Loading on the Tibia Index. Traffic Injury Prevention, 5(2), 164–72.

Gallenberger, K. (2013). Foot And Ankle Injuries In Variable Energy Impacts. Master's Theses, Marquette University.

Hennig, E. M., Cavanagh, P. R., Albert, H. T., & Macmillan, N. H. (1982). A piezoelectric method of measuring the vertical contact stress beneath the human foot. Journal of Biomedical Engineering, 4, 213–22.

Hirsch, G., & Sullivan, L. (1965). Experimental Knee-Joint Fractures. Acta Orthopaedica Scandinavica, 36, 391–399.

Humanetics Innovative Solutions. (2014). Legforms. Retrieved May 15, 2014, from http://www.humaneticsatd.com/specialty-products/legforms

Inaba, A. S. (1995). Ankle Injuries: A Sprained Ankle? Radiology Cases in Pediatric Emergency Medicine, 3(3).

Insurance Institute for Highway Safety. (2009). Frontal Offset Crashworthiness Evaluation- Guidelines for Rating Injury Measures. Retrieved from http://www.iihs.org/ratings/protocols/pdf/measures_frontal.pdf

Iyo, T., Maki, Y., Sasaki, N., & Nakata, M. (2004). Anisotropic viscoelastic properties of cortical bone. Journal of Biomechanics, 37, 1433–7.

Kirtley, C. (2001). An Instrumented Insole for Kinematic and Kinetic Gait Measurements. In Proceedings of the 5th Symposium on Footwear Biomechanics (pp. 52–53).

Kljajić, M., & Krajnik, J. (1987). The use of ground reaction measuring shoes in gait evaluation. Clinical Physics and Physiological Measurement, 8, 133–42.

Kuppa, S., Haffner, M., Eppinger, R., & Saunders, J. (2001). Lower Extremity Response and trauma Assessment Using the THOR-Lx/HIIIr and the Denton Leg in Frontal Offset Vehicle Crashes. In Proceedings of the 17th International Technical Conference on the Enhanced Safety of Vehicles. Paper No. 456.

Lestina, D. C., Kuhlmann, T. P., Keats, T. E., & Alley, M. R. (1992). Mechanism of Fracture in Ankle and Foot Injuries to Drivers in Motor Vehicle Crashes. Stapp Car Crash Proceedings, 36, 59–68.

Liedtke, C., Fokkenrood, S. a W., Menger, J. T., van der Kooij, H., & Veltink, P. H. (2007). Evaluation of instrumented shoes for ambulatory assessment of ground reaction forces. Gait & Posture, 26, 39–47.

McKay, B. J. (2010). Development Of Lower Extremity Injury Criteria And Biomechanical Surrogate To Evaluate Military Vehicle Occupant Injury During An Explosive Blast Event. Wayne State University Dissertations. Paper 146.

Mertz, H. (1994). Injury Assessment Values Used to Evaluate Hybrid III response Measurements. In S. H. Backaitis & H. J. Mertz (Eds.), Hybrid III: The First Human-Like Crash Test Dummy (PT-44th ed., p. 418). Warrendale: Society of Automotive Engineers.

Morris, A., Thomas, P., Taylor, A. M., & Wallace, W. A. (1997). Mechanisms of Fracture in Ankle and Hind-Foot Injuries to Front Seat Car occupants- An In-Depth Accident Data Analysis. Stapp Car Crash Conference, 41, 181–192.

NATO. (2007). Supplemental Information on Lower Leg Injury Assessment (TR-HFM-090 ed., pp. 1–22). Rijswijk, The Netherlands: North Atlantic Treaty Organization.

NATO/PfP. (2006). Procedures for Evaluating the Protection Level of Logistics and Light Armoured Vehicles, AEP- 55 (AEP- 55, V., Vol. Volume 2). Brussels, Belgium: North Atlantic Treaty Organization.

Newell, N., Masouros, S. D., Pullen, A. D., & Bull, A. M. J. (2012). The comparative behaviour of two combat boots under impact. Injury Prevention, 18, 109–12.

Ogawa, K., & Yokoyama, T. (2000). Visualization of impact force using pressure sensitive paper "Prescale." Le Journal de Physique IV, 10(9), 185–90.

Otte, D., Rheinbaben, H. von, & Zwipp, H. (1992). Biomechanics of Injuries to the Foot and Ankle Joint of Car Drivers and Improvements for an optimal Car Floor Development. Stapp Car Crash Conference, 36, 43–58.

Owens, B. D., Kragh, J. F., Macaitis, J., Svoboda, S. J., & Wenke, J. C. (2007). Characterization of extremity wounds in Operation Iraqi Freedom and Operation Enduring Freedom. Journal of Orthopaedic Trauma, 21(4), 254–7.

Quenneville, C. E., & Dunning, C. E. (2012). Evaluation of the biofidelity of the HIII and MIL-Lx lower leg surrogates under axial impact loading. Traffic Injury Prevention, 13(1), 81–5.

Quenneville, C. E., McLachlin, S. D., Greeley, G. S., & Dunning, C. E. (2011). Injury tolerance criteria for short-duration axial impulse loading of the isolated tibia. Journal of Trauma, 70(1), E13–8.

Ramasamy, A., Hill, A. M., Masouros, S., Gibb, I., Phillip, R., Bull, A. M. J., & Clasper, J. C. (2013). Outcomes of IED foot and ankle blast injuries. The Journal of Bone and Joint Surgery, 95, e25(1–7).

Ramasamy, A., Hill, A. M., Phillip, R., Gibb, I., Bull, A. M. J., & Clasper, J. C. (2011). The modern "deck-slap" injury--calcaneal blast fractures from vehicle explosions. The Journal of Trauma, 71(6), 1694–8.

Ramasamy, A., Masouros, S. D., Newell, N., Hill, A. M., Proud, W. G., Brown, K. A., Bull, A. M. J., & Clasper, J. C. (2011). In-vehicle extremity injuries from improvised explosive devices: current and future foci. Philosophical Transactions of the Royal Society of London. Biological Sciences, 366, 160–70.

Razak, A. H. A., Zayegh, A., Begg, R. K., & Wahab, Y. (2012). Foot plantar pressure measurement system: a review. Sensors, 12, 9884–912.

Richter, M., Thermann, H., Wippermann, B., Otte, D., Schratt, H. E., & Tscherne, H. (2001). Foot fractures in restrained front seat car occupants: a long-term study over twenty-three years. Journal of Orthopaedic Trauma, 15(4), 287–93.

Schreiber, P., Crandall, J., Hurwitz, S., & Nusholtz, G. S. (1998). Static and dynamic bending strength of the leg. International Journal of Crashworthiness, 3(3), 295–308.

Sensor Products Inc. (2011). Fujifilm Prescale. Retrieved January 31, 2014, from http://www.sensorprod.com/prescale/product-pages/prescale/prescale.pdf

Si, W., Yan, Z., & Liu, S. (2011). A Digital Spiked Shoes for Triaxial Force Measurement using Trigone Frustrum and PVDF. Information Technology Journal, 10(1), 140–145.

Topp, T., Müller, T., Huss, S., Kann, P. H., Weihe, E., Ruchholtz, S., & Zettl, R. P. (2012). Embalmed and fresh frozen human bones in orthopedic cadaveric studies: which bone is authentic and feasible? Acta Orthopaedica, 83(5), 543–7.

van der Horst, M. J., Simms, C. K., van Maasdam, R., & Leerdam, P. J. C. (2005). Occupant Lower Leg Injury Assessment in landmine Detonations Under a Vehicle. In IUTAM Symposium on Impact Biomechanics: From Fundamental Insights to Applications (pp. 41–49).

Welbourne, E. R., & Shewchenko, N. (1998). Improved Measures of Foot and Ankle Injury Risk from the Hybrid III Tibia. In Proceedings Of 16th International Technical Conference On The Enhanced Safety Of Vehicles (pp. 1618–1627).

Wertsch, J. J., Webster, J. G., & Tompkins, W. J. (1992). A portable insole plantar pressure measurement system. The Journal of Rehabilitation Research and Development, 29(1), 13–18.

Wiler, J. L. (2008). Diagnosis : Tibial Pilon / Plafond Fracture. Emergency Medicine News, 30(3), 42.

Zuby, D. S., Nolan, J. M., & Sherwood, C. P. (2001). Effect of Hybrid III Leg Geometry on Upper Tibia Bending Moments. SAE Technical Paper, 2001-01-01, 1–14.

2 The Effect of Posture on Forces and Moments Measured in an ATD Lower Leg

2.1 Introduction

Injury criteria are developed to relate forces measured in ATDs (Anthropomorphic Test Devices) to real injury risk to occupants of vehicles during crash or blast events. These criteria are used in evaluating and developing safety systems, and the effect of posture may influence the outcome of these injury evaluations. There is limited information on the effect of ATD initial posture on the measured forces and moments in the lower leg; most injury criteria are developed with the ankle in a neutral posture (*e.g.*, Funk et al., 2004). The effect of posture on these forces and moments, and consequent injury assessment, needs to be investigated to ensure that current practices are adequately assessing potential injury risk. Furthermore, the ankle in the ATD is represented by a simple ball joint, which likely does not accurately represent real joint kinematics; therefore, investigating the effect of posture in the ATD may also help to develop useful techniques for investigating of the effect of posture in cadaveric specimens.

The posture of the ATD ankle may affect the measured forces and moments in the Hybrid III lower leg (the current standard tool used by industry to evaluate injury risk). Parenteau and Viano (1995) showed that in quasi-static loading of the Hybrid III ankle

there was no joint moment in the natural range of motion, but this increased dramatically outside the normal range. They calculated the input torque on the ankle joint based on reaction moments and load. This necessitated knowing the moment arm between the load cell and the point of application of force. Because the load cell is not located at the joint, and due to the kinked geometry of the leg, the length of the moment arm would change depending on the posture, making it important to know the position of the ankle if the joint moment was being determined based on reaction loads. Potentiometers can be incorporated into ATD models to directly measure ankle angle, but this is not standard equipment in the Hybrid III leg. Accelerometers have been incorporated in the foot of the ATD to quantify acceleration, however integrating this data with respect to time to give position will amplify error in the signal, making it difficult to determine the actual position of the foot.

The posture of the ATD ankle is only known at the beginning of the crash or impact test. During a crash test the ATD leg will tend to stay in its initial posture until the time of impact, and it is in this initial impact where the highest and most injurious forces and moments tend to be recorded in the ATD. The standard Hybrid III foot and ankle do not contain any instrumentation, preventing the position from being recorded during the impact.

The effect of initial posture on the recorded forces and moments in the Hybrid III ATD has not been thoroughly tested. The leg and ankle angles may affect the stiffness of the leg or the transmission of moments through the ankle joint, altering the Peak Axial Force

and Tibia Index. The goal of this work was to determine if the posture of the ankle and leg affects two primary injury criteria used in crash testing: Peak Axial Force and Adjusted Tibia Index.

2.2 Methods

Impact tests were conduct on a 50th percentile Hybrid III ATD right lower leg (Humanetics Innovative Solutions, Plymouth, MI, USA) using a previously validated pneumatic testing apparatus (Figure 2-1A) (Quenneville et al. 2010). The leg was positioned such that the long axis (defined as a line connecting the knee clevis to the center of rotation of the ankle ball joint) of the leg was horizontal. The knee clevis was suspended using braided steel cable on a linear bearing, which allowed free motion in the direction of impact. The steel cable allowed the knee to freely rotate. The ATD could be positioned such that the neutral axis made an angle of up to ±10 degrees with the horizontal. The flesh analog on the lower leg was removed to allow more accurate positioning.

The ankle posture was controlled using a custom footplate, which travelled on a linear bearing along a rail parallel to the direction of impact (Figure 2-1B).

A)

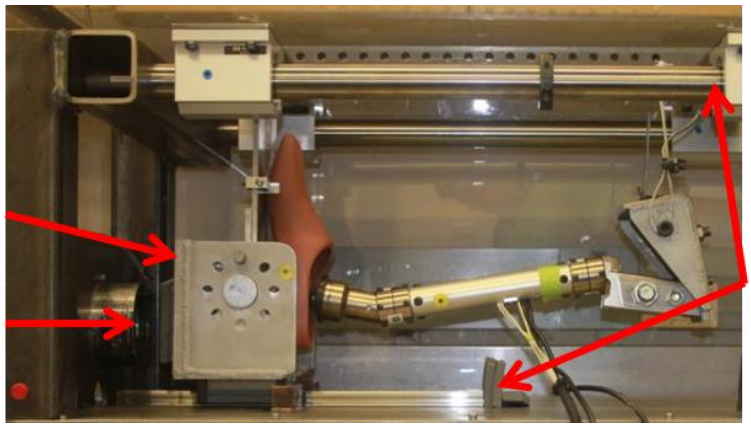

B)

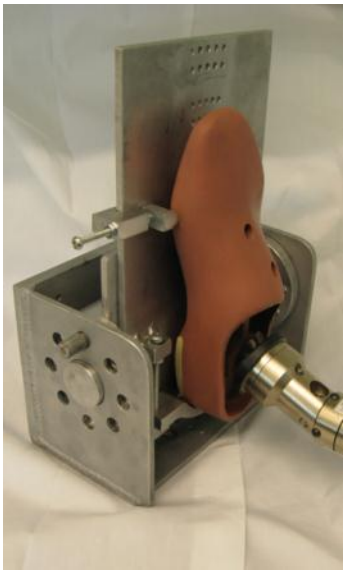

Figure 2-1- A) The pneumatic impactor with the ATD leg mounted in a neutral posture. B) The ankle positioner in a neutral posture.

The footplate allowed for independent positioning of the ankle in inversion, eversion, dorsiflexion, and plantarflexion in five degree increments representative of the range possible in the human ankle. The postures tested reflect measured ankle postures during

emergency driving maneuverers (Manning et al. 1997) to simulate ankle position just before impact, and ankle postures used in other works which performed similar impacts on cadaveric specimens (Crandall et al. 1998) to allow comparison with these works. Ankle flexion was tested in five degree increments between 20° plantarflexion and 20° dorsiflexion. Ankle eversion was tested at five degrees, and inversion at 20, 15, 10 and 5 degrees. The neutral axis of the leg was maintained in a horizontal position for all of these impacts.

The effect of tibia angle, represented by the angle of the neutral axis of the leg with respect to the impact direction, was also investigated. The neutral axis of the leg was tested at five and ten degrees above and below the horizontal (representing knee extension and flexion), where the angle was measured between the neutral axis of the leg and the horizontal. The range of angles that could be tested was constrained by the testing equipment, and likely was less than those that would typically be relevant in frontal car crash testing. However, these do represent realistic leg postures of a mounted soldier, where the impact direction is from underneath the vehicle (van der Horst et al. 2005). When simulating these postures the ankle was kept in a neutral posture with respect to the leg. For example, when the tibia angle was adjusted to simulate ten degrees above the horizontal, the footplate was adjusted to ten degrees of plantarflexion to maintain the neutral posture of the ankle.

The impactor transferred energy into the ankle positioning device through a block of foam rubber which was used to modulate the force pulse and reduce the likelihood of

mechanical damage to the apparatus. The foam block was changed after every ten impacts to mitigate any mechanical damage that might affect the load response. Five-axis load cells in the upper and lower tibia were recorded at approximately 15 kHz using a data acquisition system (National Instruments, Austin, TX, USA). An optical sensor measured the velocity of the impacting mass immediately before the impact, which was maintained at 5 +/- 0.1 m/s. Each trial consisted of five impacts at a specific posture. Three trials, with five impacts in each trial, were conducted over the course of testing with the ankle in a neutral posture to assess repeatability. The order of tested postures was randomized before testing began; however, due to time constraints, the five repeated impacts at each specific posture were conducted one after the other. The randomly selected first posture (20 degrees plantarflexion) was repeated at the end of testing, and the last posture tested on the first day (five degrees plantarflexion) was repeated at the start of testing the next day to check if the impactor performed consistently over the two test days.

The measured signals from each of the five channels on the upper and lower load cells were zeroed based on the signal before impact. Then each channel was filtered using the double two-pole Butterworth low-pass method described in Annex I- Test Protocol for Occupant Safety Measurements and Injury Assessment (NATO 2007). This involved passing the signals through a 2-pole Butterworth low-pass filter at a cut-off frequency of 1250 Hz, then reversing the signal and passing it back through the filter with the same

cut-off frequency, and finally reversing it once more to achieve a filtered signal with no phase shift.

The Peak Axial Forces (F_z) in the upper and lower load cells were determined for each impact along with the duration of the impact. The impact was considered to have initiated 1 ms before the F_{zLower} channel increased to 10% of its maximum value and finished 1 ms after the F_{zLower} fell below 10% of its maximum value. This definition of duration was not based on a standard, but produced consistent results that allowed for comparison within this work. The upper peak Tibia Index adjusted for the geometry of the ATD leg, $TI_{AdjUpper}$, was also calculated (refer to section 1.3). Unfortunately, a technical issue prevented M_{yLower} data from being recorded, making it impossible to determine the $TI_{LowerAdj}$. Therefore, the data for the upper tibia load cell formed the primary basis of evaluation for this study. However, the lower tibia load cell was still used to investigate F_z and moments about the x-axis. The five impacts for each trial were averaged, and the standard deviation was determined.

A one-way ANOVA was conducted to determine if the means from the trials associated with a set of postures differed significantly, with Tukey's Honest Significant Difference (HSD) used as a post-hoc test with $\alpha = 0.05$ to compare between each posture. The program SPSS (IBM Corporation, Armonk, NY, USA) was used to perform this analysis.

2.3 Results

A total of 110 impacts were performed. The velocity of the impacts was highly consistent, with a mean (standard deviation (SD)) velocity of 4.99 (0.08) m/s. The average impact duration was 9.9 (0.7) ms. A sample plot of the complete impact (Figure 2-2) shows four regions: pre-impact, impact, free travel of the leg along the linear bearings, and the leg reaching the end of its travel and coming to a stop.

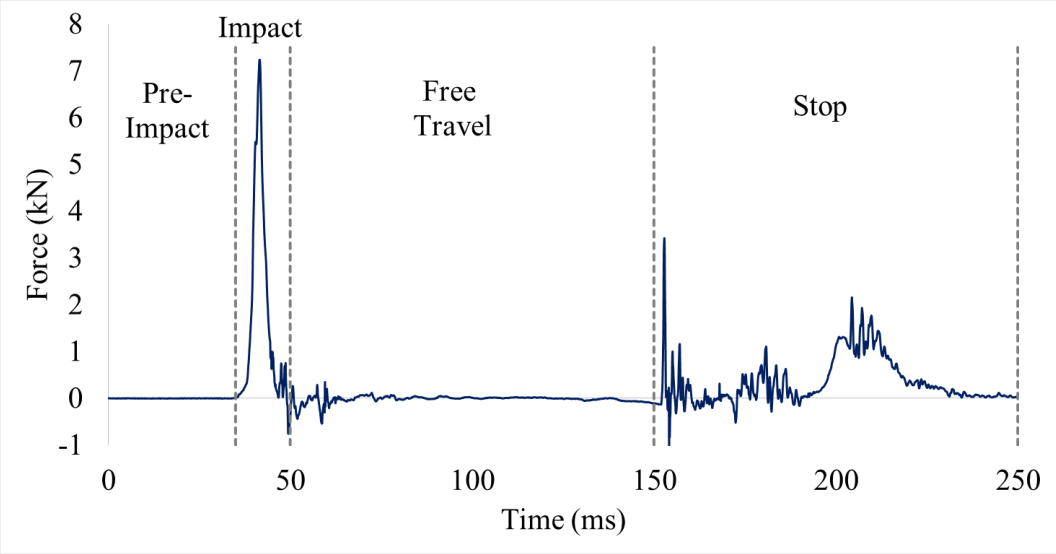

Figure 2-2- A plot of a complete impact event recorded by the F_{zLower} channel.

No significant differences among the three neutral trials were found ($p>0.5$), indicating that the testing apparatus provided consistent results across the testing period. A t-test

was performed to compare the results from the first trial with the repeated trial at the end of testing, and no significant differences were found when comparing F_{zUpper} ($p=0.948$) or $TI_{AdjUpper}$ ($p=0.556$).

The posture tested last on the first day, five degrees plantarflexion, was repeated first thing on the second day of testing. No significant difference ($p=0.154$) was found when comparing $TI_{AdjUpper}$; however, a significant difference ($p=0.006$) was found when comparing F_{zUpper}.

On average, the maximum resultant moment and maximum axial force occurred within 0.5 ms of each other. This indicates that no other collisions between parts of the leg and the testing apparatus changed the dynamics of the impact. The Peak Axial Force measured in the proximal tibia was an average of 87% (range 79-94%) of that measured in the distal tibia.

Due to the number of impacts and high sample rate, a large quantity of data was generated. For this reason, a MATLAB® program was written to automate the data analysis (Appendix B).

The average Peak Axial Force and Adjusted Tibia Index for the upper tibia are displayed in relation to postures in dorsiflexion and plantarflexion (Figure 2-3) inversion and eversion (Figure 2-4), and tibia angle (Figure 2-5).

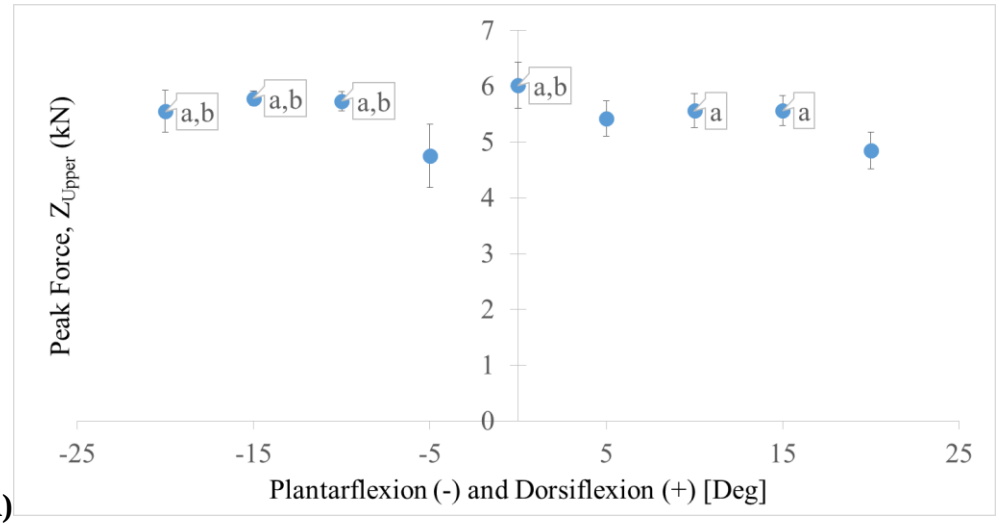

A)

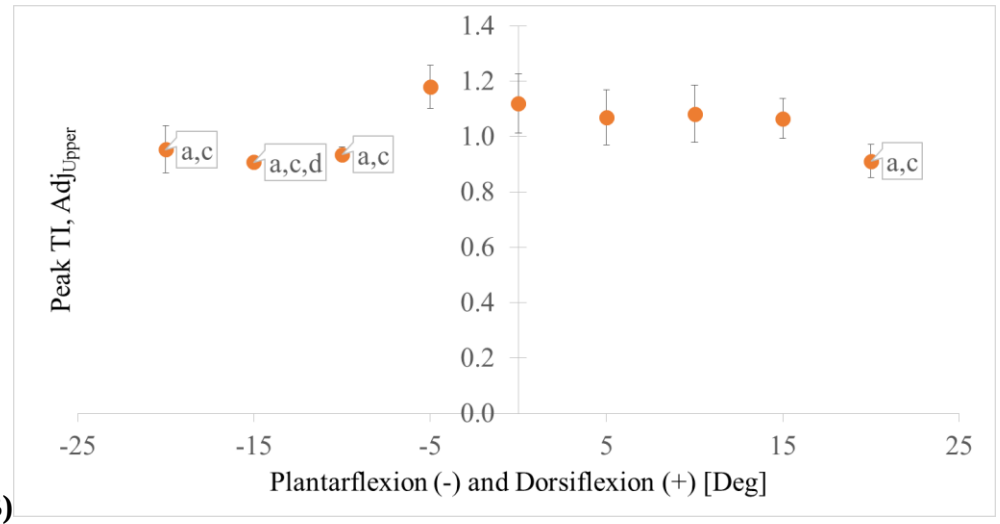

B)

Figure 2-3- The effect of ankle flexion on upper peak A) F_z and B) TI_{Adj}. a= sig diff from -5°, b=sig diff from 20°, c=sig diff from 0°, d=sig diff from 10° ($p<0.05$).

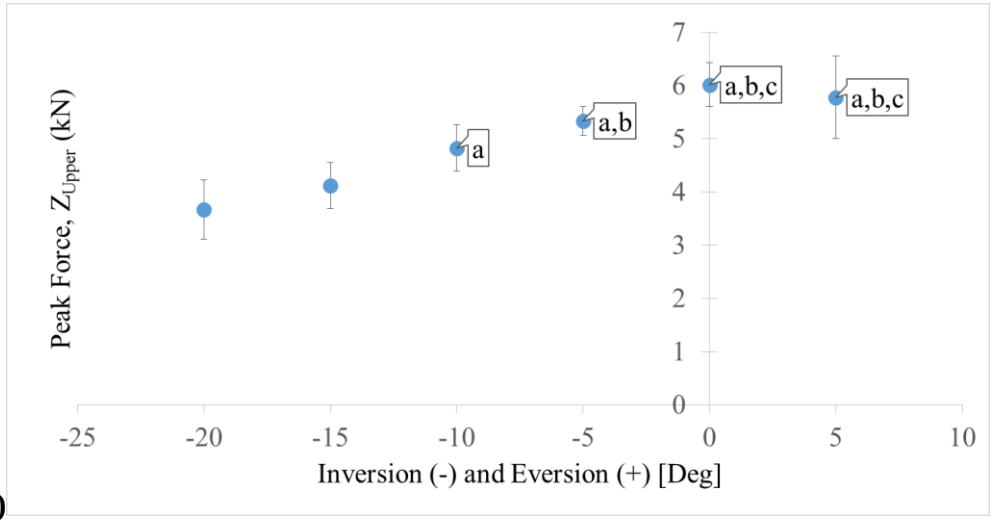

A)

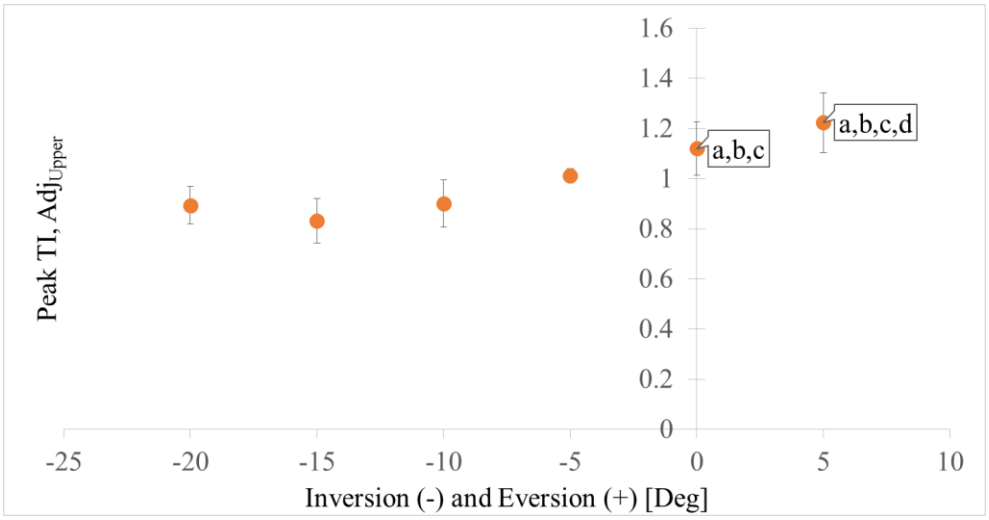

B)

Figure 2-4– The effect of ankle inversion and eversion on upper peak A) F_z and B) TI_{Adj}. a= sig diff from -20°, b=sig diff from -15°, c=sig diff from -10°, d=sig diff from -5° ($p<0.05$).

A)

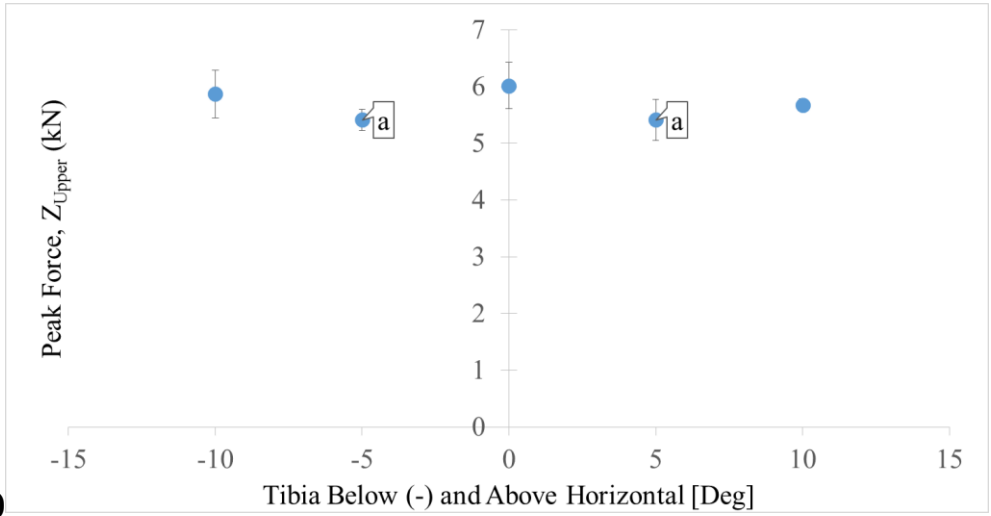

B)

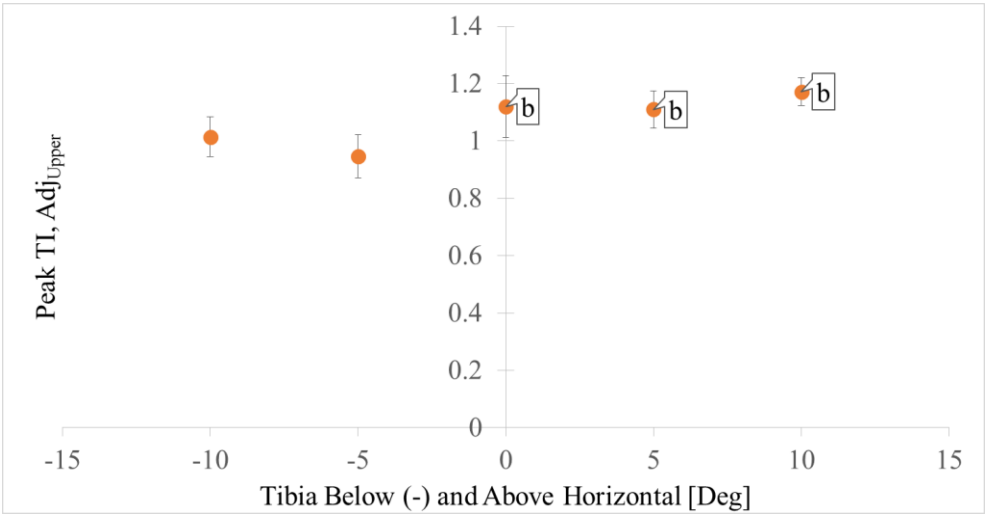

Figure 2-5- The effect of tibia angle on upper peak A) F_z and B) $TI_{Adj.}$ a= sig diff from 0°, b=sig diff from -5° ($p<0.05$).

Impact durations were consistent for postures in dorsiflexion and plantarflexion (9.89 (0.42) ms), as well as for tibia angle postures (9.59 (0.37) ms). However, in inversion and eversion, the impact durations showed greater variations with posture (10.16 (1.22) ms), which are summarized in Figure 2-6.

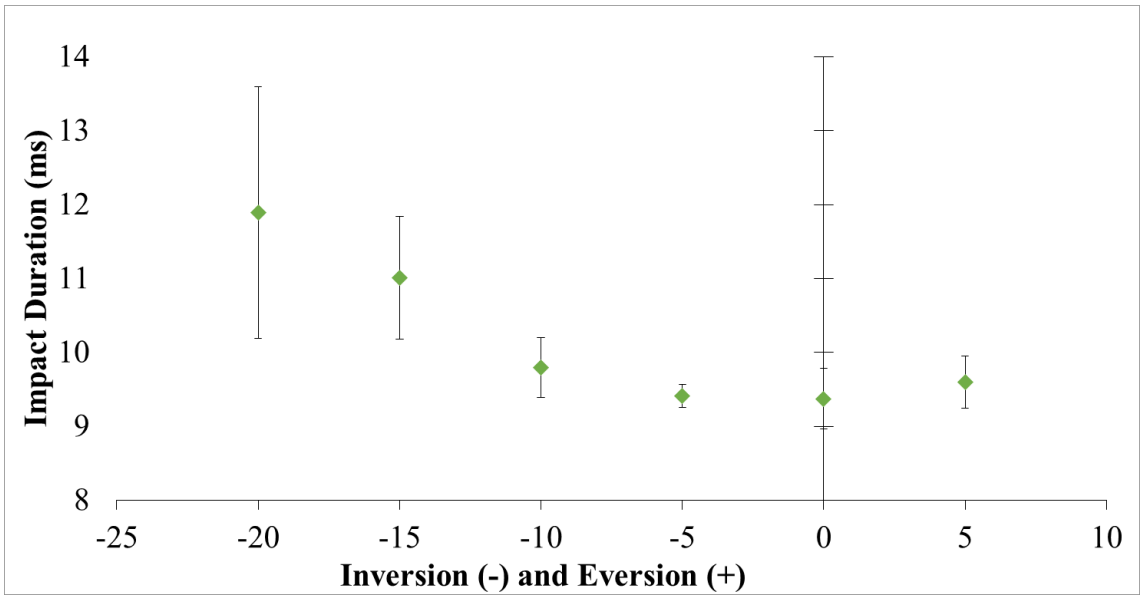

Figure 2-6- Calculated impact durations over a range of inversion/eversion postures.

2.4 Discussion

2.4.1 Effect on Injury Criteria

It has been suggested by multiple researchers that the initial posture of the leg and ankle can influence the injury risk to the lower leg (van der Horst et al. 2005; Dong et al. 2013; Crandall et al. 1998). A Hybrid III leg was subjected to impacts using a pneumatic device, and the Peak Axial Forces (average of 6 kN) and impact durations (average of 10 ms) that were recorded indicate that the experimental impact reasonably approximated a real world impact event, based on measures reported to occur in crash testing (Quenneville et al. 2011).

When the ATD ankle posture was varied across a range of postures in plantarflexion and dorsiflexion, significant differences were found in both peak $TI_{AdjUpper}$ and F_{zUpper}. These differences would have an effect on safety evaluations, although the range from the maximum value to minimum value across all postures was relatively low (F_{zUpper}: 4.8-6.0 kN, $TI_{AdjUpper}$: 0.91-1.18). Similar results were found when the tibia angle was varied (F_{zUpper}: 5.4-6.0 kN, $TI_{AdjUpper}$: 0.95-1.17). This suggests that injury measures in the Hybrid III ATD leg are relatively insensitive to the influence of these postures. It should be noted that even though this range is relatively narrow, it does bridge the NATO recommend cutoff level of 5.4 kN (NATO/PfP 2006) and IIHS recommended cutoff of a $TI < 1$ (Insurance Institute for Highway Safety 2009).

When testing the effect of inversion and eversion, significant differences were observed (see Figure 2-4), and a large range of values were recorded (F_{zUpper}: 3.7-6.0, $TI_{AdjUpper}$: 0.83-1.22). This range of outcomes would have an appreciable effect on safety ratings. The highest peak F_{zUpper} forces were seen when the ankle was in a neutral posture, and the highest $TI_{AdjUpper}$ values were seen at near neutral postures. These results both indicate increased injury risk at neutral or near neutral postures, whereas previous research with cadaveric specimens has suggested that injury risk is not influenced by initial inversion or eversion in the normal range (Crandall et al. 1998). This difference may be explained by investigating the stiffness of the Hybrid III leg, which is detailed below.

During the ATD testing in inversion and eversion, it was observed that the long axis of the tibia was forced slightly out of line with the direction of impact, when viewed overheard, due to the geometry of the leg and construction of the impacting apparatus. This effect was at its maximum at 20 degrees of inversion. This angle was small, and the corresponding component of force that would not be transmitted in the F_z direction due to this angle would also be small. This misalignment alone is likely not fully responsible for the range of peak F_z recorded over the tested postures. Instead, the slight misalignment of the leg may have affected the stiffness of the leg in the direction of impact. In neutral postures the leg is most stiff, which results in high peak forces but shorter impact durations (Figure 2-6). The reduced Peak Axial Force measured with increasing inversion and eversion could be explained by reduced stiffness of the leg, supported by

longer impact durations, at those postures. When the long axis of the tibia shaft was pushed out of plane, it was likely to bend, which resulted in a less stiff response.

2.4.2 Moments Measured in the ATD

It was noted that at the time of peak F_{zLower} the moment about the x-axis in the lower load cell, M_{xLower}, was negative in all cases. Especially in inversion and eversion it would be expected that opposite initial postures would create opposite moment arms, and therefore corresponding bending moments in opposite directions. The moment arm necessary to produce these moments due to the applied axial force, as measured by the load cell, was calculated with Eq. 2.1:

$$Moment\ arm = (\mathrm{M_{x}}_{Lower} + (\mathrm{F_{y_{Lower}}} * 0.078))/\mathrm{F_{z_{Lower}}} \qquad \text{Eq. 2.1}$$

The moment about the x-axis due to force acting along the y-axis, which acts at a distance of 0.078 m from the load cell (the distance between the center of the load cell and the center of rotation of the ankle joint), was added from the measured moment and divided by the axial force to determine the length of the moment arm. This approach for correcting the measured moment at the load cell based on forces acting orthogonally to the axial direction was first described by Kuppa et al. in 1998. The moment arms at which the axial force was calculated to have acted are plotted for inversion and eversion postures (Figure 2-7).

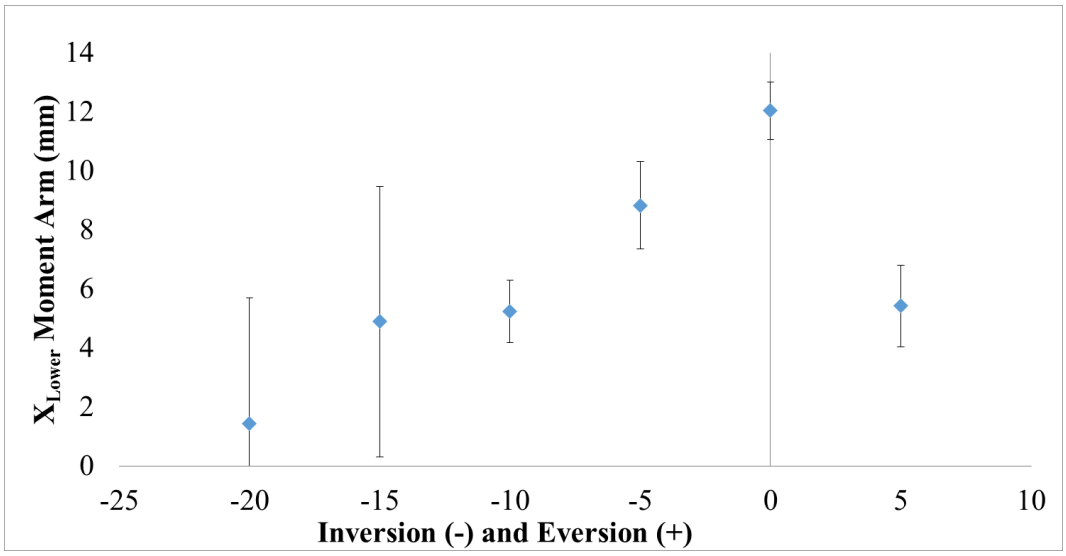

Figure 2-7- The calculated M_{xLower} moment arm over inversion/eversion postures.

The moment arms during plantarflexion and dorsiflexion were similarly calculated, and plotted on Figure 2-8.

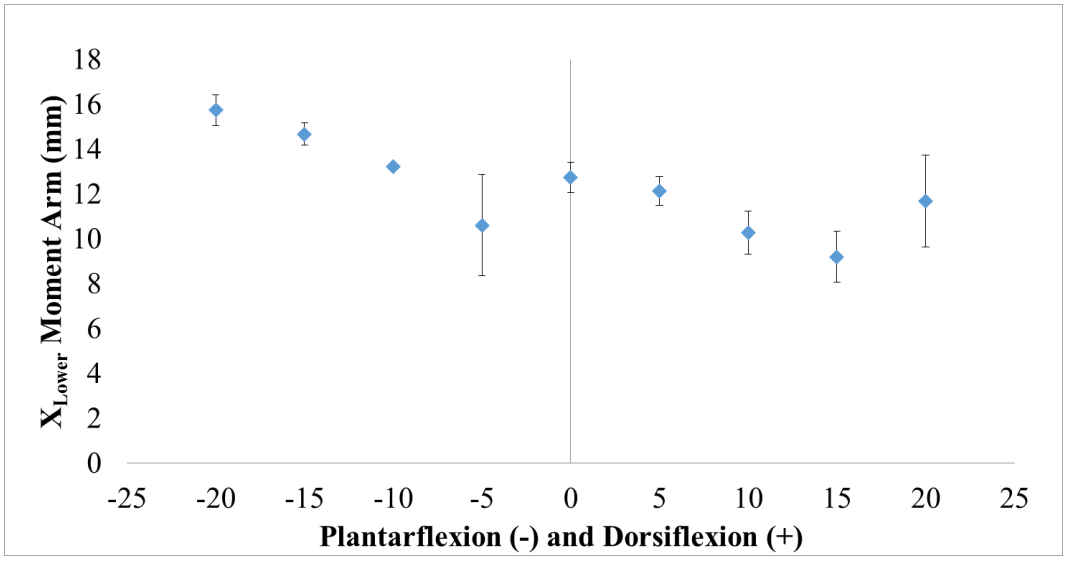

Figure 2-8- The calculated M_{xLower} moment arm over plantar/dorsiflexion.

When the M_{xLower} plots were inspected over the duration of the impact, it was noted that there were no apparent discontinuities. This suggests that the ball joint did not reach its limit during the initial impact. The calculated moment arm (Figure 2-7 and Figure 2-8) indicates that in a neutral posture the axial force was applied along a moment arm that extends approximately one cm laterally from the long axis of the right leg of the ATD used here (refer to Figure 1-4). As the ankle moved into inversion, the moment arm was shorter and when it moved into eversion, the moment arm was longer.

There are two possible explanations for this behavior. The first is that the asymmetry of the ATD foot and the way the silicone flesh analog is deposited around the metal footform tends to favor force transmission on the medial side, regardless of the posture of the foot. This seems somewhat unlikely, both because observation of the geometry of the foot does not clearly support this, and because this explanation would necessitate that the ball joint be capable of transmitting large moments. Although this may be possible to some degree had there been high frictional forces generated in the joint, it seems unlikely because the joint was generally easy to manipulate.

The second explanation is that the design of the load cell coupling to the ankle produced eccentric loading on the load cell which resulted in this consistent, erroneous reading. Figure 2-9 shows a simplified schematic of the load cell design.

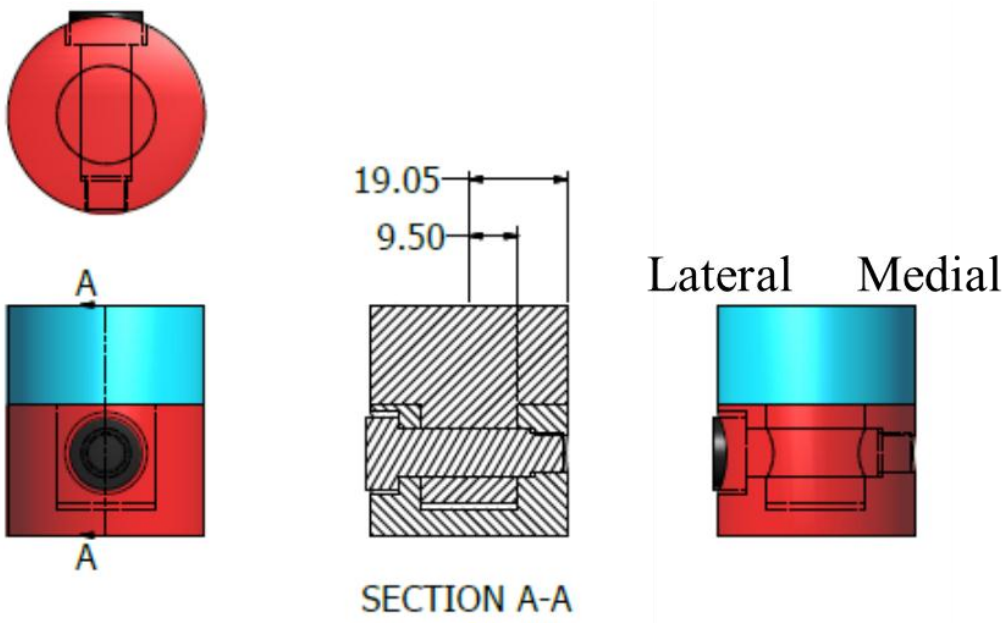

Figure 2-9- A simplified drawing (dimensions in mm) of the current arrangement used to attach the load cell (blue) to the ankle joint (red).

The bolt that pins the load cell to the ankle is threaded on one end, and has a clearance fit through the load cell and the opposite side of the ankle joint. The threaded portion of the ankle bolt is securely located, but the unthreaded portion end can deflect slightly in the clearance fit, which leads to bolt bearing the load unevenly. This explanation is supported by observation of wear on the bolt, and uneven contact noted to occur between the ankle joint and load cell (Figure 2-10).

A) **B)**

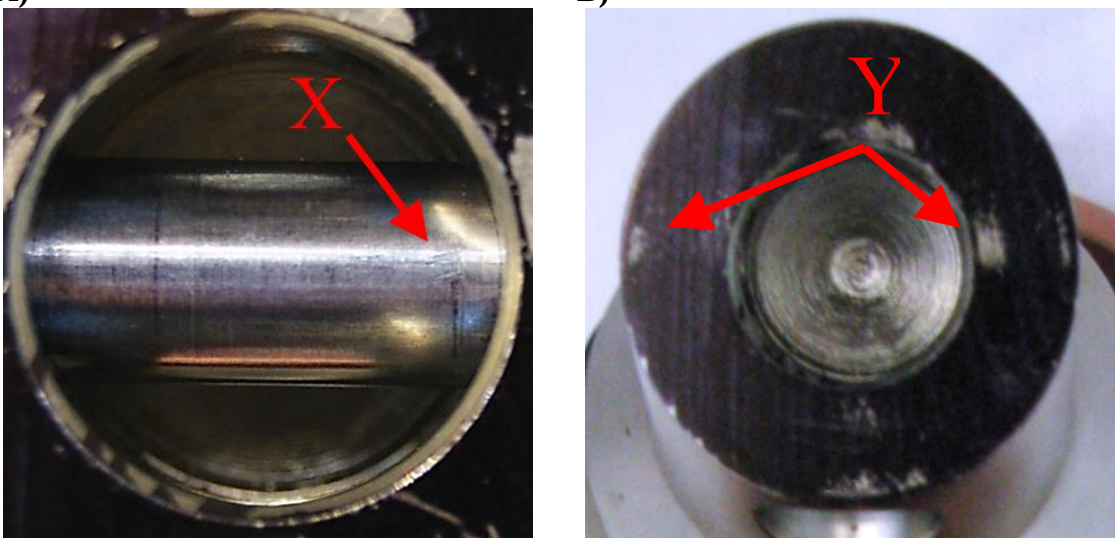

Figure 2-10- A) The ankle retention bolt showed signs of wear on the medial side at *X*. B) Paint removal at *Y* indicates that contact forces were not evenly distributed over the mating surfaces of the ankle joint.

In plantarflexion and dorsiflexion tests, the largest calculated moment arm occurred when the foot was in maximum plantarflexion. The force applied to the sole of the foot is transmitted via a steel plate, embedded in the rubber footform, to the ankle ball joint through a linkage (Appendix C). In plantarflexion, the distance between the load cell and the attachment to the footplate is at a minimum, which also minimizes the y-moment acting about the load cell. This would exacerbate the potential for eccentric loading, as the frictional forces between the load cell and ankle joint attachment would be minimized, and instead forces would be transmitted through the bolt and mating surfaces, leading to eccentric loading.

The moment arm created by this eccentric loading could explain the consistent negative moment. Through correspondence with the manufacturer of this load cell it was determined that the effect of eccentric loading has not been specifically evaluated; however, a review of the calibration fixture for this load cell suggests that an axial force may be recorded as a moment if it is applied eccentrically, even if it acts within the footprint of the load cell (Appendix D). Further investigation into the sensitivity of this load cell to eccentric loading would be beneficial, especially because new ATD legs such as the Thor-Lx use a similar load cell in a similar mounting configuration (Appendix E). One possible method to remedy this issue would involve changing the design of this connection so that contact forces on this surface are even, and that the connection is tight. This could be accomplished by installing a bolt that creates compression across the joint.

Although significant differences were seen in both peak F_z and TI_{Adj} during inversion and eversion, these differences may have been created by eccentric loading of the load cell and a change in stiffness of the leg due to slight misalignment, which are issues intrinsic to the design of the ATD leg. This means that although the leg response is affected by posture, it remains to be determined if this response is similar to what occurs when a human lower leg is dynamically loaded at various postures. The results from this work can be used to improve the design of ATD load cell connections in the future, and also serve to emphasize the importance of both axial and bending stiffness in ATD design and cadaveric testing. It is interesting to note that in every case the F_{zLower} force was larger than the F_{zUpper} force, despite the fact that the two force transducers are on the same rigid

shaft. This is likely due to the bending of the shaft absorbing some energy. This finding further emphasizes the importance of accurately representing stiffness in ATD legs.

2.4.3 Limitations

The overall variance in each posture tested was notable. Despite careful positioning of the leg, small perturbations in the initial setup seem to have had large effects on the measured outcomes. This variation under the present, highly controlled test setup indicates that different results could likely be expected in repeated crash tests, emphasizing the need to do repeat testing in the real world. Also, a high degree of care needs to be taken in initial ATD positioning prior to these impacts.

Measures were taken to evaluate whether the testing apparatus was producing consistent results over the course of testing. The three neutral posture trials performed at random times over the course of two days of testing showed no significant differences in $TI_{AdjUpper}$ or F_{zUpper}. The first posture tested was repeated at the end of testing and it also showed no significant differences. The last posture tested on the first day of testing was repeated first thing in the morning on the second day of testing. It was found that although $TI_{AdjUpper}$ did not show any significant difference, F_{zUpper} did. This difference may have been caused by the grease-packed linear bearing on the ankle positioner cooling down overnight, creating a stiffer response to impact. These were the only impacts that were performed on the "cold" impactor (the impacts on the first day were preceded by multiple impacts to achieve the correct impact velocity).

The variance in outcomes for each posture can be attributed to subtle differences in the initial posture of the leg, but also to small changes in the performance of the apparatus between impacts. Using multiple ATD legs and randomly assigning each trial for each posture to each would allow for a more robust analysis, but the availably of ATD legs and time required prevented this. As these devices are certified tools, thus necessitating a high degree of similarity among ATD legs, it is likely a reasonable assumption that varying the actual ATD leg used for testing would not dramatically affect the results of this study. Furthermore, the fact that one ATD leg and apparatus were used, along with one impact velocity and impactor mass, gives a higher degree of confidence that each impact was consistent. Testing with a greater number of ankle postures may make trends in the response of the ATD clearer. However, the postures tested in the present study are representative of the natural range of motion of the human ankle, and as such likely captured the relevant trends. Testing at multiple speeds would also give an indication of the effect of impact velocity.

2.5 Conclusions

When using an ATD to simulate a human during safety tests, consideration should be taken to position the ankle in a posture which is as close to neutral as possible, and to impact it in an axial direction. These conditions best recreate those used in developing injury criteria. The fact that posture does influence the response of the leg indicates that instrumentation to record ankle posture would be beneficial and could lead to reduced

variability in test results. Further work to investigate the response of the human ankle and lower leg to impacts in a variety of initial postures would allow the biofidelity of the ATD ankle to be better assessed and would be useful for development and validation of new models of ATD lower legs.

2.6 References

Crandall, J. R., Kuppa, S. M., Klopp, G. S., Hall, G. W., Pilkey, W. D., & Hurwitz, S. R. (1998). Injury mechanisms and criteria for the human foot and ankle under axial impacts to the foot. International Journal of Crashworthiness, 3(2), 147–62.

Dong, L., Zhu, F., Jin, X., Suresh, M., Jiang, B., Sevagan, G., Cai, Y., Li, G., & Yang, K. H. (2013). Blast effect on the lower extremities and its mitigation: a computational study. Journal of the Mechanical Behavior of Biomedical Materials, 28, 111–24.

Funk, J. R., Rudd, R. W., Kerrigan, J. R., & Crandall, J. R. (2004). The Effect of Tibial Curvature and Fibular Loading on the Tibia Index. Traffic Injury Prevention, 5(2), 164–72.

Insurance Institute for Highway Safety. (2009). Frontal Offset Crashworthiness Evaluation- Guidelines for Rating Injury Measures. Retrieved from http://www.iihs.org/ratings/protocols/pdf/measures_frontal.pdf

Kuppa, S., Haffner, M., Eppinger, R., & Saunders, J. (2001). Lower Extremity Response and trauma Assessment Using the THOR-Lx/HIIIr and the Denton Leg in Frontal Offset Vehicle Crashes. In Proceedings of the 17th International Technical Conference on the Enhanced Safety of Vehicles. Paper No. 456.

Manning, P., Wallace, W. A., Roers, A. K., Owen, C. J., & Lowne, R. W. (1997). The Position and Movement of the Floor in Emergency Manoeuvres and the Influence of Tension in the Achilles Tendon. In Stapp Car Crash Conference (pp. 195–206).

NATO. (2007). Test Methodology for Protection of Vehicle Occupants against Anti-Vehicular Landmine Effects (TR-HFM-090 ed., Vol. 323). Rijswijk, The Netherlands: North Atlantic Treaty Organization.

NATO/PfP. (2006). Procedures for Evaluating the Protection Level of Logistics and Light Armoured Vehicles, AEP- 55 (AEP- 55, V., Vol. Volume 2). Brussels, Belgium: North Atlantic Treaty Organization.

Parenteau, C. S., & Viano, D. C. (1995). A new method to determine the biomechanical properties of human and dummy joints. In International IRCOBI Conference on the Biomechanics of Impact (pp. 183–96). Brunnen. Retrieved from http://wbldb.lievers.net/10097100.html

Quenneville, C. E., Fraser, G. S., & Dunning, C. E. (2010). Development of an apparatus to produce fractures from short-duration high-impulse loading with an application in the lower leg. Journal of Biomechanical Engineering, 132.

Quenneville, C. E., McLachlin, S. D., Greeley, G. S., & Dunning, C. E. (2011). Injury tolerance criteria for short-duration axial impulse loading of the isolated tibia. Journal of Trauma, 70(1), E13–8. Retrieved from http://www.ncbi.nlm.nih.gov/pubmed/21217472

van der Horst, M. J., Simms, C. K., van Maasdam, R., & Leerdam, P. J. C. (2005). Occupant Lower Leg Injury Assessment in landmine Detonations Under a Vehicle. In IUTAM Symposium on Impact Biomechanics: From Fundamental Insights to Applications (pp. 41–49).

3 Development of an Instrumented Boot

3.1 Introduction

Injury prediction for the lower legs is based on values recorded at the lower and upper ATD tibia load cells. It is unclear whether these predictors appropriately represent injury risk to the foot and ankle. The ability to directly measure the forces applied to the foot during impact events may allow for more quantitative analysis of the potential for lower limb (particularly foot) injury during impact events. Knowledge of force magnitude and distribution on the foot could also allow for calculation of forces and moments in the ankle, which could be combined with values currently recorded in the ATD leg to allow a more detailed prediction of ankle injury. A device that is inexpensive, robust, and accurate, which can measure forces in the foot without significantly altering the dynamics of the leg, would provide insight into this issue. ATDs are typically dressed in some form of footwear during testing, so an instrumented piece of footwear would allow for measurement of these forces in a convenient package that could be applied to either an ATD or a cadaveric specimen (NATO/PfP 2006). The goal of this work was to create an instrumented boot capable of recording force magnitude and distribution on the foot during impact events.

Several devices have been developed using load cells and pressure sensitive resistors that measure forces applied to the sole of the foot (see sections 1.6.1 and 1.6.2); however, these are mainly used for analyzing gait (*e.g.*, Razak et al. 2012). Due to the much lower

accelerations in walking or standing compared to the high accelerations that occur in blast events, the inertial effects of added mass in the form of instrumentation in shoes built for analyzing gait are far less pronounced than in impact loading. The very high forces developed in impact loading would require load cells that are physically large and relatively heavy, which would affect the shape of the boot, pressure distribution on the sole of the foot, and impact dynamics. Furthermore, devices used to analyze gait using pressure sensitive resistors do not tend to fully quantify the force, but rather focus on the approximate distribution of force. While this is perfectly acceptable for gait studies, as it allows for abnormal gait to be identified, in safety testing the total force and distribution are valuable.

Piezoresistivity is a property which is characterized by a change in electrical resistance with strain. A sensor could be created using material with this property by calibrating the resistance over a range of known pressures, and then using this relationship to predict pressure (and correspondingly force) based on a measured resistance. Piezoresistive sensors are also suitable for safety testing because they are lightweight, inexpensive, and accurate (Vecchi et al. 2000). Commercially-available sensors are not designed for the levels of force anticipated in this application, and some require the purchase of custom instrumentation, making this option more expensive and adding another level of complexity to an instrumentation system. These commercial products are often used for mapping contact pressures and for conducting research (Tekscan Inc 2010). In order to

reduce cost and create a sensor which can measure loads in the desired range, a custom sensor was developed for use in the instrumented boot.

3.2 Methods

3.2.1 Sensor Design and Construction

A commercially available polymer product, Linqstat® (Caplinq Corporation, Ottawa, Ontario, Canada), was used to manufacture custom force sensors. This sheet polymer has previously been reported to have piezoresistive properties (Kalantari et al. 2012). Linqstat® is composed of particles of carbon black dispersed in a matrix of polyethylene, and is available in three different volume fractions of carbon, with different associated sheet resistances: low (50-200 kΩ/square), medium (1-50 kΩ/square), and high (<1kΩ/square). The piezoresistive properties of all three volume contents were assessed using a simple test, which consisted of applying pressure to a 161 mm^2 piece of each material using a vice, and measuring the resistance across it with a digital multi-meter. The low volume fraction polymer was found to have low conductivity along the surface of the sheet and no conductivity across the thickness of the sheet, making it unsuitable for a force-sensing purpose. The high volume fraction material was extremely conductive, and acted as an excellent conductor regardless of the applied pressure, again making it unsuitable. The medium carbon content Linqstat® showed some conductivity which increased with applied pressure. For this reason the medium content material was selected for use in the construction of the sensors.

The sensors were constructed by sandwiching the piezoresistive material between two backing plates. These plates were constructed to serve as electrodes and mechanical supports for the piezoresistive material, and were constructed of 16 gauge cold rolled steel. Steel was chosen because it has negligible electrical resistance when compared to the polymer, and is stiff enough to ensure that the forces applied to the sensor are distributed evenly over the polymer area. A less stiff material would be more likely to distort, concentrating forces on specific areas of the polymer. The thickness of the plates was limited to keep the mass of the sensors low, and to ensure that the ATD foot could still fit into the boot with the sensors in place.

The plates were cut to roughly the correct size using a band saw and then cut to final size on a milling machine. Each plate was blasted with glass bead to remove mill scale and provide a more uniform contact surface with the polymer (Figure 3-1). Eight sensors were created to cover the insole of the boot. Through strategic placement, these sensors covered all major load-bearing structures in the foot, thus reducing the possibility of alternate load pathways developing between the sole of the foot and the boot. While it was desirable to use a greater number of smaller sensors, thus increasing the spatial resolution of the boot, this number of sensors served to provide proof of concept for the design and was limited by the data acquisition equipment available. The boot could also act as a load path around the ankle due to the frictional forces between the boot and leg.

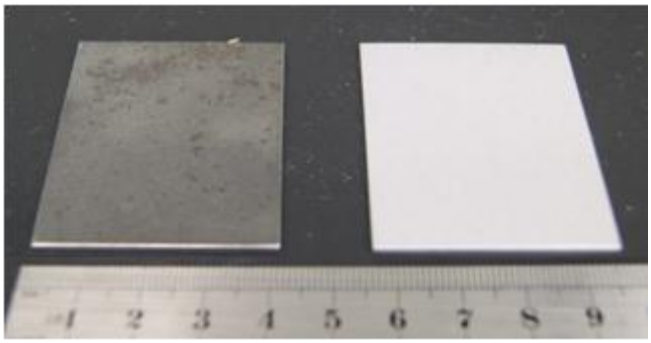

Figure 3-1- The steel plates used in the construction of the sensors, before being blasted with glass beads (left) and after being blasted (right).

Three different geometries were created (Figure 3-2) to cover the majority of the sole of the boot. Shapes A and B in this figure have the same area of 2000 mm^2, while sensor C has an area of 1000 mm^2.

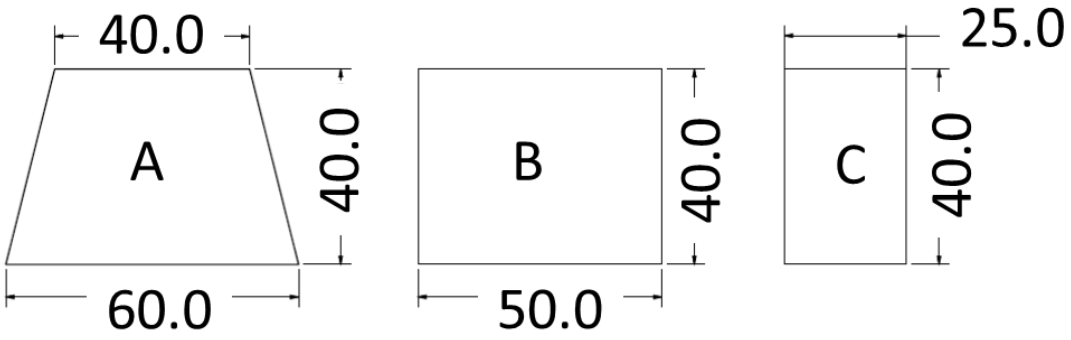

Figure 3-2- The three sensor geometries (dimensions in mm).

The areas of the foot that bear the most force in normal walking (the calcaneus, the heads of the metatarsals, and the toes) were considered to be the most important in transmission of force during impact (Hudson 2014). These areas were therefore covered with multiple sensors (Figure 3-3).

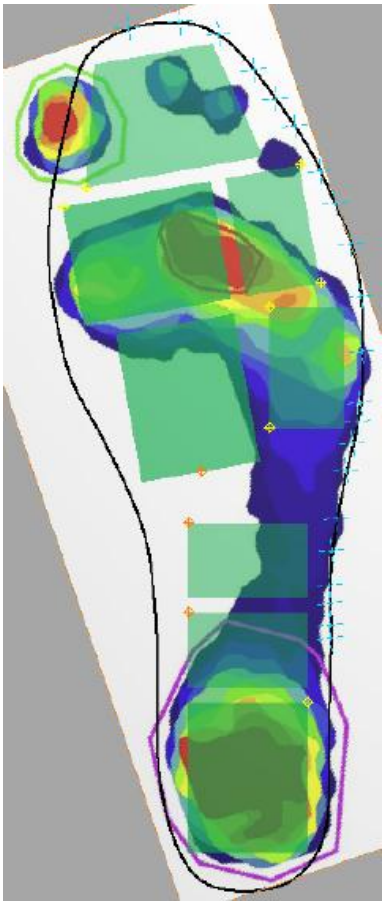

Figure 3-3- A representative diagram of pressure distribution during normal walking (Hudson 2014) with an overlay of the sensor layout.

Sheets of the piezoresistive polymer were cut to size by placing the plate on the polymer sheet, then tracing around the steel plate with a scalpel. A wire was glued to each backing plate using high conductive epoxy (CAT. NO. 83315-15G, MG Chemicals, Burlington, Ontario, Canada). The epoxy was then allowed to cure for 48 hours. Special care was taken to ensure that the insulation of the wire lay alongside the plate, and that the conductive epoxy bond was kept thin, even, and smooth. This ensured that forces applied to the plate would not be concentrated in one area by the presence of the wire. The polymer sheets were inserted between two plates and this stack was tightly wrapped with electrical tape, creating the finished sensor (Figure 3-4). Electrical tape was chosen because it kept the two plates and piezoresistive polymer aligned, but did not readily transmit load, thus preventing alternate load pathways from forming.

Figure 3-4- The completed sensor.

3.2.2 Instrumentation

Each of the eight sensor was connected in a voltage divider configuration and the voltage dividers were arranged in parallel so that they could be excited using a single power source. An example circuit diagram is shown in Figure 3-5.

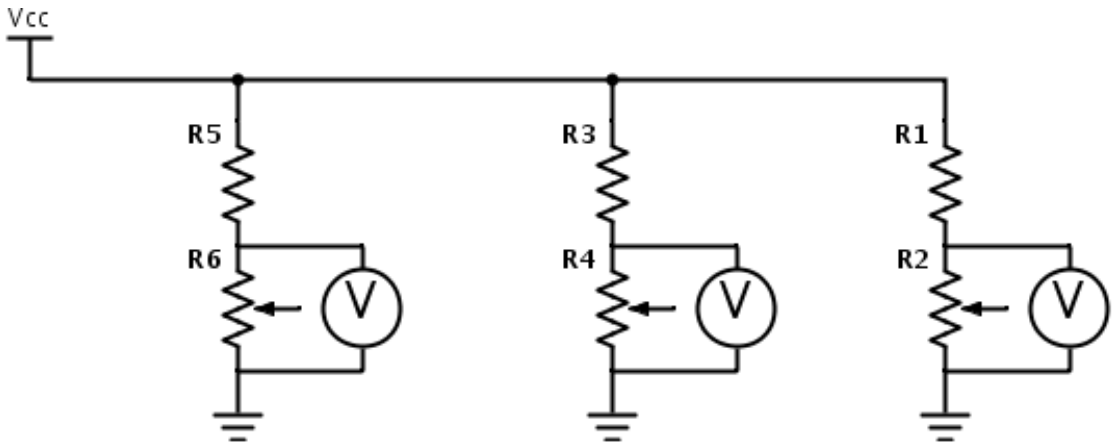

Figure 3-5- Eight voltage dividers in parallel were used (three voltage dividers are shown). R1, R3, and R5 are reference resistors, while R2, R4, and R6 represent the sensors, which vary in resistance with applied pressure.

A Vishay® 2310 amplifier (Vishay Precision Group, Shelton, CT, USA) was used to provide the excitation voltage for the sensor. The device has a maximum current output of 100 mA for continuous use. To prevent this capacity from being exceeded, the maximum current in each of the eight sensors had to be limited to 12.5mA, which was

accomplished by using a 102.0 ohm reference resistor and a 1.0 V excitation. This limited the maximum current in each arm to 10.2 mA, and the maximum total current to 81 mA. This max current would only occur if the resistance across all sensors fell to 0 ohms, which might occur if the two backing plates were shorted around the polymer. The resistance across the sensor was approximately 200 Ω when no pressure was applied. The low voltage also reduced the possibility of significant Joule heating in the piezoresistive material. A prototype circuit board was built to package these voltage dividers (Figure 3-6).

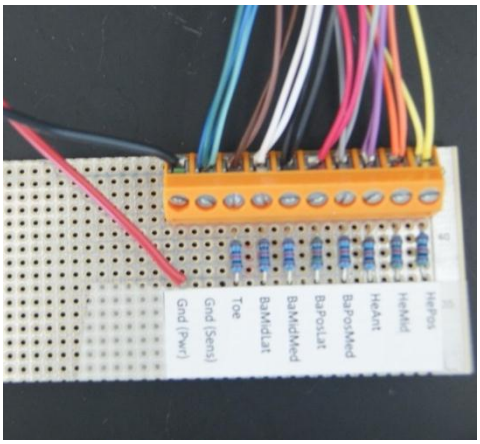

Figure 3-6- The voltage divider circuit board.

Instrumentation used for recording blast events must be able to sample at a rate high enough to properly characterize the impact. Generally, 10 kHz is recommended as the minimum sampling frequency for blast testing (NATO/PfP 2006). The data acquisition

unit (DAQ) used in this work (NI9205, National Instruments Corporation, Austin, Texas, USA) was able to sample at an aggregate rate of 250 kHz, allowing each of the eight channels to be sampled at a maximum rate of 31.25 kHz, well over the recommended rate. A LabView® program was used to record the voltage across each of the eight sensors (Appendix F).

The measured potential, the excitation voltage, and the resistance of the reference resistor in the voltage divider were used to calculate the resistance across the piezoresistive polymer sensor. The value of R_2 (Eq. 3.1) was determined by manipulating Ohm's Law, and was found to be:

$$R_2 = \frac{R_1}{\frac{V_{CC}}{V} - 1} \qquad \text{Eq. 3.1}$$

Where R_2 is the resistance across the sensor, R_1 is the reference resistor (102.0 ohm), V_{cc} is the excitation voltage (1.0V), and V is the voltage measured by the DAQ.

3.2.3 Quasi-Static Calibration of the Sensor

The electrical response of each sensor under a quasi-static compressive load was characterized using an Instron® 5940 material testing machine (Instron Corporation, Norwood, MA, USA). The force was applied with a 25.4 mm diameter circular platen in the center of the sensor (Figure 3-7).

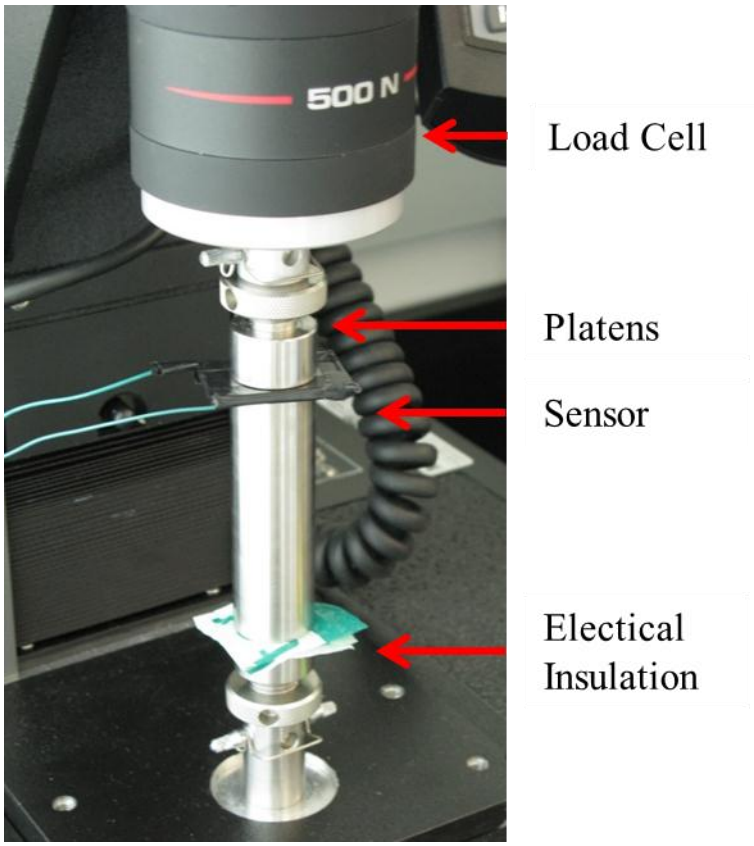

Figure 3-7- Quasi-static calibration of the sensor on the material testing machine.

The testing machine was used in position control mode, and the position was changed at a rate of 0.1 mm/min until a load of 300 N was reached. This force threshold was chosen to stay well below the maximum capacity of the load cell, which was 500 N. The sensor being tested was very stiff in compression, so slight positional errors had the potential to create large forces rapidly, potentially damaging the load cell. The test was repeated three times for each sensor with the sensors tested in a random order (Table 3.1). Between each test, the sensor was removed and replaced in the machine.

Table 3.1- The order of testing for the plates under quasi-static load.

Test #	*Plate Number*
1, 2, 3	8
4, 5, 6	5
7, 8, 9	2
10, 11, 12	7
13, 14, 15	4
16, 17, 18	6
19, 20, 21	3
22, 23, 24	1

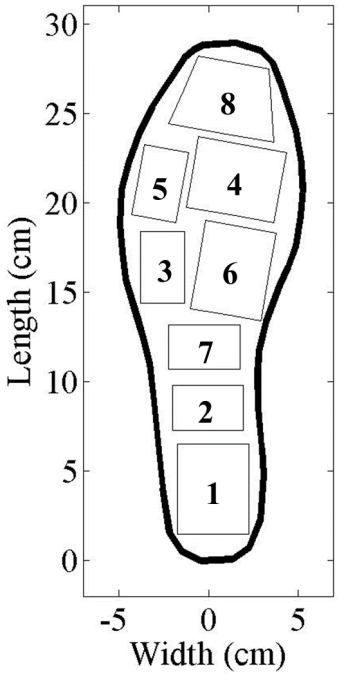

A sampling rate of 1000 Hz was used to record the potential across the sensor, and the load measured from the material tester load cell was recorded at 100 Hz.

Results from the quasi-static testing of each individual sensor were used to determine the change in resistance in response to applied pressure. The load recorded by the material testing machine was converted to pressure based on the area of each individual sensor. A pressure-resistance curve was developed for each sensor by fitting a function to the test

data. The three fits for each plate were then averaged, creating a standard curve. These steps were automated using programs written in MATLAB® (Appendices G and H).

Quasi-static testing on the edge and corner of one of the small sensors (Figure 3-2, Shape C) was performed to test the effect of eccentric loading. The corner loading was accomplished by placing the sensor in the material tester such that one corner of the sensor was aligned with the center of the circular platen of the material tester. In the side loading tests either the middle of the long or short side of the sensor was aligned with the center of the platen. The same testing parameters described above were used for these eccentric loading tests. In all, three eccentric loading positions were tested, and each test was repeated three times. All tests were performed on the same sensor.

3.2.4 Dynamic Testing of the Sensor

In order to explore the dynamic response of the sensor, an impact that more closely approximated those expected in the actual application of the boot was performed. An extra sensor (Figure 3-2, Shape C), was constructed and calibrated using the quasi-static procedure described above. This sensor was then subjected to five sharp impacts using a hammer, and was calibrated again to test that the impacts did not affect the response.

The sensor was then placed on top of a 500 lb capacity load cell (Sensortronics Model 60001-500, Vishay Precision Group, Malvern, PA, USA), which was calibrated using a 35 lb mass. A steel plate was placed on top of the sensor to evenly distribute the applied force, and a steel mass was dropped onto this plate in order to simulate an impact event.

A variety of materials were placed on top of this plate to modulate the impact. These included layers of cardboard, solid rubber sheeting, and a solid rubber bouncy ball. The voltages across the piezoresistive sensor and load cell were simultaneously recorded at 20 kHz using a DAQ.

3.2.5 Boot Construction

In the Canadian military, there are plans to adopt a standard combat boot, manufactured by Kodiak® (Kodiak Group Holdings Corporation, Cambridge, Ontario, Canada) (Levesque 2013). In order to replicate the footwear that may be used by soldiers, a Kodiak® Quantum II boot was used in the present work. A size 11 boot was found to best fit the foot of the Hybrid III 50th percentile male ATD, which has a specified length of 10.2±0.3 inches and breadth of 3.9±0.3 inches (Mertz 1994).

The sensors were installed directly onto the puncture-resistant, fiber-reinforced polymer plate in the sole of the boot. This puncture-resistant plate is standard in all CSA certified work boots (Canadian Centre for Occupational Health and Safety 2010). The sensors were laid out on the insole of the boot in the configuration shown in Figure 3-8.

Tape was used to temporarily position the plates on the underside of the insole while silicone adhesive (GE All Purpose Silicone I, SE1124, Huntersville, NC, USA) was applied in a thin coat and allowed to set for 24 hours to adhere the sensors to the puncture-resistant plate. This adhesive was chosen due to its flexibility, which allows for some movement of the sensors, thus preventing them from bending or delaminating when

the puncture resistant plate flexes, but holding the sensors in position during insertion of the foot into the boot. The boot itself prevented large motions of the foot relative to the sensors, and the force of the impact was expected to occur primarily in the axial direction, thus limiting the amount of shear force on the sensors and the adhesive holding them in place.

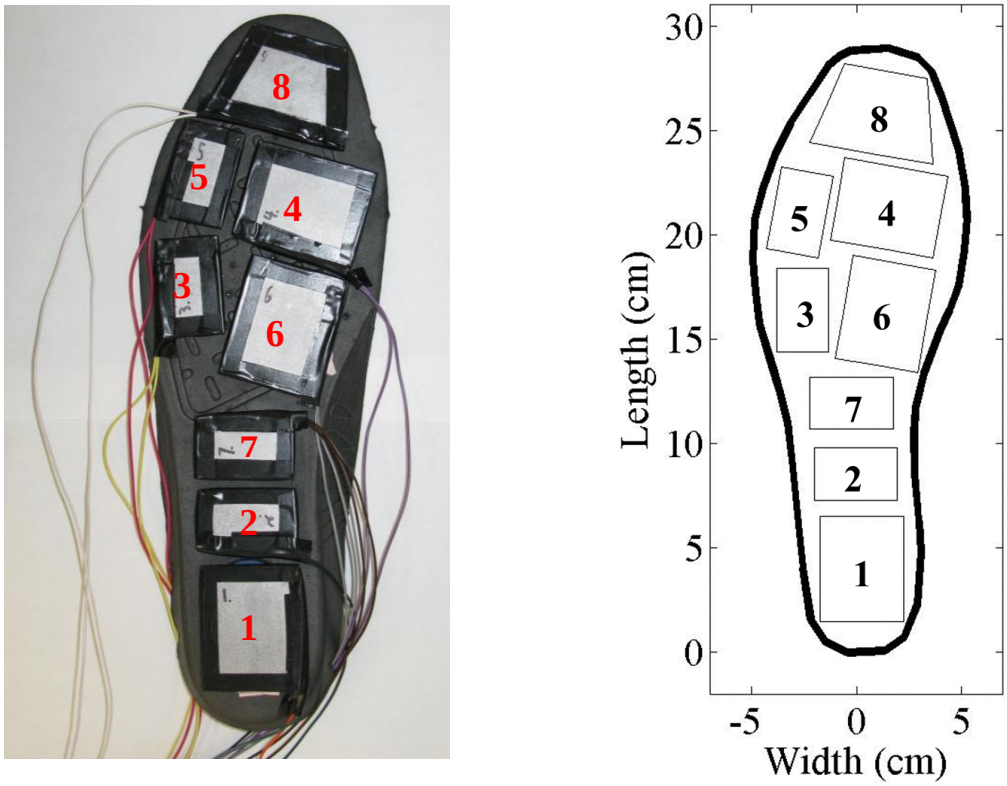

Figure 3-8- The sensors and their relative positions as they were installed on the sole of the boot.

3.2.6 Quasi-static Testing of the Assembled Boot

The ability of the boot to measure forces applied to the foot of the ATD was first quantified by applying a quasi-static load. A bracket was manufactured to position the leg in an Instron material testing machine with an AMTI MC3A load cell, which has a maximum axial force capacity of 4450 N. The leg mount was designed to hold the leg in a position such that the line that passes through the center of rotation of the ankle ball joint and the center of the knee clevis would intersect the center of the AMTI load cell and be parallel to the axis of compression on the material testing machine. The proximal end of the leg was fixed to the load cell on the material testing machine (Figure 3-9).

The flesh analog was left on the ATD leg to better position the leg in the boot, and a thin cotton sock was placed over the foot to create a low friction surface that allowed the foot to more smoothly insert into the boot. The leg was inserted into the boot and the boot was laced up in the normal manner.

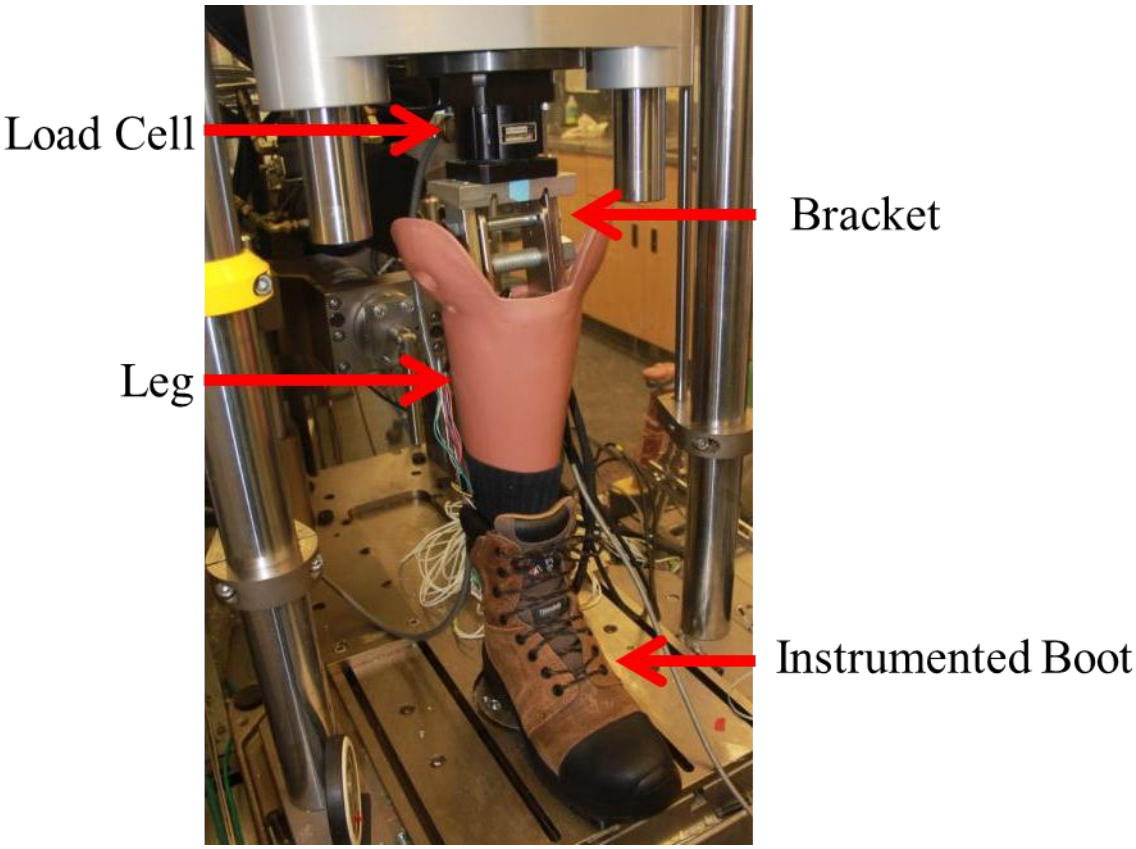

Figure 3-9- The boot and leg installed in the material testing machine.

Compression was applied in position control at 2 mm/min until the load threshold was reached. Three different load thresholds were used, and the test at each load threshold was repeated three times. After the last test the leg was removed from the boot, reinserted, and tested again to evaluate the reproducibility of the setup. This was then repeated once more. This was done to assess whether the manner in which the foot was inserted into the boot had an effect on the recorded forces. The order of testing, which was randomly determined, is shown in Table 3.2.

Table 3.2- Load thresholds used in the quasi-static tests.

Test #	*Load Threshold*
1	500
2	1000
3	250
4	500
5	1000
6	250
7	250
8	1000
9	500
10	500 (retest)
11	500 (retest)

The materials testing machine's load cell, eight boot sensors channels, and the ten channels from the two load cells in the leg were recorded at 100 Hz. In order to synchronize the two data acquisition systems (one for the boot, the other for the material tester and ATD), an extra channel on the boot sensor DAQ was used to monitor an output channel of the ATD DAQ. A digital pulse on this channel was generated when the material tester started. The measured voltage from the DAQ was collected using a

LabView® program (Appendix F), and was converted to force and analyzed using a MATLAB® program (Appendix I).

3.2.7 Dynamic Testing of the Assembled Insole and Leg

The boot was tested in dynamic impacts by mounting it on the leg in the same manner as described in the quasi-static testing. In this case, the flesh analog was removed to allow for better visualization of the position of the leg in the impactor. The leg was then installed in the pneumatic impactor detailed in Section 2.2 (Figure 3-10).

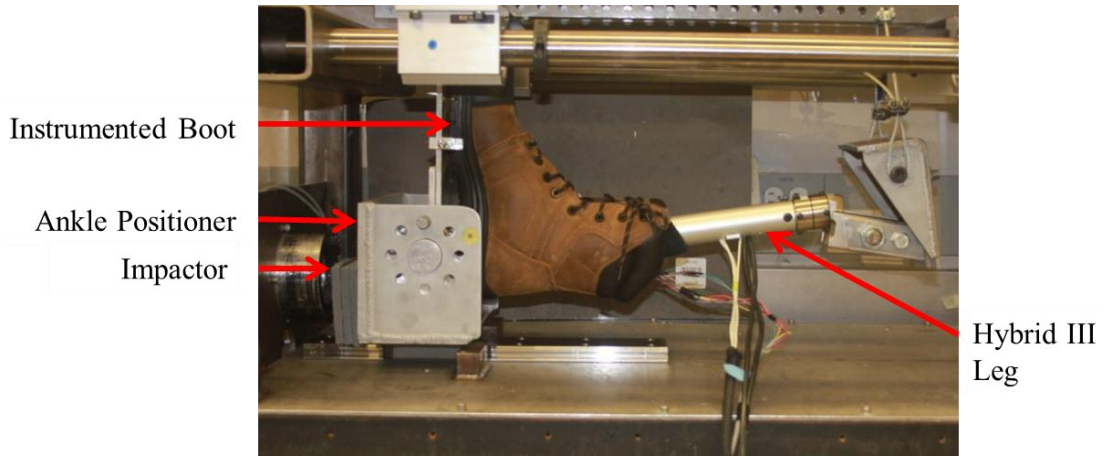

Figure 3-10- The boot and ATD leg in a neutral posture in the pneumatic impactor.

All impacts were conducted at a velocity of 5.0 +/- 0.1 m/s. The piezoresistive boot sensors were sampled at 20 kHz and the ATD leg was sampled at approximately 15

These differing sampling rates represent the maximum rates allowed by the DAQs being used. Tests were conducted at the extremes of the postures tested in the previous ankle posture study (Chapter 2), with three tests being run at each posture. impacts that were conducted are summarized in

Table 3.3. Neutral testing was conducted at the beginning and end of the testing, while the order of the other tests was randomized. Because the ankle was obscured by the boot, the neutral posture of the leg was confirmed by measuring the angle of the long section of the ATD leg using a sine bar and level; the tibia was considered to be in a neutral posture when this portion made an angle of 8.3 degrees with the horizontal. Before the last two neutral impacts, the boot was removed and replaced on the ATD leg to determine if the methods used to dress the leg with the boot affected the measured results.

Table 3.3- The postures tested under dynamic conditions.

Test #	*Posture*
1, 2, 3	Neutral
4, 5, 6	5° Inversion
7, 8, 9	15° Plantarflexion
10, 11, 12	5° Eversion
13, 14, 15	20° Inversion
16, 17, 18	15° Dorsiflexion
19, 20, 21	Neutral
22, 23	Neutral (retest)

The measured voltage from the DAQ was recorded using the aforementioned LabView® program, and was converted to force and analyzed using a MATLAB® program (Appendix J).

The resistance change in each sensor was converted to a stress based on the standard curve for each sensor, which was determined during the quasi-static calibration of the individual plates (Section 3.4.1). This stress was then converted to a force based on the area of each sensor. The sum of forces from the sensors in the boot was compared to the force measured by the material testing machine load cell and the ATD lower leg load cell.

3.3 Results

3.3.1 Quasi-Static Calibration

The pressure-resistance curve of each test was fitted with a function of the form of Eq. 3.2. This function was found to best match the pressure-resistance curve over the range of pressures tested herein.

$$Pressure\ (Pa) = \mathrm{a} * \mathrm{Resistance}\ (\Omega)^{\mathrm{b}} + \mathrm{c} \qquad \text{Eq. 3.2}$$

The small plate geometry and large plate geometry produced similar curves, although a higher pressure was achieved with the smaller plate because the maximum force that could be applied by the material testing machine was limited to 300 N (Figure 3-11). The coefficients for all fits for all tests can be found in Appendix K.

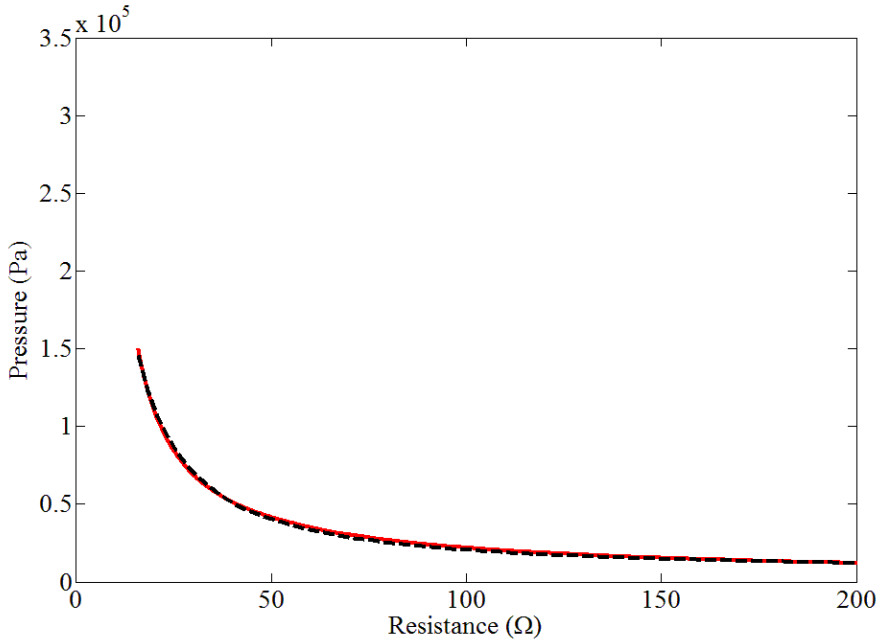

A)

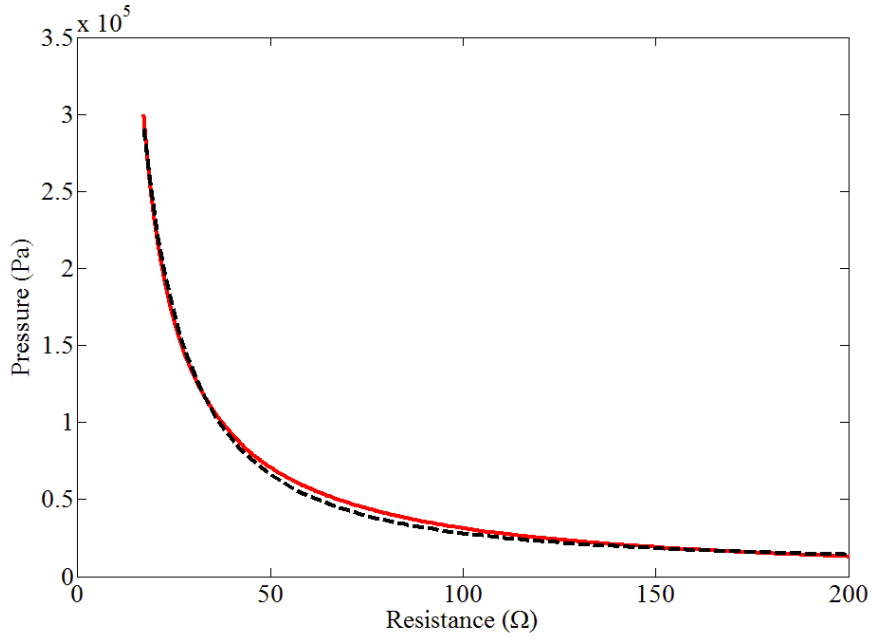

B)

Figure 3-11- Representative calibration curve of A) test 1 for plate 1, a large plate and B) test 2 for plate 2, a small plate. The red line is the experimental data, and the black line is the fit.

The three tests on each sensor produced similar results. The fits for each of the three tests for each sensor were averaged (Figure 3-12) and a curve was fit through this average to produce the final calibration curve that related resistance to pressure for a given sensor.

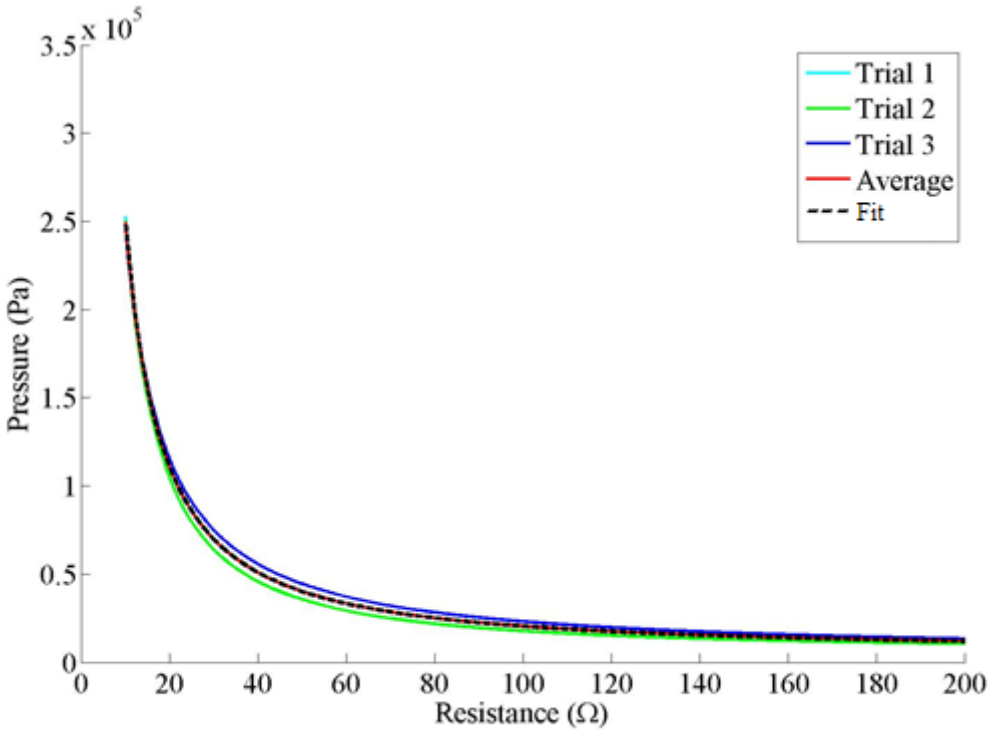

Figure 3-12- The three calibration curves from the tests on plate 1 were averaged and fit with a curve.

The sensor used for dynamic testing was calibrated before impacting, post impacting, and in eccentric locations (Figure 3-13). The calibration curves were similar before and after

the impact tests; however, eccentric loading did affect the response of the sensor, with the effect being most pronounced for loading at the corners, and least pronounced for loading at the center of the long edge.

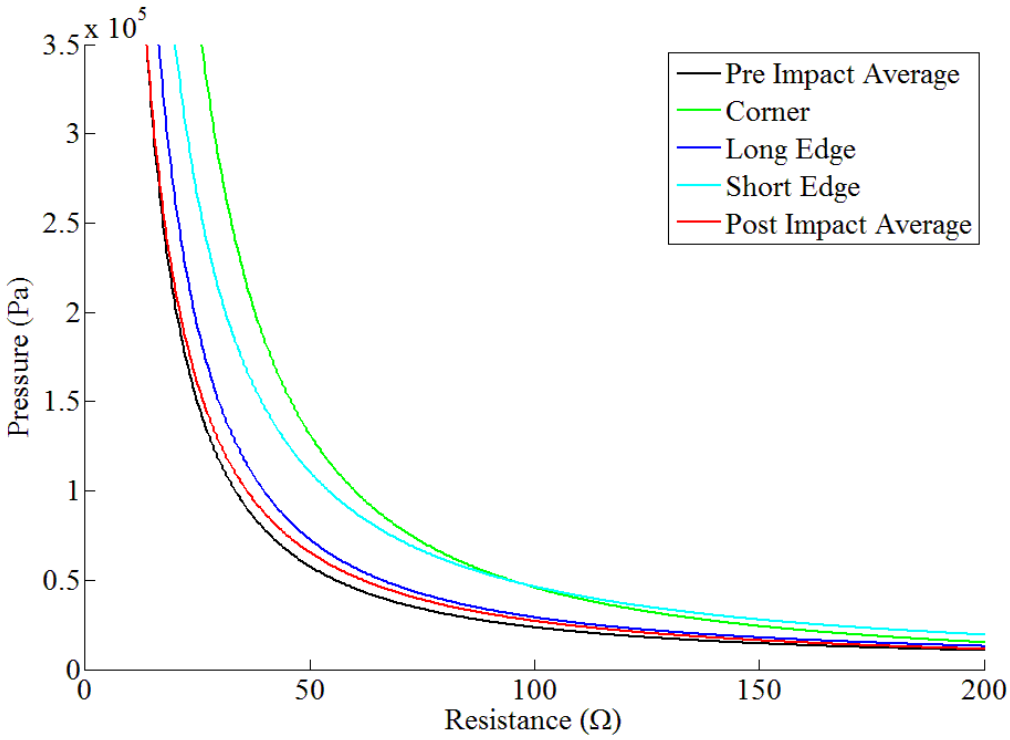

Figure 3-13- Average calibration curves for testing before and after impacts, and with eccentric loads.

3.3.2 Dynamic Testing of the Sensor

In dynamic loading, the piezoresistive sensor was able to accurately record the shape of the impulse, but not the magnitude of the force. In the majority of tests, the piezoresistive sensor recorded a force of about a fifth of that which was recorded in the load cell (Figure 3-14). In other tests, the piezoresistive sensor recorded a force of about a tenth of that which was recorded in the load cell.

The piezoresistive sensor was noted to have excellent sensitivity to small force changes; corrugated cardboard was used to shape the impact in Figure 3-14A, and the roughness of the plot is likely due to layers of cardboard collapsing. In Figure 3-14B, the impact was shaped with a solid piece of rubber, so the plot is very smooth. These differing materials were used to create differing force profiles during impacts.

A)

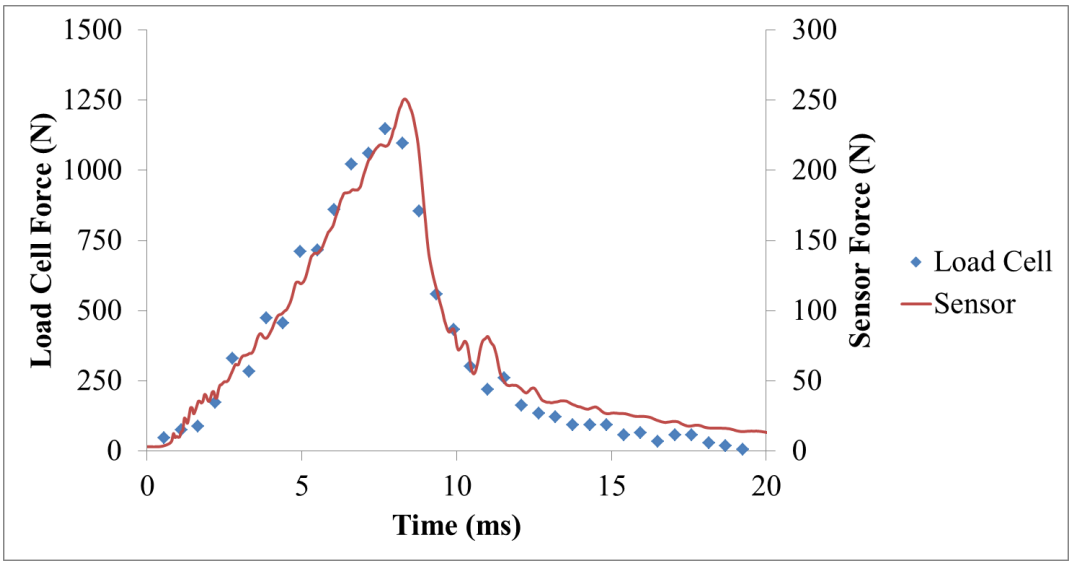

B)

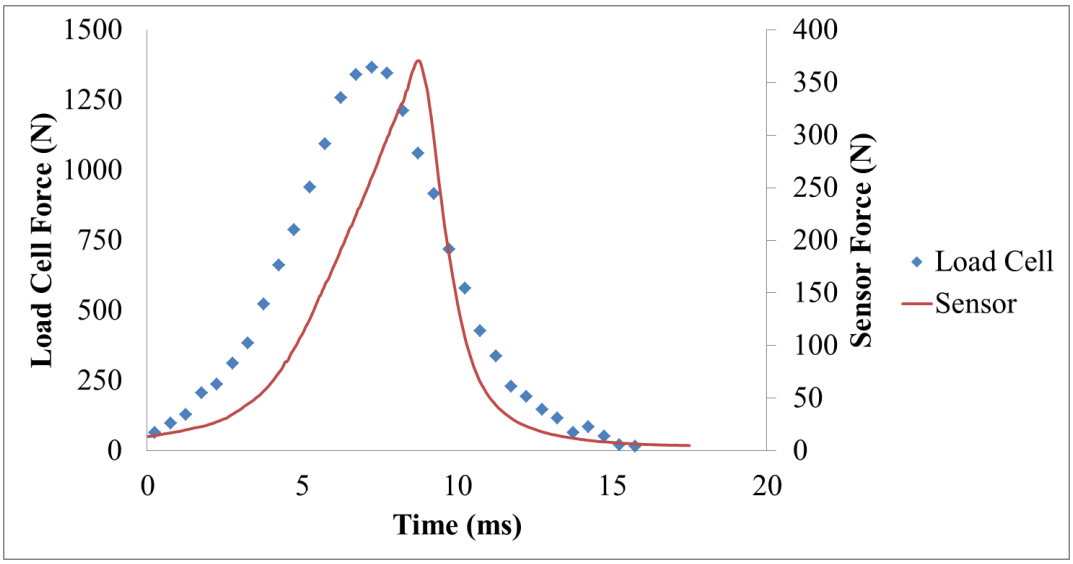

Figure 3-14- Two drop tests comparing the force recorded in the sensor and the load cell. The impact was modulated with A) corrugated cardboard and B) rubber. In A the factor of difference was 5, while in B the factor of difference was 3.75.

3.3.3 Quasi-static Testing of the Boot

The boot captured an average of 80% of the work captured by the load cell (Table 3.4). The work was calculated by integrating under the force-displacement curve for the material tester load cell, and for each of the sensors in the boot, which were then added together. The material tester force curve was fairly linear for each of the tests; however, the slope of this load cell curve was found to increase over the course of testing, as can be seen in Table 3.4.

Table 3.4- The slope of the load cell curve and percent work captured for each test.

Test Number	*Threshold (N)*	*Slope of load cell curve (N/mm)*	*% Work Captured*
1	500	54	55
2	1000	97	89
3	250	151	65
4	500	171	89
5	1000	149	79
6	250	175	87
7	250	160	60
8	1000	160	96
9	500	178	100
10*	500	72	80
11*	500	68	77
		Average:	80

**leg was removed and reinserted into boot*

The percentage of the total force that each sensor recorded was calculated, and this value was averaged over the 11 trials (Table 3.5). These consistently showed the highest force to be measured at the heel and in the lateral forefoot (sensors 1, 2, and 3). The proportion of the total force each sensor bore was found to be relatively consistent throughout the test, regardless of the total force magnitude.

Table 3.5- The average percent of the total load that each sensor recorded over the course of the quasi-static testing.

Sensor	*Average % Load**	*Average St Dev*
1	47.6	5.7
2	10.5	3.4
3	13.7	5.1
4	4.0	1.7
5	1.8	0.8
6	6.6	1.1
7	1.0	0.5
8	0.0	0.0

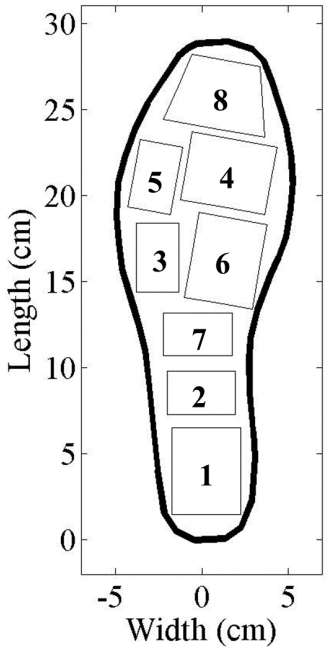

**The sum of % load is less than 100%, as each value is an average of 11 trials; the sum for each individual trial was 100%.*

In some of the tests, the boot force closely approximated the load cell force, but in others a sudden force offset between the two curves appeared. In Figure 3-15, Test 8 showed good agreement between the boot and load cell, while in Test 5 a drop in boot force was seen at 0.5 mm and 3.5 mm.

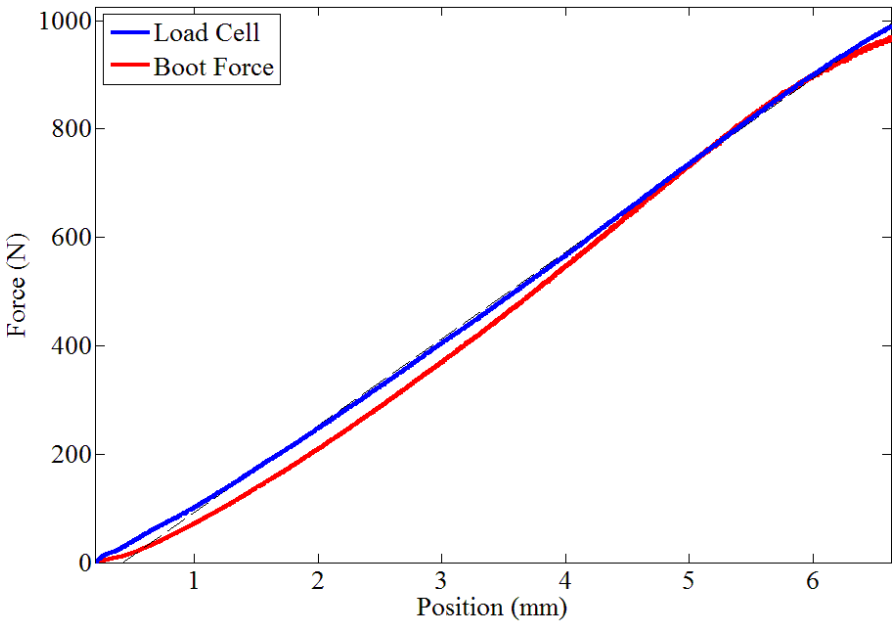

A)

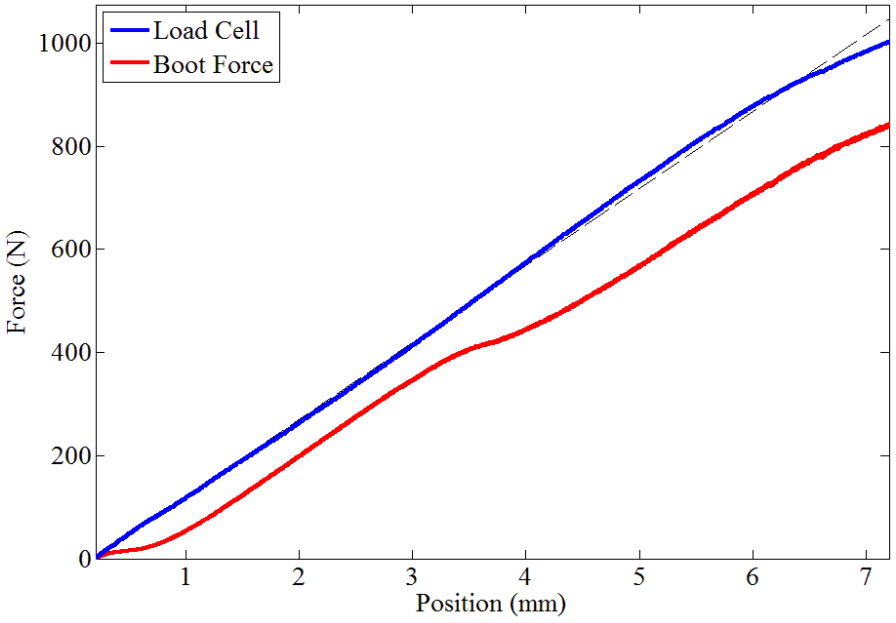

B)

Figure 3-15- The force recorded by the material tester load cell and the total force recorded by the boot sensors during A) Test 8 and B) Test 5.

3.3.4 Dynamic Testing of the Boot

The impact velocity during the dynamic testing was highly consistent, with a measured mean (SD) velocity of 5.00 (0.08) m/s. The average impact duration when performing dynamic impacts with the boot on the ATD leg was 15.7 (1.2) ms. The neutral impacts before and after refitting the boot were not significantly different when measured by the boot ($p=0.577$) or by F_{zLower} ($p=0.664$), and were therefore grouped. When examining F_{zLower}, neutral posture impacts at the beginning of testing were found to be significantly different from the neutral posture impacts at the end of testing after refit ($p=0.048$) but not before refit ($p=0.094$). When total boot force was examined, neutral posture impacts at the beginning of testing were found to be different than impacts at the end of testing, both before and after refit ($p=0.002$ and $p=0.007$, respectively) (Table 3.6).

Table 3.6- Neutral Testing Before and After Impact Testing.

	F_{zLower} (N)		*Total Boot Sensor* (N)	
	Average	*Std Dev*	*Average*	*Std Dev*
Start Impacts	3250	115	349	6
End Impacts	2881	42	251	16
After Refit	2742	335	267	28

A MATLAB® program was written to interpolate the force between the sensors during the impacts, allowing for better visualization of the impacts. The program also was used to create a movie of the measured forces during the impact (Appendix L). This video can be viewed online at: *http://youtu.be/55N0nZMzPNo*. Figure 3-16 visualizes the force distribution at four time points over the course of an impact with the leg in a neutral posture.

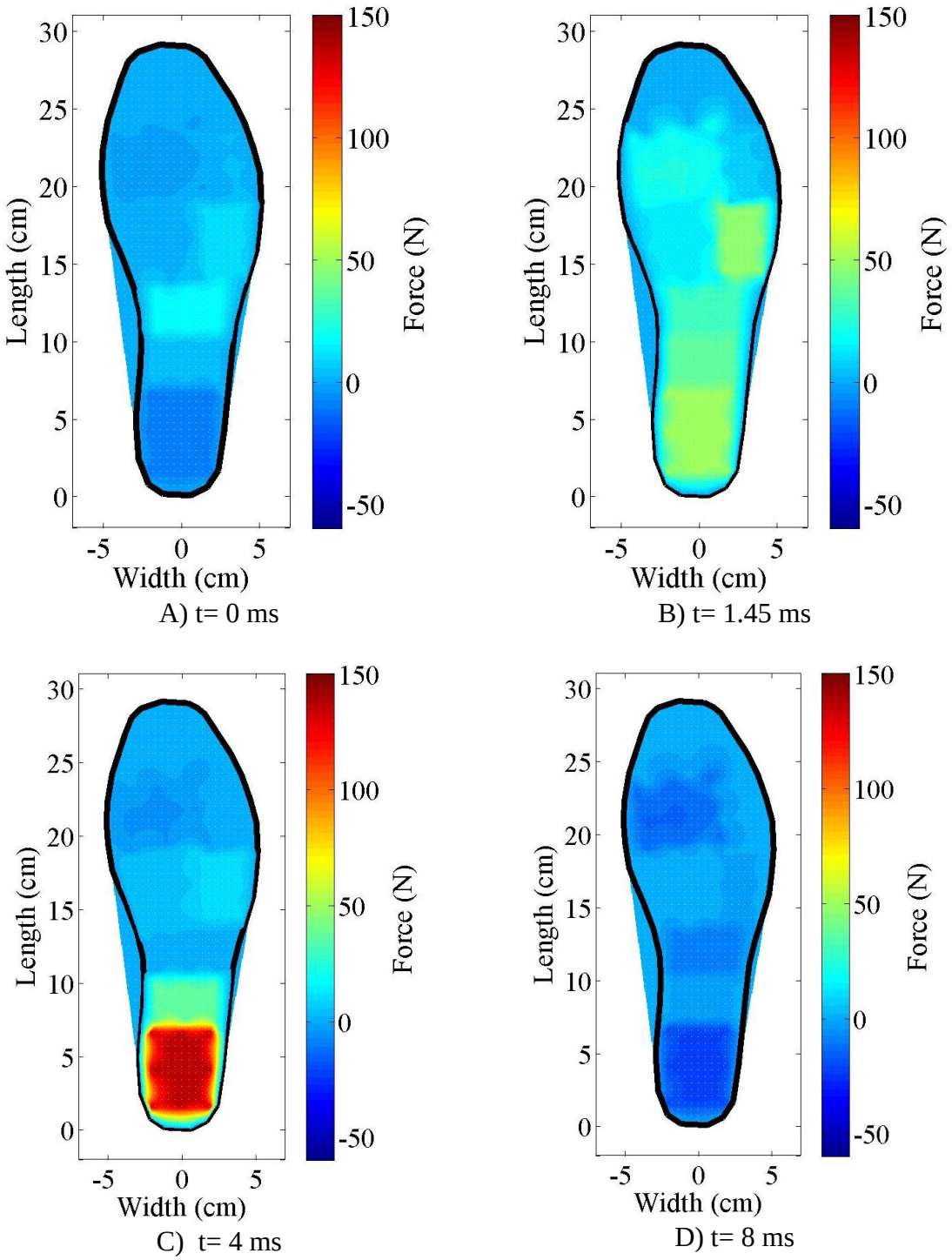

Figure 3-16- The distribution of forces over the sole of the foot during the impact.

Time= 0 is defined just before impact occurs.

The force recorded in the boot matched the general shape and duration of the forces recorded in the ATD leg, with the notable exception of a negative dip early in the impact on the boot sensor curve that corresponded to a sharp peak on the F_{zLower} curve measured at the same time (Figure 3-17). This dip and peak coupling was seen in all of the dynamic boot impacts. Also, the resting value for the boot force was offset from zero after the impact by approximately 100 N.

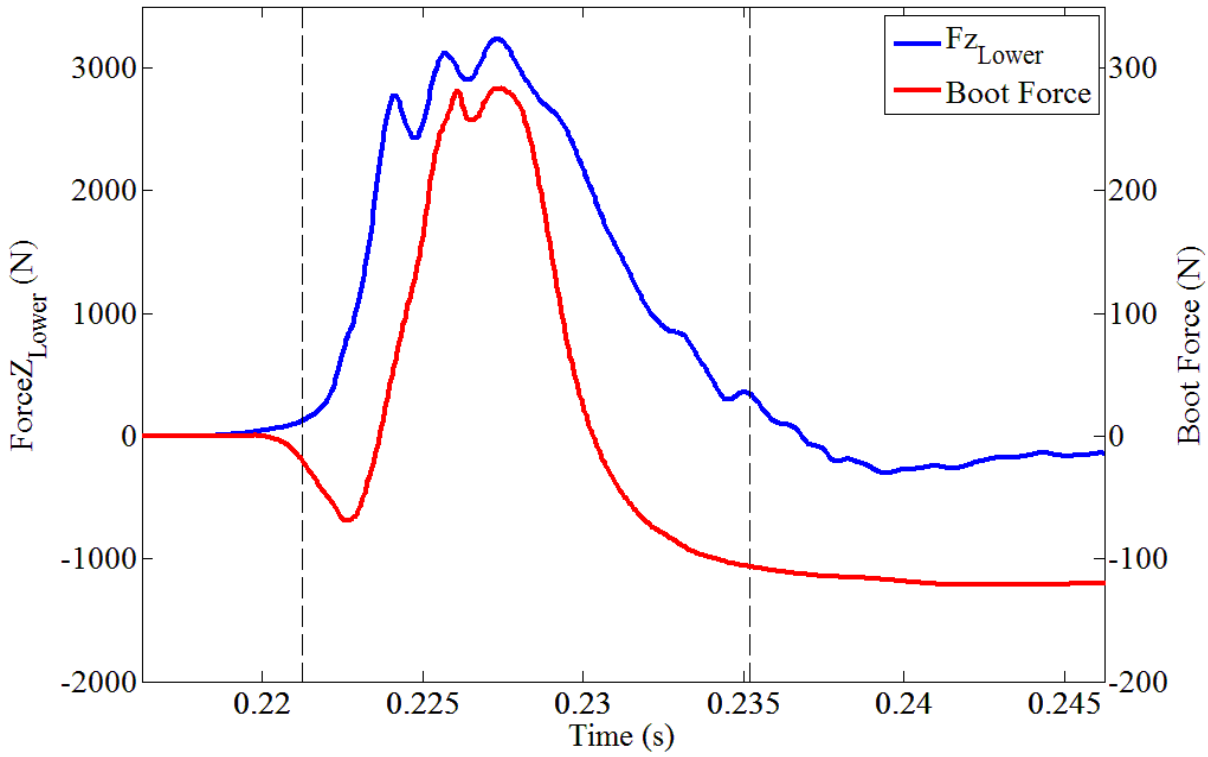

Figure 3-17- The force curve from the F_{zLower} channel of the ATD and the total measured boot force for a neutral impact.

Despite the fact that the boot was able to reproduce the shape of the impulse, the magnitude of force recorded by the boot was approximately 10 times less than that measured in the ATD leg. This factor of difference is an average of 10.32 (0.93) across all of the dynamic tests (Table 3.7).

Table 3.7- The factor of difference between the peak force recorded by the boot and the peak F_{zLower} load cell channel.

Posture	*F_{zLower}/Total Boot Force*	*Std Dev*
15° Plantarflexion	11.21	0.09
15° Dorsiflexion	11.15	0.30
20° Inversion	9.82	0.48
5° Inversion	10.25	0.25
5° Eversion	9.07	0.10
Neutral (Start)	9.29	0.21
Neutral (End)	10.99	0.82
Average=	10.32	0.93

The percent of the total force that each of the sensors bore at the time of peak force was calculated and an average over impacts in neutral posture was calculated (Table 3.8).

Table 3.8- The average percent of the total load that each sensor recorded at the peak total boot force during neutral posture impact testing.

Sensor	*Average % Load*	*Std Dev*
1	53.9	6.0
2	19.9	6.1
3	3.6	2.8
4	13.1	4.7
5	0.7	0.3
6	5.8	3.4
7	3.0	0.8
8	0.1	0.0

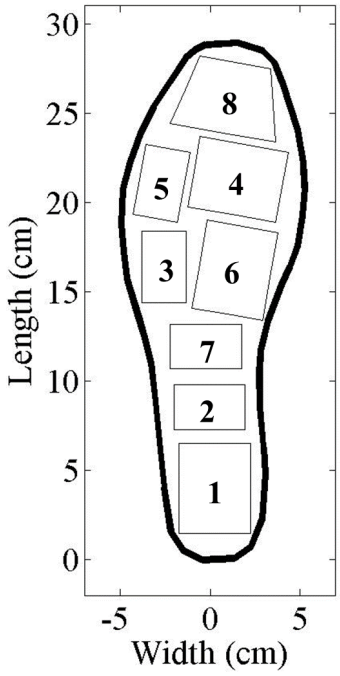

The posture of the ankle was found to affect the distribution of force over the sole of the foot. For example, the percent of the total peak force that is carried by sensor four across the range of postures tested in plantarflexion and dorsiflexion is shown in Figure 3-18.

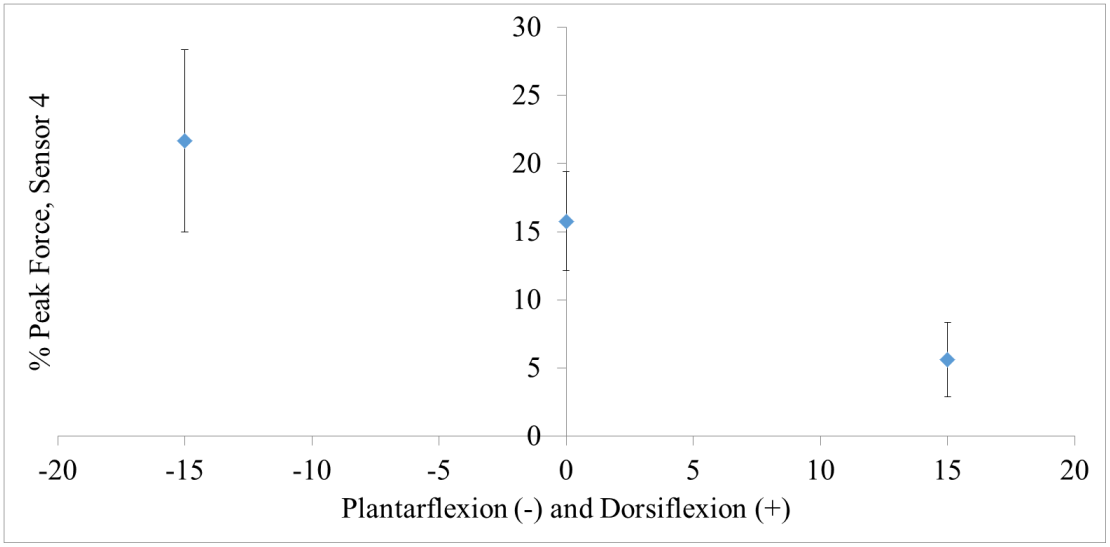

Figure 3-18- The percent of peak force that sensor four carried across tested postures in plantar/dorsiflexion.

The trends seen in the total boot force and the ATD leg peak force show good agreement when plotted in relation to dorsiflexion/plantarflexion (Figure 3-19) and inversion/eversion (Figure 3-20). However, there is consistently an order of magnitude difference between the two.

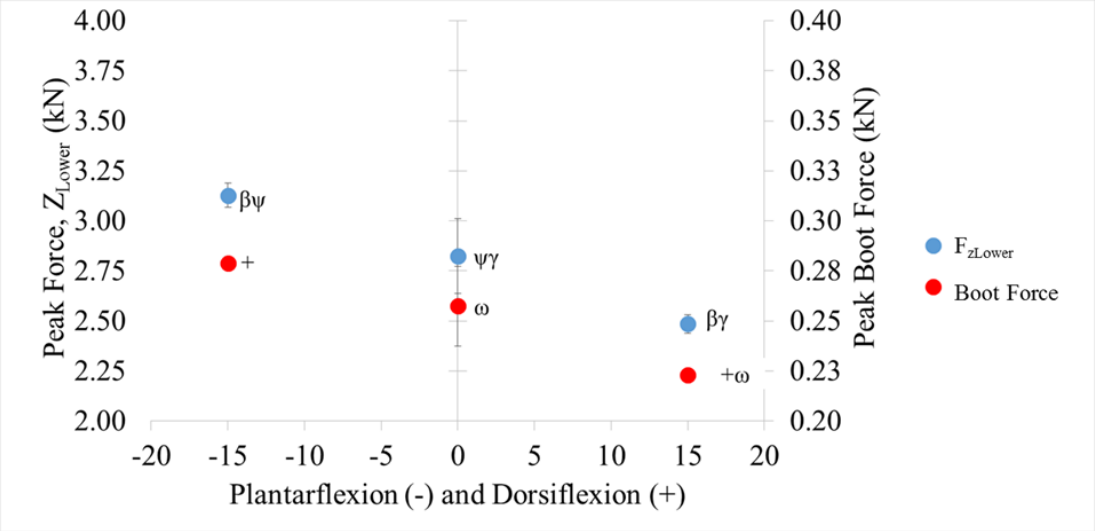

Figure 3-19- The peak F_{zLower} and boot force in dorsi/plantarflexion. Symbols denote significant differences ($p<0.05$).

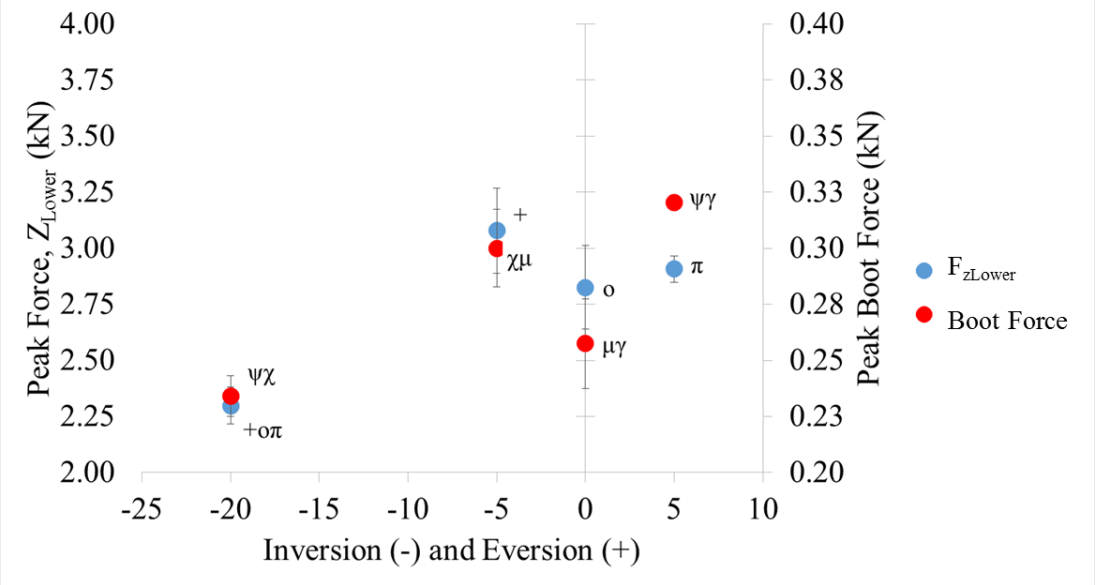

Figure 3-20- The peak F_{zLower} and boot force in inversion/eversion. Symbols denote significant differences ($p<0.05$).

3.4 Discussion

Sensors were developed and tested, in both quasi-static and dynamic loading, on their own and as part of an instrumented boot. This is the first known device developed for the purposes of evaluating loading to the foot under impact conditions.

3.4.1 Sensor Quasi-Static Calibration

The calibration curves for the sensors were created using repeated tests over a wide range of load. The output of the sensors was highly consistent, and the instrumentation system developed was reliable and effective. The smaller area sensors had the most consistent calibration curves, both when comparing among sensors of the same size and when comparing repeated tests on one sensor. This may be due to the fact that the larger plates did not distribute the applied force as evenly, bending slightly and creating variable pressure across the sensors. This hypothesis is supported by the observation that off center loading, on the edges or corner of the plate, affected the resistance response. In future iterations of this design, smaller plate geometry could be used to lessen the likelihood of plate deformation.

The capacity of the load cell on the material testing machine limited the range of force that could be used for calibration. A larger capacity load cell would allow for a more representative range of forces to be tested, and would also give an indication of the accuracy of the equation used to fit the curves at high pressures (at pressures above

approximately 50 kPa, large changes in pressure corresponded to small changes in resistance).

The DAQ used in this work had an absolute accuracy of 690 μV for the anticipated voltage range of 1 V, corresponding to less than 0.1% error (National Instruments 2010). The voltage generator DC output was rated at an accuracy of ±1% of the selected voltage range (Vishay Precision Group 2011). The reference resistor accuracy was also ±1% of its value, as determined by the banding. Taking the partial derivative of Eq. 3.1 with respect to each of the parameters allowed for an assessment of the contribution of each of these errors, leading to an expected overall error in R_2, at the resistances measured during the impact testing, between 1 and 2% of the calculated value.

At high pressures, this uncertainty in resistance could affect the estimated pressure. It may be necessary to adopt alternate instrumentation, such as a Wheatstone bridge, to measure these very small changes in resistance. This would create a limit on the lower limit of force sensing, but may make these sensors more useful at the high force levels expected in impact testing. Currently, the equation used to fit the calibration curve has been extrapolated beyond the capacity of the material tester load cell to make higher pressure estimations, and therefore may be a source of error for the sensor readings.

Temperature may also play an important role in the calibration of these sensors. The resistance of piezoresistive materials is known to be dependent on temperature (Vega et al. 2011). The temperature effect was not examined in this work, as temperature at the locations in which the calibration and testing occurred was similar. However, joule

heating of the sensors in the insulated boot may have shifted the temperature. The sensitivity of these sensors to temperature would be an interesting and useful investigation in the future.

The calibration of the sensors has a large effect on the ultimate accuracy of the sensors. If the sensor is not calibrated correctly, all measurements made with that sensor will be incorrect. More repetitions during calibration for each sensor, investigations into the effect of temperature, and testing and fitting over a larger force range will increase the accuracy of the calibration and of the sensor.

The resistance of the polymer appeared to be dependent on where the piece was cut from the roll. This indicates that the distribution of carbon black in the polymer is not homogenous. Samples cut at the same point along the width of the roll of polymer sheet and closely spaced along the direction of rolling were most consistent, so this strategy was adopted when cutting sensor material for this work. This emphasizes the importance of calibrating each individual sensor, which was done for all sensors used in the present work, leading to individual calibration curves and greater confidence in the output from the devices.

3.4.2 Dynamic Testing of the Sensor

The sensors were robust, easy to manufacture, and reliable. These sensors could be useful in many applications, especially where thin and light sensors are required. Although the sensors were able to correctly record force magnitudes in quasi-static

loading, in dynamic loading the force recorded in the load cell and in the piezoresistive sensor were different by a factor of between 5 and 10. This factor of difference did not seem to scale with either force amplitude or impact duration. It is likely that the viscoelastic nature of the polymer causes it to react differently depending on the applied strain rate, meaning that the response is a function of both amplitude and duration. Some of the discrepancy between the forces measured in the boot and in the ATD may be due to the complex translational and rotational acceleration of the segments of the leg.

Calibrating the sensor in different strain rate regimes may provide a solution to this scaling issue. The dynamic calibration performed in this work was unable to reliably vary the strain rates due to limitations with the apparatus. The consistency of the factor of difference between the sensor and load cells seems to indicate that applying the quasi-static loading calibration to the dynamic situation was inappropriate. It may be possible to calibrate the sensor at different rates, which would allow for the determination of the absolute magnitude of a force.

Without further testing and characterization of the sensor, it is difficult to use the piezoresistive sensors to establish the absolute amplitude of the force. However, if another load cell along the load path can be assumed to be subject to the same force, the forces recorded by the piezoresistive sensor can be scaled to the true value, giving useful information regarding the distribution and rate of application of forces. In most testing situations, it is possible to implement multiple load measurement systems for comparison,

which would make the use of these sensors possible for the measurement of dynamic loads as well as quasi-static loads.

3.4.3 Quasi-Static Testing of the Boot

In quasi-static loading, the boot accurately recorded the magnitude and location of forces. The fraction of the total force measured by each sensor was remarkably consistent over the course of each test and among tests. The discrepancies between the recorded load in the boot and in the material testing machine are likely due to inaccuracies in the sensors and development of alternate loading paths. The sensor was demonstrated to have a different response depending on the position of the sensor within the boot, influencing the overall accuracy of the boot.

The sensor and material tester curves diverged suddenly at one point in several of the tests, suggesting that an alternate loading path had been developed. These alternate load paths could have travelled through the foam insole after it distorted around the sensors and directly impacted the insole and sides of the boot, or they could have passed from the boot to leg through friction with the leg. The former explanation is supported by permanent deformation in the shape of the sensors on the insole (Figure 3-21). This divergence was only observed in some of the curves, and did not seem to be related to the order in which the sensors were tested. Thicker sensors to separate the insole and the sole, or better sensor coverage of the sole, might reduce the likelihood of alternate load paths forming.

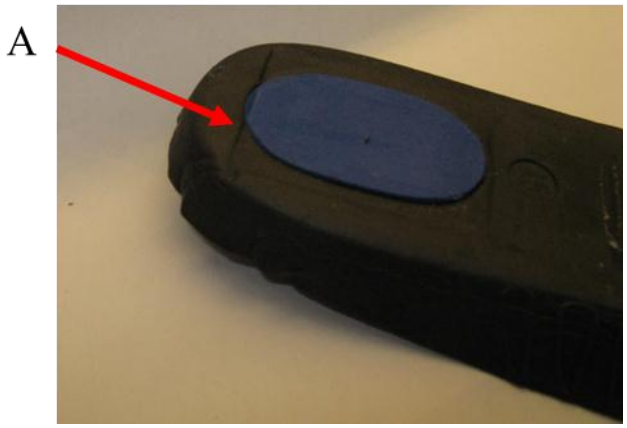

Figure 3-21- Permanent deformation (A) on the underside of the insole after testing.

The slope of the force-position curve increased over the course of testing. When the leg was remove from the boot and reinserted, the slope of the line decreased to a value slightly higher than the first test. This indicates that the boot load path became stiffer during the course of testing, likely due to compression of materials in the boot. The stiffening of the boot over multiple tests, and the partial reversal of this stiffening after the ATD was removed and reinserted, also indicates settling of the foot. For these reasons, it is important to perform multiple trials with the boot to allow it to "wear in". Ensuring that the foot is either well settled in the boot before recording impacts or removing and reinserting the foot into the boot prior to each impact will also reduce variability among tests.

3.4.4 Dynamic Testing of the Boot

The spatial distribution of load recorded by the sensors during the peak force was similar to that found during quasi-static testing. The heel was found to bear the majority of the force over the duration of the impact, as well as the highest peak forces, because it lies directly under the ankle joint. The ATD does not mimic muscle loading in the ankle, so forces acting on the forefoot or toes cause the ankle joint to rotate with minimal resistance. During the impact, the forces recorded in these areas would be those required to overcome the friction in the ball joint, the stiffness of the boot in flexion, and the inertial forces created when the foot is accelerating. This light loading in the forefoot, followed by heavy loading on the heel, can be seen in Figure 3-16. Higher forces would be expected in areas other than the heel if the ATD foot reached the limit of its range of motion, preventing the ankle joint from rotating, or if muscle loading were simulated.

The posture of the foot did affect the distribution of load, as demonstrated in Figure 3-18. Measuring the force distribution on the foot of a cadaveric specimen in multiple postures and correlating recorded injuries in that specimen with the distribution of force in ATDs in the same postures would be a useful preliminary step in developing foot injury criteria.

When the ATD was dressed with the boot, the shape of both the upper and lower F_z curves was altered. A peak early in the impact appeared when compared to the impacts without the boot. This peak correlated to a negative dip in the output of the boot sensors, which is indicative of unloading.

These two facts taken together suggest that early in the impact the load path through the boot was not through the sole, where the sensors were, but in fact was through the edges of the sole. This force is transferred to the foot and leg through frictional forces with the boot, unloading the sensors under the foot. This created the early sharp peaks in the F_z force curves and the negative dip that indicates unloading in the sensors. Later in the impact, the forces appeared to follow the more intuitive load path through the sole of the foot. Post impact, the force fell to a negative, constant value, which seems to correlate to the pre-impact minimum, indicating that after impact the boot is not resting as heavily on the sensors. This may be caused by subtle stretching of the laces or boot during impact.

The load path around the sensors, which is thought to have occurred at the beginning of the impact, is likely caused by higher stiffness due to stitching and reinforcement where the leather of the upper of the boot is attached to the sole. This observation demonstrates the large effect that seemingly minor differences in stiffness can have under high rates of loading.

The boot sensor recorded a much smoother curve than the ATD load cell. This is attributed to the fact that there is more free mass, which creates forces due to vibration and acceleration, distal to the ATD load cell than the boot sensors.

If the foot is entrapped between two parts of a vehicle during crash testing, very high forces could be expected which can create severe injuries (Morris et al. 1997). Current techniques would likely not record this injury, while this new tool would be able to record these forces and therefore identify the associated risk of debilitating injury.

3.4.5 Future Directions

These sensors are inexpensive and effective, but there are ways in which they could be improved and refined. The piezoresistive material used for these experiments is not specifically designed for this use. Work to produce a more consistent polymer with properties tailored to produce the largest resistance changes in the ranges of pressures which are being investigated would be beneficial. The type of polymer, the type and volume fraction of conductive particle, the length of polymer chains, and the homogeneity of the conductive particle distribution are just a few of the parameters that could be investigated.

It may be useful to have more sensors to better cover over the sole of the boot and provide more information regarding spatial distribution of force. This would help mitigate the possibility of alternate loading pathways being created (improving the ability of the boot to fully capture forces) and would also increase the spatial resolution. If the piezoresistive polymer were tailored to the pressure levels of interest, this would also allow each area of the foot to be covered with a sensor that was most sensitive to the expected pressure range for that region.

Pre-stressing the polymer using a more refined mounting system would allow for the sensor to measure both compression and tension, and would also eliminate some uncertainty in lower pressure regions by reducing the likelihood of the polymer moving away from the electrode. With the current design, there is no compressive force across

the sensor when unloaded. A small amount of tension across the sensor can cause the plate and polymer to separate, producing an air gap with very high resistance. This could produce misleading readings because the relationship between pressure and resistance is only valid when the resistance is dependent on the piezoresistive material. If the contact resistance becomes significant, the relationship no longer holds. However, in impact testing there are relatively minimal tensile forces, so this is not a major concern at the present time.

Although the dynamic calibration of the sensor addressed some loading rate effects, a series of tests on the sensor, and of the assembled boot, that covered a wide range of rates and peak forces would be beneficial in estimating the effect of strain rate. Other techniques to explore the time dependence of the sensor could also be employed, such as subjecting the sensors to periodic forces at variable frequencies.

3.5 References

Canadian Centre for Occupational Health and Safety. (2010). Safety Footwear. Retrieved May 12, 2014, from http://www.ccohs.ca/oshanswers/prevention/ppe/footwear.html

Hudson, D. (2014). The effect of walking with poles on the distribution of plantar pressures in normal subjects. *Physical Medicine and Rehabilitation*, *6*, 146–51.

Kalantari, M., Dargahi, J., Kövecses, J., Mardasi, M. G., & Nouri, S. (2012). A New Approach for Modeling Piezoresistive Force Sensors Based on Semiconductive Polymer Composites. IEEE/ASME Transactions on Mechatronics, 17(3), 572–581.

Levesque. (2013). Canadian Military – Land Operations Temperate Boot. Soldier Systems: An Industry Daily. Retrieved April 10, 2014, from http://soldiersystems.net/2013/10/15/canadian-military-land-operations-temperate-boot/

Mertz, H. (1994). Injury Assessment Values Used to Evaluate Hybrid III response Measurements. In S. H. Backaitis & H. J. Mertz (Eds.), Hybrid III: The First Human-Like Crash Test Dummy (PT-44th ed., p. 418). Warrendale: Society of Automotive Engineers.

Morris, A., Thomas, P., Taylor, A. M., & Wallace, W. A. (1997). Mechanisms of Fracture in Ankle and Hind-Foot Injuries to Front Seat Car occupants- An In-Depth Accident Data Analysis. Stapp Car Crash Conference, 41, 181–192.

National Instruments. (2010). C Series Analog Input Module NI 9205 Specifications. Retrieved January 23, 2014, from http://sine.ni.com/ds/app/doc/p/id/ds-190/lang/en

NATO/PfP. (2006). Procedures for Evaluating the Protection Level of Logistics and Light Armoured Vehicles, AEP- 55 (AEP- 55, V., Vol. Volume 2). Brussels, Belgium: North Atlantic Treaty Organization.

Razak, A. H. A., Zayegh, A., Begg, R. K., & Wahab, Y. (2012). Foot plantar pressure measurement system: a review. Sensors, 12, 9884–912.

Tekscan Inc. (2010). FlexiForce ® Sensors User Manual (Rev H). Retrieved from http://www.tekscan.com/pdf/FLX-FlexiForce-Sensors-Manual.pdf

Vecchi, F., Freschi, C., Micera, S., Sabatini, A. M., Dario, P., Sacchetti, R., & Superiore, S. (2000). Experimental Evaluation of Two Commercial Force Sensors for Applications in Biomechanics and Motor Control. In 5th Annual Conference of the International Functional Electrical Stimulation Society (pp. 4–7).

Vega, A., Sumfleth, J., Wittich, H., & Schulte, K. (2011). Time and temperature dependent piezoresistance of carbon nanofiller/polymer composites under dynamic load. Journal of Materials Science, 47, 2648–2657.

Vishay Precision Group. (2011). Signal Conditioning Amplifier. 2300 System. Retrieved April 21, 2014, from http://www.vishaypg.com/docs/11255/syst2300.pdf

4 Numerical Modelling of the Sensor Response

4.1 Introduction

During an impact event the loading to the foot (and correspondingly any sensors in an instrumented boot) tends to be normal in direction. The structure of the boot helps prevent shear forces from being transmitted through the sensors by physically constraining the foot in the boot. However, there is a chance of shear loading on the sensors; therefore, it is important to determine if shear forces affect the resistance across the piezoresistive polymer as normal forces do. The response of piezoresistive polymers to shear forces has not been previously investigated. If shear forces do create substantial changes in the resistance of the polymer, it would be necessary to develop practices to separate the measurement of shear and normal effects, or avoid the possibility of shear stresses acting on the sensor.

The sensors were successfully tested under compressive loading (see section 3.3.1), but attempts to test the sensors under shear stress were unsuccessful. The sensors developed in the previous chapter were assembled using electrical tape to maintain the structure while minimizing the possibility of alternative load paths forming. This assembly did not allow the polymer to be stressed in shear, so conductive adhesive was used to fix a piece of piezoresistive polymer between two platens which could then be pulled apart using a material tester while the resistance across the polymer was measured. This would have

mimicked a lap shear test. Unfortunately the conductive adhesive was much less conductive than expected and this experiment had to be abandoned.

Instead, a numerical simulation was adopted. Several researchers have developed relationships between resistance and normal stress in a piezoresistive polymer (Kalantari et al. 2012; Wang et al. 2013; Zhang et al. 2001). These works estimated the change in resistance by developing a relationship between particle separation and resistance, and then using the mechanical properties of the material to estimate the average change in particle separation with stress. This requires the assumption that particle size and distribution is homogenous, and also that the paths of current flowing between the particles are evenly distributed. In order to create a simulation that can be used to explore both of these assumptions, a Monte Carlo type simulation was developed in this work. In this type of simulation, many trials of the same type, with some random input, are repeated and the results are collected to obtain a distribution of results. This can be used to determine which result, or range of results, is statistically most likely to occur.

The first goal of the present simulation work was to explore whether or not shear strain would influence resistance, and to provide basic answers to questions regarding piezoresistive polymers. A numerical model which allows for a high degree of freedom in the range of inputs for various material properties was desired.

This simulation would also provide a foundation for more complex models which can be used to investigate the influence of material properties, such as conductive polymer size

and volume fraction, which would be beneficial when manufacturing polymers for this application.

4.2 Methods

The model was developed in MATLAB® (The MathWorks Inc, Natick, MA, USA). The resistance of a simulated volume of material was calculated (Appendix M). The material used in Chapters 3 was composed of conductive particles of carbon black dispersed in a polyethylene matrix. In order to simulate this, perfectly conductive, spherical particles with uniform diameter were randomly distributed in a volume, which represents the non-conductive polyethylene matrix of the polymer. This random distribution was accomplished by generating an x, y, and z Cartesian coordinate using a uniform random number generator. If a particle were placed such that the center to center distance was less than the particle diameter, that particle was placed again, in order to prevent particle volumes from overlapping. The number of particles in the volume was determined by the total volume fraction of conductive material modeled, as well as the density of particles in the material. A 500 nm diameter spherical particle and 0.3 volume fraction (carbon volume/polyethylene volume) was used in the simulation. These figures are based on measurements made by Kalantari et al. (2012), who used the same type of material as was used in Chapter 3.

The Dijkstra algorithm was implemented to find the minimum resistance path from the anode to cathode, across a simulated volume of the polymer. The implementation of the

Dijkstra algorithm used in this work was heavily modified from an open source program (Kirk 2008). This algorithm is extremely memory intensive. In the algorithm, the "cost" of each path, in this case the resistance, between every two points is determined. Various strategies, such as limiting the maximum distance that the algorithm will look to find the next particle that might reasonably be the lowest cost, were implemented in this work. Although these strategies significantly reduced the computational intensity, only a small number of particles (approximately 600) could be simulated with reasonable run times on the computer that was available.

To simulate the anode and cathode on each side of the material sample, points were created on the top and bottom surfaces of the simulated volume, which were aligned with particles within the top and bottom three particle diameters of the surface. Distances between particles greater than three diameters were considered to be unlikely to be a part of the shortest path; this assumption was examined by increasing the distance considered in order to determine if this distance affect the results of the simulation. The resistance between each particle and any neighbor within three diameters was then calculated based on the equations described below.

Resistance from one particle to the next was determined based on the theory of tunneling developed by Simmons (1963) to describe the current density flowing through a material:

$$J = \frac{3\sqrt{2m\varphi}}{2s}\left(\frac{e}{h}\right)^2 V e^{-\frac{4\pi s}{h}\sqrt{2m\varphi}} \qquad \text{Eq. 4.1}$$

Where:

$$s = surface\ to\ surface\ distance\ (m)$$

$$h = 6.62x10^{-34}\frac{m^2 kg}{s}, \qquad Planck's\ constant$$

$$m = 9.109x10^{-31}kg, \qquad electron\ mass$$

$$e = 1.602x10^{-19}C, \qquad electron\ charge$$

$$\varphi = 8.01x10^{-21}\ J, \qquad energy\ barrier\ between\ carbon\ and\ polyethylene$$

The energy barrier to transfer an electron between carbon and polyethylene was estimated by Zhang et al. (2001). Substituting this formula into Ohm's Law, resistance between neighboring particles was found:

$$R = \frac{V}{I} = \frac{V}{Ja} = \frac{8\pi h}{3a\gamma e^2}\ s\ e^{\gamma s} \qquad \text{Eq. 4.2}$$

Where:

$$\gamma = \frac{4\pi}{h}\sqrt{2m\varphi} \qquad \text{Eq. 4.3}$$

$$a = cross\ secitional\ area\ of\ particle\ (m^2)$$

The resistance contributed by each particle along a single path was combined in the same fashion as resistors in series (Equation 4.4):

$$R1_{Series} = R_1 + R_2 + \cdots R_N \qquad \text{Eq. 4.4}$$

The path with the lowest resistance from each of the particles within three diameters of the anode was combined in the same fashion as resistors in parallel to determine the total resistance across the simulated volume (Equation 4.5):

$$\frac{1}{R_{Total}} = \frac{1}{R1_{Series}} + \frac{1}{R2_{Series}} + \cdots \frac{1}{RN_{Series}} \qquad \text{Eq. 4.5}$$

The number of paths and the number of particles involved in each path changed with each iteration, depending on the location of the randomly distributed particles. Strain in the material caused by a simulated normal stress, increasing from 0 to 300 kPa in 20 steps, was calculated. In order to determine the strain based on the applied force, the compressive modulus of the material was estimated to be 0.7 GPa (MatWeb 2014). Shear angle, from 0 to 0.9 degrees in 6 steps, was used to simulate strain due to shear force. Shear angle, rather than shear strain, was used because the magnitude of shear stress that might be experienced by the sensor is unknown, and the shear angle allowed for a simpler calculation of particle location, while still fulfilling the goals of the simulation. The position of each particle was adjusted based on the strain and the original position.

When simulating shear, particles that were pushed outside of the simulated volume re-entered on the opposite side of the volume in order to maintain the same average

electrode to electrode distance; otherwise, by the end of the simulation the distance would be the hypotenuse of a triangle with the shear angle being one vertex. In a larger simulated volume this effect would be negligible, but due to the small simulated volume, this change in average distance would have had an effect on the results.

The small simulation volume may have also created edge effects, which would be negligible in a much larger simulated volume. In order to mitigate this potential issue, the simulated volume was extended three particle distances past each edge of the simulated electrodes so that minimum paths could leave and re-enter the footprint of the electrode, as they could if the simulated volume were part of a much larger volume.

The total resistance was very different depending on the random assignment of particles. This, again, would not have been an issue in a larger simulation volume. In order to normalize the results, the ratio of current resistance to initial resistance was calculated at each level of applied strain. Two thousand simulations were averaged to model shear, and one hundred simulations were averaged to model normal force. The number of iterations necessary was determined by running the simulation while periodically checking if the values appeared to have converged. Once convergence occurred, the simulation was stopped. The particles were randomly distributed for each trial, but the simulated volume was the same, at (10 particle diameters)^3, or 1.25 x 10^{-16} m^3.

4.3 Results

4.3.1 Normal Force

Figure 4-1 illustrates how the resistance path changed as the normal force was applied. Each particle is represented by a sphere, and the red and green sheets represent the electrode. Each particle involved in the minimum resistance path from each anode to cathode is shown in purple. Particles that are involved in more than one path are a darker shade of purple. The light blue lines represent the minimum paths from each particle at the anode to any particle at the cathode. When the simulated force on the volume was increased, the path distance (and consequently resistance) decreased. This simulation considered only the single lowest resistance path for each point on the anode; there would be many other paths for current to flow across the volume.

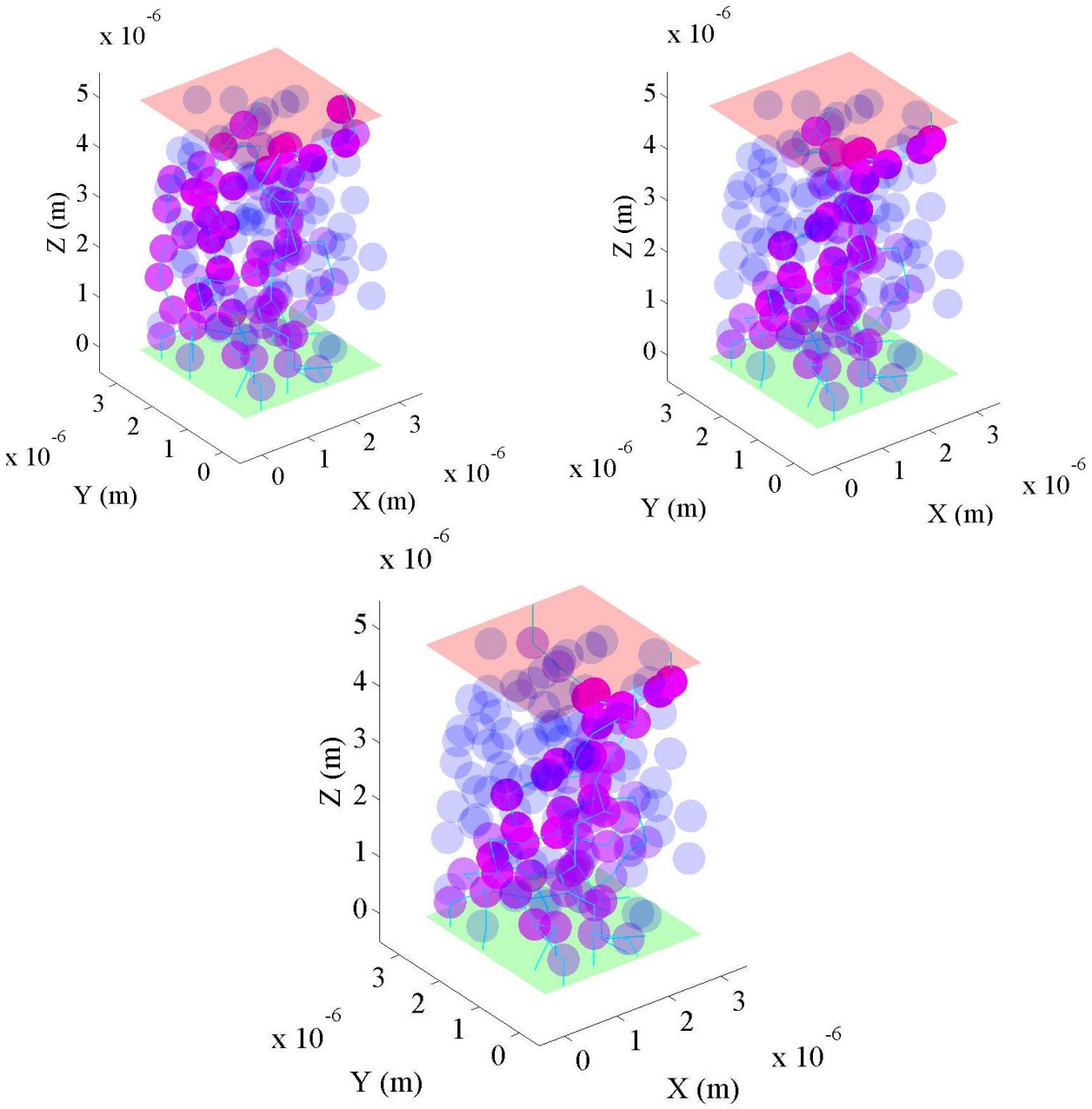

Figure 4-1- Simulated current through a volume of conductive, uniform, spherical particles (a volume approximately 1/5 of that which was used in the simulation is shown in this figure for clarity).

The averaged resistances of 100 simulated volumes under increasing levels of normal force are displayed, with the standard deviation of the set displayed as error bars (Figure 4-2). The 'experimental' curve was constructed using the average calibration curve for sensor one (refer to Section 3.2.3). This curve was offset so that the ratio of resistance (R) to initial resistance (R_0) was unity when force equaled 0 N.

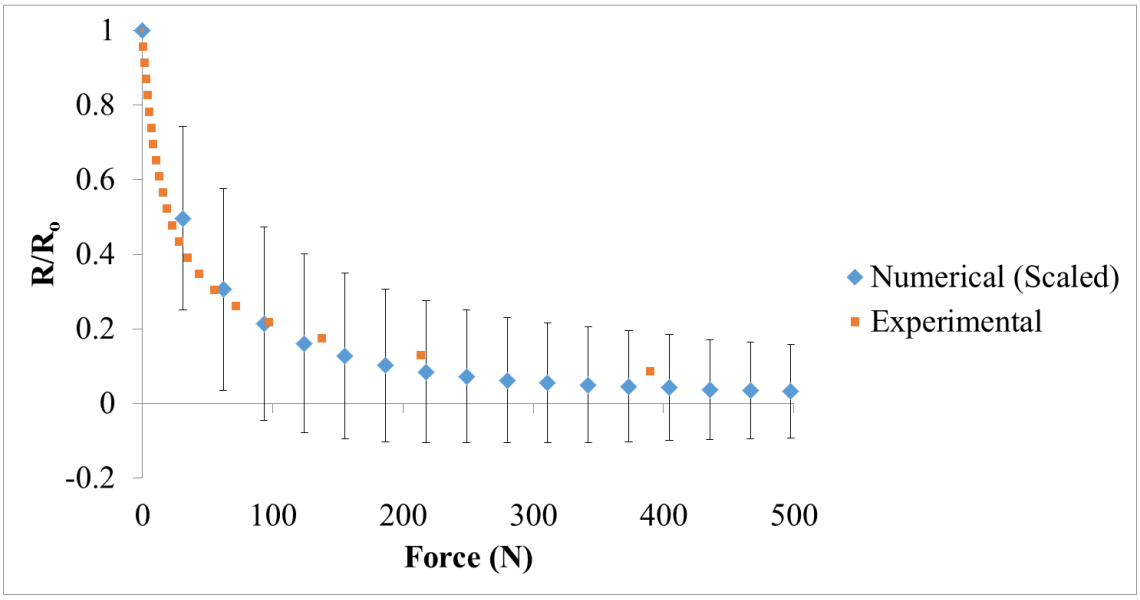

Figure 4-2- The relationship between change in resistance and applied force. Experimental and scaled numerical simulation results are plotted.

The plot shows the average change in resistance, expressed as a fraction of initial resistance, as normal force was applied. The force was scaled by a constant factor of 1/30000 so the numerical results could be compared on the same plot as experimental

results. This scaling was necessary because the numerical model is based on estimated physical parameters (*i.e.* particle size, distribution, volume fraction of particles, compression modulus) of the piezoresistive polymer and an extremely small simulation volume; if the relevant physical parameters for this particular material were determined experimentally and the larger size volume could be modelled (which was not done due to computational limitations), this scaling could likely be eliminated. The convergence of the simulation is demonstrated in Figure 4-3

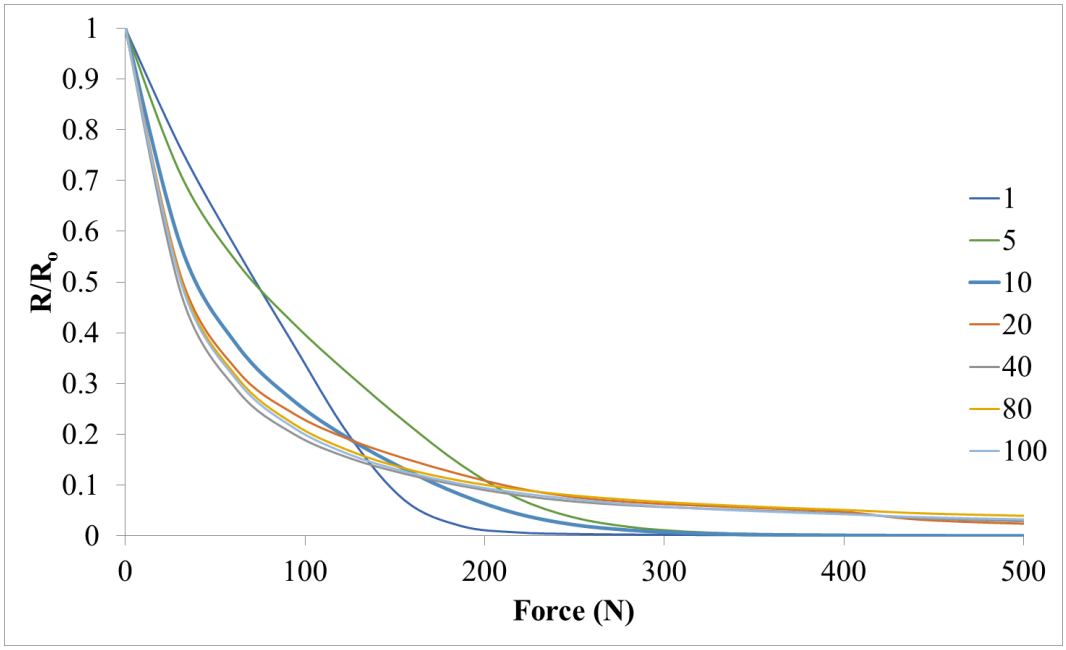

Figure 4-3- The average ratio of resistance to initial resistance as more simulations (number shown in legend) were added. Convergence occurred at approximately 100 simulations. These results are scaled by the same factor as above.

4.3.2 Shear Strain

Under shear loading, small shear strains in the model produced very large changes in resistance. A small change in location of a given particle tended to create an entirely new path for the current to flow. In a larger simulated volume many paths would be involved so the average resistance value would be more consistent. In order to account for this issue, the ratio of current resistance to initial resistance at each level of simulated shear strain was averaged across 2000 trials (Figure 4-4)Figure 4-4- A semi-log plot showing the average ratio of resistance to initial resistance as more simulations (number shown in legend) were added. Convergence occurred at approximately 1500 simulations..

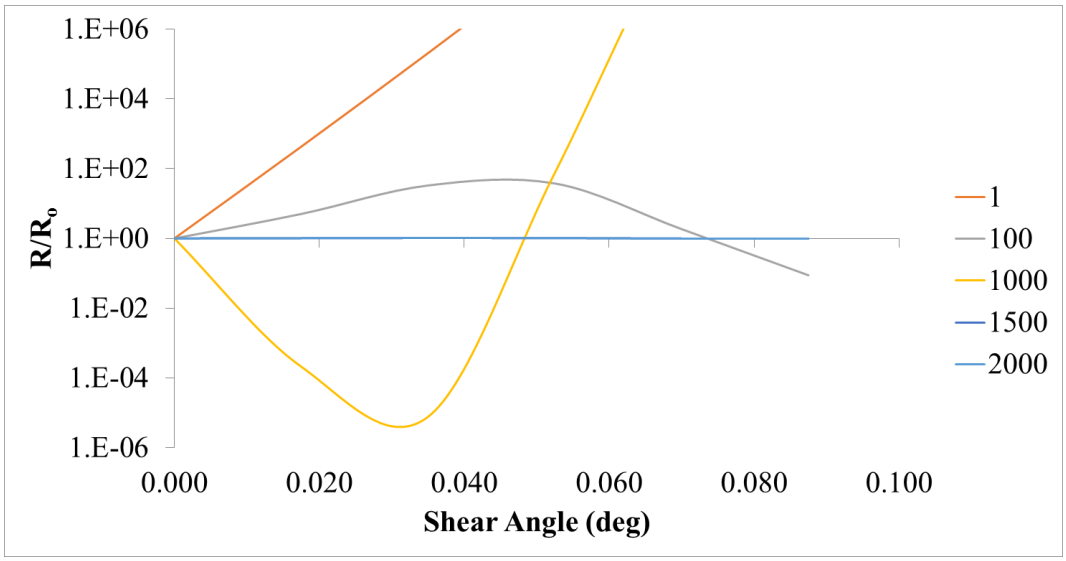

Figure 4-4- A semi-log plot showing the average ratio of resistance to initial resistance as more simulations (number shown in legend) were added. Convergence occurred at approximately 1500 simulations.

Figure 4-5 shows the total average ratio of resistance as the shear angle of the sample was increased. As shear strain could not be experimentally tested, no comparison is shown.

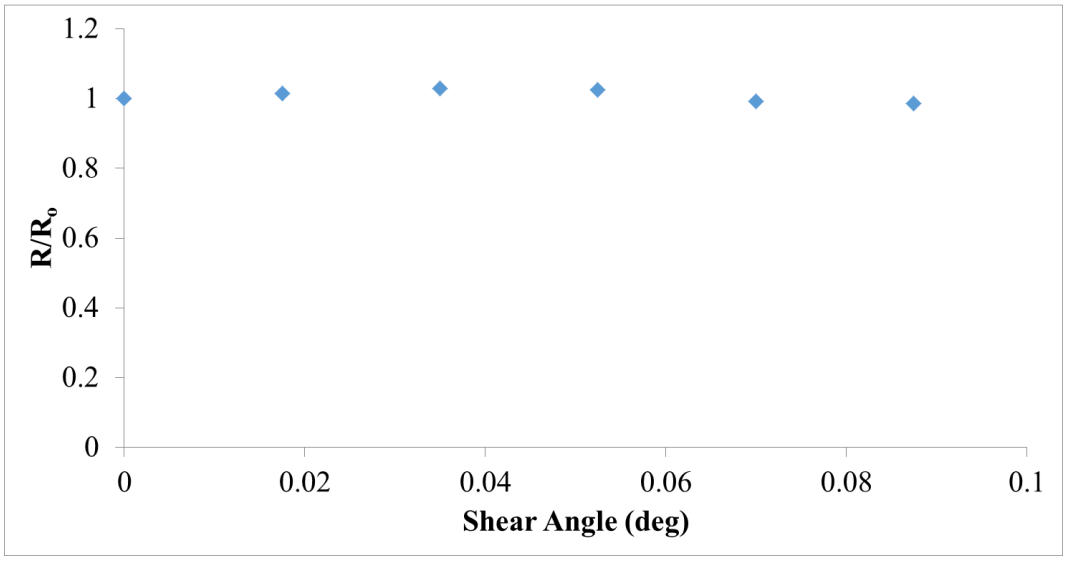

Figure 4-5- The ratio of resistance to initial resistance was near unity across shear angles.

4.4 Discussion

This model simulated resistance change due to normal strain and shear strain. When modeling the response to normal stress, the scaled resistance-stress curve matched the shape of the experimental results closely. The simulation was also used to explore the effect of shear strain on the measured resistance of the material. The results showed that shear strain likely does not affect the resistance of the material, which is a useful finding when determining how sensors made from piezoresistive material may be used in practical applications. As long as the sensor is not physically destroyed in shear,

measurements of normal force will likely be unaffected by any applied shear stress. This result should be experimentally validated in the future to ensure the accuracy of the model.

The model was able to predict whether the resistance would increase or decrease. Without detailed measurement of material properties, such as the volume content of conductive particle, distribution of properties, and diameter and shape of particles, it would not be possible to determine the true resistance value of the material. Furthermore, due to the large number of particles involved and the associated computing cost of the Dijkstra algorithm, a simulation of any large volume of material would be incredibly memory intensive. These reasons likely explain why the magnitudes of the experimental and simulation results were so different, although the shapes of the curves were very similar.

The Dijkstra algorithm was implemented to find the paths that had the lowest associated resistance and, in this application, would therefore be the most important. There are countless other paths that the current could take through the particles to get from one electrode to the other. This algorithm effectively sorts them and finds the set with the lowest cost. The number of paths it considers is equal to the number of particles within three diameters of the anode. For each of those particles, a path to the cathode was found.

Several concessions were made in order to allow modelling while maintaining reasonable computing times. First, as described earlier, only particles within certain distances were considered. It was assumed that the very high resistance encountered for the current to

reach particles outside this distance would make these paths unlikely to be part of the minimum path.

Secondly, only a small material volume could be simulated. This required the results to be scalable in order to model the full sized sensor. The Poisson effect was also not considered. This was done to make the simulations more efficient; calculating the displacement due to the Poisson effect for every particle depending on their position in the volume of interest would have been extremely memory intensive. Modeling this effect in future iterations of the simulation could be performed to verify that this assumption is valid.

Even with these efforts, evaluation of the resistance of a simulated volume in a given state of stress took about one minute. Although this seems low, with many iteration and multiple stress states to be considered for each simulated volume, the program took two weeks to run when modelling shear strain.

It was critical to repeat the simulation enough times for the results to converge. The simulation was repeated using different particle positions until the average of those results converged on a stable number. The modelled response of the sensor to shear strain was extremely sensitive to the size of the sensor. As the material deformed in shear, the particles that were involved in the minimum resistance path changed (one would be pushed slightly further than another), leading to massive variations in the resistance. This resulted in the need for many repetitions to achieve convergence of the simulation. The modeled response of the sensor to normal forces was much less variable. This is likely

because the particles involved in the minimum paths did not change greatly; instead, the paths were simply shortened as the material was compressed.

This simulation utilizes the concept that the resistance between particles is dependent on their distance from one other. Each of these resistances was added, either in series or parallel as required, to create a path from one electrode to the other. By implementing the Dijkstra algorithm, the most important paths (in terms of resistance) for a set of particles were determined, making the computation more efficient. Adding these paths together gives a representative value for the resistance of the volume, which can then be compared to other values of resistance when the volume is subject to various types of strain.

This simulation allowed for exploration of the effects of normal and shear forces on the resistance of the piezoresistive polymer, and could also be used in the future to investigate the effect of various material properties on the resistance of the polymer.

4.5 References

Kalantari, M., Dargahi, J., Kövecses, J., Mardasi, M. G., & Nouri, S. (2012). A New Approach for Modeling Piezoresistive Force Sensors Based on Semiconductive Polymer Composites. IEEE/ASME Transactions on Mechatronics, 17(3), 572–581.

Kirk, J. (2008). Advanced Dijkstra's Minimum Path Algorithm. MATLAB file Exchange. Retrieved from http://www.mathworks.com/matlabcentral/fileexchange/20025-advanced-dijkstra-s-minimum-path-algorithm

MatWeb. (n.d.). Compressive Strength Testing of Plastics. Retrieved April 21, 2014, from http://www.matweb.com/reference/compressivestrength.aspx

Simmons, J. G. (1963). Generalized Formula for the Electric Tunnel Effect between Similar Electrodes Separated by a Thin Insulating Film. Journal of Applied Physics, 34, 1793–803.

Wang, L., Han, Y., Wu, C., & Huang, Y. (2013). A solution to reduce the time dependence of the output resistance of a viscoelastic and piezoresistive element. Smart Materials and Structures, 22, 075021.

Zhang, X. W., Pan, Y., Zheng, Q., & Yi, X. S. (2001). Piezoresistance of conductor filled insulator composites. Polymer International, 50, 229–236.

5 Discussion

5.1 Initial Ankle Posture in ATD Testing

Anthropomorphic Test Devices (ATDs) are one of the most important tools in safety testing. They are used extensively to assess the ability of vehicles to protect occupants during crashes or other potentially injurious impacts. Despite the fact that the lower leg and foot are often injured during these events, the Hybrid III leg does not directly record data from the foot or ankle. Instead, criteria for injury risk to the foot, ankle, and lower leg are generally grouped and based on data recorded from the load cells in the tibial shaft of the ATD. These criteria were developed with specimens being axially impacted in a neutral posture (*e.g.*, Kuppa, Wang, et al. 2001). Any influence on this recorded data by posture would therefore lead to variability in the assessment of injury risk when using Hybrid III ATDs in testing. Whether the influence of posture on injury risk is reflected in reality for humans has yet to be determined.

The Hybrid III leg does not attempt to simulate the natural articulations of the human ankle or the natural stiffness of the leg; both of these have been identified as factors which limit the prediction of injury to the lower leg with this device (McKay 2010). Furthermore, the fact that the Hybrid III does not record posture makes it difficult to correct for, or investigate, these issues after testing. The Thor-Lx and MiL-Lx have both been developed as advanced ATD legs to address some of these issues. However,

because the Hybrid III remains the most widely used and accessible leg, it was chosen for this study.

It was found that the initial posture of the Hybrid III ankle did have significant effects on both TI_{Adj} and F_z, which are two main criteria used to evaluate lower limb injury in industry. The range of outcomes produced under very similar impact conditions, with only the posture changing, would have resulted in different injury risk assessments in both automotive crash testing and military testing. Without similar impacts being conducted on cadaveric specimens, it is not possible to determine if the behavior of the Hybrid III ankle is biofidelic. However, if these tests were to be performed in the future, the data collected using the cadaveric specimens could be compared to the data collected herein using the Hybrid III, and injuries in the cadaveric specimens could be related to measured values in the ATD.

Performing multiple repetitions of a controlled impact allowed for some subtle but interesting behaviors in the Hybrid III leg to be observed. It appears that eccentric loading of the lower load cell due to the design of the joint may have led to an "artificial" moment being recorded. This effect should be investigated in the future, and if the load cell used in the Hybrid III is found to be sensitive to eccentric loading, the design of the joint could be changed to mitigate this issue. Also, the stiffness of the ATD in non-axial combined loading was hypothesized to have affected the measured forces in the leg, and could be investigated further. Both the MiL-Lx and Thor-Lx incorporate compliant elements to better match the axial stiffness of a human lower leg, but the bending stiffness

may also be important, especially when testing in non-neutral postures. The bending stiffness of these new surrogates should be evaluated in the future.

In order to make comparison to other impact studies more reliable**,** it would be beneficial to conduct impacts at multiple energies. Only one level of impact energy was considered in this work to allow for straightforward comparison within the study, but this makes comparison to studies conducted at different impact velocities problematic, as the influence on velocity was not examined. However, the chosen impact velocity of 5 m/s produced peak forces and impact durations that are representative of real-world impact events. Also, TI and F_z values measured during the impact spanned critical values for injury prediction.

5.2 Developing the Instrumented Boot

A device that can record forces in the foot and can be easily adapted to either cadaveric specimens or ATDs was developed. This instrumented boot utilized piezoresistive sensors, which were custom built for use in the boot. A simple construction, instrumentation, and calibration procedure made these sensors inexpensive and reliable.

In quasi-static loading of the Hybrid III leg in the instrumented boot, the boot was able to capture an average of 80 percent of the work recorded by the material testing device. This figure could be improved by calibrating the sensors across a larger range of forces, changing the shapes of the sensors to better cover the boot sole, and increasing the number of sensors to avoid the creation of alternate loading paths.

The effects of shear stress on the sensor were not investigated experimentally due to issues encountered when bonding the polymer with adhesive, but were investigated numerically. Further work to investigate the effect of bending on the resistance measured across the polymer would also be beneficial as this type of distortion could occur when the boot and plates flex during impact. The numerical simulation that was created simulated the resistance change of the polymer with an applied stress. Using this simulation, it was demonstrated that the sensor was insensitive to shear stress in its resistance response, and is therefore not a loading condition that must be avoided when using the sensors.

In dynamic testing, the sensors were able to record the shape of the force curve, and perhaps most importantly, the distribution of force. This allowed for visualization of the location of forces on the sole of the foot, and also provided information about the load pathways through the foot during impacts conducted with footwear.

Investigating the distribution of forces over the foot in real time could allow for comparison to cadaveric studies and correlation to foot injury in the future. However, the boot recorded a force that was consistently around one tenth of that recorded by the Hybrid III leg load cell. This is a significant limitation that requires further investigation to resolve, and prevents force magnitude measurements using the boot sensor exclusively at this point. A second, proven load cell must be used to measure force in the path to allow for the forces to be appropriately scaled.

It is likely that some of the discrepancy between the load measured in the boot and in the ATD can be attributed to losses related to the elastic nature of the materials in the testing apparatus, as well as rotational and translational acceleration of the leg and foot during the impact. Measurement of acceleration of these segments may allow for better understanding of this issue. This illustrates that the ability to measure force at various locations on the foot and leg could be especially important in the development of more refined injury criteria in the lower leg.

A thorough examination of the sensor under dynamic conditions may help to identify the factors that are responsible for the difference in recorded magnitudes. The strain rate and peak force were both suggested herein as factors that may influence the recorded force. If a correction factor could be developed, it would allow for direct measurement of force magnitude with the sensor. Investigation of the accelerations of the leg and foot during impact may help to describe the dynamics, and consequently forces, acting on the foot.

The adjusted boot sensor measurement and Hybrid III lower load cell (with and without the boot) followed a consistent trend in peak axial force over the range of postures tested (Figure 5-1).

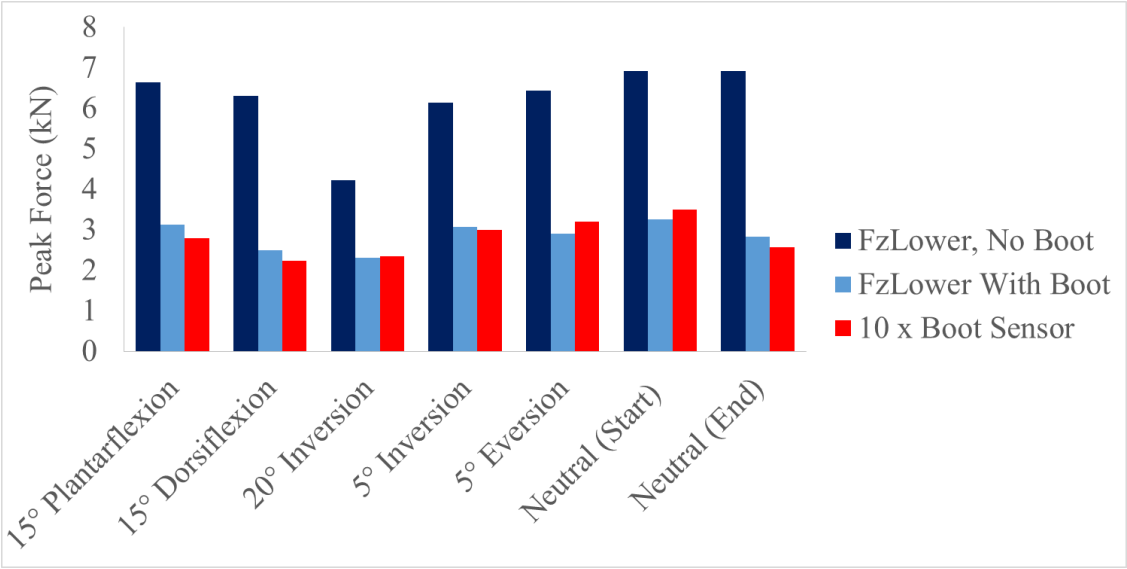

Figure 5-1- The peak force measured in F_{zLower} with and without the boot, and ten times the peak forces measured by the boot, at various postures.

Although the instrumented footwear in this work was developed using a boot, the sensors and instrumentation could be used to understand how other types of footwear can affect the load paths and force magnitudes measured during impact. The reduction in peak force with the addition of the chosen boot ranged from 45-61%, as seen in Table 5.1, which is similar to the reduction of 65% noted in the study by Quenneville and Dunning (2012), who investigated the force attenuation of hiking boots in blast impacts. This demonstrates the importance of considering the effect of footwear in impact testing.

Table 5.1- A summary of the reduction of peak F_{zLower} forces caused by the boot.

Posture	*Peak F_{zLower} (N)*		*% Reduction*
	With Boot	Without Boot	
15° Plantarflexion	3125	6634	53
15° Dorsiflexion	2487	6306	61
20° Inversion	2297	4227	46
5° Inversion	3075	6142	50
5° Eversion	2905	6430	56
Neutral (Start)	3247	6920	53
Neutral (End)	2823	6920	59
		Average=	54

5.3 Summary

The forces and moments measured in an Anthropomorphic Test Device leg were found to be affected by the initial posture of the ankle. Similar tests on cadaveric specimens are necessary to determine if this ATD can be used to predict the risk of lower leg injury to humans in non-neutral postures. In the meantime, the ATD should be set in a neutral posture prior to crash testing in order to match how commonly used injury criteria were developed.

The foot of the ATD is typically not instrumented, making it difficult to assess the risk of injuries to the foot, which can be extremely debilitating. Currently, only a general force magnitude across the whole foot can be estimated based on data recorded higher up the leg in the tibia. This requires assumptions to be made about the risk of injury to the various structures of the foot. The instrumented boot developed in this work is an inexpensive, simple tool to better understand force distributions in the foot, and it could be used to develop injury criteria specific to the foot.

Although there is still work to be done in understanding lower extremity injury, this tool could help to solve some of these issues. Hopefully, this will lead to safer vehicles and a better chance of an occupant walking away from a vehicle crash or impact without serious injury.

5.4 References

Kuppa, S., Wang, J., Haffner, M., & Eppinger, R. (2001). Lower Extremity Injuries and Associated Injury Criteria. In Proceedings of the 17th International Technical Conference on the Enhanced Safety of Vehicles (Vol. 4). Paper No. 456.

McKay, B. J. (2010). Development of Lower Extremity Injury Criteria And Biomechanical Surrogate To Evaluate Military Vehicle Occupant Injury During An Explosive Blast Event. Wayne State University Doctoral Dissertations. Paper 146.

Quenneville, C. E., & Dunning, C. E. (2012). Evaluation of the biofidelity of the HIII and MIL-Lx lower leg surrogates under axial impact loading. Traffic Injury Prevention, 13(1), 81–5.

Appendix A- Anatomical Terms

Ankle Inversion- Turning the foot inwards.

Ankle Eversion- Turing the foot outwards.

Anterior-Towards the front of the body. Example: The nose is on the anterior aspect of the head.

Comminuted- A fracture where a bone is fragmented into multiple pieces.

Diaphysis- The mid-section (straight part) of a long bone.

Distal- Further from the point of attachment. Example: The ankle is distal to the knee.

Dorsiflexion- Lifting the toes upwards. Example: Brining toes toward shin.

Forefoot- The ball of the foot.

Hindfoot- The heel of the foot.

Knee Extension- Straightening the knee.

Knee Flexion- Bending the knee.

Lateral- Away from the midline of the body. Example: The little toe is positioned laterally to the big toe.

Medial- Towards the midline of body. Example: The big toe is medial to the little toe.

Midfoot- The arch of the foot.

Plantarflexion- Moving the toes downward. Example: Pressing a gas pedal.

Posterior- Towards the rear of the body. Example: The heel is on the posterior aspect of the foot.

Proximal- Closer to the point of attachment. Example: The knee is proximal to the ankle.

Martini, F. H., Timmons, M. J., & Tallitsch, R. B. (2009). *Human Anatomy* (Sixth.). San Francisco, CA: Pearson Education Inc.

Appendix B- MATLAB® Code for Analyzing ATD

Posture Impacts without Boot

```
%%open files we are going to work with
fr= fopen ('E:\Sept27Oct4AtdTests\Sept27_oct4\DataDirectory.txt', 'r');
fw= fopen ('E:\Sept27Oct4AtdTests\DataOutputZPeakAlignmentNums.txt', 'w');
fin= fopen('E:\Sept27Oct4AtdTests\DataOutputZPeakAlignmentVar.txt', 'w');
fti= fopen('E:\Sept27Oct4AtdTests\DataOutputZPeakAlignmentTIs.txt', 'w');

%%Puts some headings in the files
fprintf(fin,'PosCat;Angle;Trial\n\n');
fprintf(fw,'Duration(s);Int(Chn);;;;;;;;;;abs(max(Chn));;;;;;;;;;Filename\n');
fprintf(fw,';IntUpperFx(N/s);IntUpperFy(N/s);IntUpperFz(N/s);IntUpperMx(Nm/s);IntUpperMy(Nm/s);Int
LowerFx(N/s);IntLowerFy(N/s);IntLowerFz(N/s);IntLowerMx(Nm/s);IntLowerMy(Nm/s);UpperFx(N);Up
perFy(N);UpperFz(N);UpperMx(Nm);UpperMy(Nm);LowerFx(N);LowerFy(N);LowerFz(N);LowerMx(N
m);LowerMy(Nm);\n');
fprintf(fti,'MaxTIup; MaxTIup Time; MaxFzUp; MaxFzlow; TI@MaxFzUp; MaxFzUp Time; MaxResM;
TI@MaxResM; MaxResM Time\n\n');

%%initial set up stuff

sensitivity=.10; %percent off of the mark for integration (in percent, 10% is good)
bounces=2; %number of times the channel can go up or down out of the sensitivity zone (i give it 2, even
makes most sense if you want whol wavelengths)
upwiggle=15; %margin of error for the impact (usually about 150)
dwnwiggle=15; % because the values are 0ed, the integral before will be zero anyways (anything over 20)

%%starts processing the first file, this counts the file number
for i=1:110 %100 for all files

%%Get the data from the file, and the filename
file{i}= fgets(fr);  %writes00 first filename to a line
file{i}=strcat(file{i});
ATDleg=dlmread(file{i}); %reads all the data from that filename into the matrix
ATDleg=ATDleg(:,1:(end-1)); %deletes last column, it is not data
tstep=(3/length(ATDleg)); %how long between each value (in seconds)

%%smooths smasher with butterworth filter
normfreq=(1250*2)/(3/length(ATDleg))^-1;
[b,a]=butter(2,normfreq);
filt=filter(b,a,ATDleg);
filtflip=flipud(filt);
filt2=filter(b,a,filtflip);
ATDleg=flipud(filt2);
```

```
%%puts information about the file into a line, then writes it to a seperate file
name=0;
name=file{i}(1:end);

if strfind(name,'Dorsi')
   fprintf(fin,'1;');
   fprintf(fin,'%s%s;', name(strfind(name,'Dorsi')+6), name(strfind(name,'Dorsi')+7));
end
if strfind(name,'Plant')
   fprintf(fin,'1;');
   fprintf(fin,'-%s%s;', name(strfind(name,'Plant')+6), name(strfind(name,'Plant')+7));
end

if strfind(name,'Ever')
      fprintf(fin,'2;');
      fprintf(fin,'%s%s;', name(strfind(name,'Ever')+5), name(strfind(name,'Ever')+6));
end
if strfind(name,'Inver')
      fprintf(fin,'2;');
      fprintf(fin,'-%s%s;', name(strfind(name,'Inver')+6), name(strfind(name,'Inver')+7));
end

if strfind(name,'Flex')
      fprintf(fin,'3;');
      fprintf(fin,'%s%s;', name(strfind(name,'Flex')+5), name(strfind(name,'Flex')+6));
end
if strfind(name,'Exten')
      fprintf(fin,'3;');
      fprintf(fin,'-%s%s;', name(strfind(name,'Exten')+6), name(strfind(name,'Exten')+7));
end

period = strfind(file{i},'.');
if str2num(name(period-1))==0
   fprintf(fin,'10');
else fprintf(fin,'%s', name(period-1));
end

fprintf(fin,'\n');

%%Check reading with a plot
%plot([0:size(vals,1)-1],vals);
%print('C:\Users\John Van Tuyl\Documents\ATDTESTWORKING\1Initialvals.jpg');

%0s the atd leg curves
for j=1:10
   sub=mean(ATDleg(1:100,j));
   for b=1:length(ATDleg)
      ATDleg(b,j)=ATDleg(b,j)-sub;
   end
end
```

```
%%Check zeroing with a plot
%plot([0:size(vals,1)-1],vals);
%print('C:\Users\John Van Tuyl\Documents\ATDTESTWORKING\2zeroed.jpg');

%%finds the maximum value for FZ lower (column 8)
[maxZlow,maxindex]= max(ATDleg(:,8));

%%computes the time the impact starts and stops based on a percent of maximum deviations
%%from 0, with wiggle room.  Tracks the lower Fz force channel
k=1; %this counts through each row in each file
while k<= size(ATDleg,1)
   if abs(ATDleg(k,8))>(sensitivity*maxZlow) %goes through rows, records rows when >sensitivity off
zero
       impact(k,1)=1;%there is impact here
   else impact(k,1)=0;
   end
k=k+1;
end

%%keeps track of each time the impact goes from a certain percent of the abs max down
k=1; %this counts through each row in each file
t=1;
counter=0;
while k<= size(ATDleg,1)-1
       if impact(k+1,1)~=impact(k,1)
          counter(t)=k;
          t=t+1;
       end
k=k+1;
end

%%computes the integral over the impact time for each channel
startint=counter(1)-dwnwiggle;
endint=counter(bounces)+upwiggle;
%endint=startint+300;

mres=0;
myadup=0;
TIup=0;
%%Calculates TI and Mres over impact
for j=1:length(ATDleg)
   %j=startint:endint
   myadup(j)=ATDleg(j,5)-(ATDleg(j,3)*0.02832);
   mres(j)=sqrt((myadup(j)^2)+(ATDleg(j,4)^2));
   TIup(j)=(ATDleg(j,3)/35900)+(mres(j)/225);
end

[MaxTIup,MaxTIupind]=max(TIup(startint:endint));
[MaxFzup,MaxFzind]= max(ATDleg((startint:endint),3));
[MaxFzlow,maxindex]= max(ATDleg((startint:endint),8));
```

```
[MaxMResup,MaxMResupind]= max(mres(startint:endint));

sub=0;
ypos=0;
j=1;
while j<= size(ATDleg,2)
integral(1,j)=0;
for k=startint:endint;
   ypos=(ATDleg(k,j)+ATDleg(k+1,j))/2;
sub=abs((ypos)*tstep);
integral(1,j)=integral(1,j)+sub;
%plotx=[vals(k,j),vals(k,j), vals(k+1,j),vals(k+1,j)]; %draws a box to check the integration
%ploty=[0, ypos, ypos, 0];
%ploty(k,j)=ypos; %draws a line to check the integration, hopefully makes it faster
end
j=j+1;
end

%Check duration with a plot
fs=20;
figure('Position', [50, 50, 1049, 895]);
hold off;
fzupplot=line(linspace(0,3,length(ATDleg)),ATDleg(:,3), 'linewidth', 3, 'color', [0 0 1]);
hold on;
fzlowplot=line(linspace(0,3,length(ATDleg)),ATDleg(:,8), 'linewidth', 3,'color', [0 0 .5]);
mxlowplot=line(linspace(0,3,length(ATDleg)),ATDleg(:,9)*10, 'linewidth', 3,'color', [0 .5 0]);
mxupplot=line(linspace(0,3,length(ATDleg)),ATDleg(:,4)*10, 'linewidth', 3,'color', [0 1 0]);
xlim([(startint-20)*tstep,(startint+200)*tstep]);
ylim([-1000,8000]);
ylabel('ForceZ (N)', 'fontsize', fs, 'FontName', 'Times')
set(gca,  'fontsize', fs, 'FontName', 'Times')
ax1=gca;
ax2=axes('ylim',[-.2
1.6],'Position',get(ax1,'Position'),'XAxis','bottom','YAxisLocation','right','Color','none','XColor','k','YColor','
k',  'fontsize', fs, 'FontName', 'Times');
tiplot=line(linspace(0,3,length(ATDleg)), TIup,'linewidth', 3,'Color',[1 0 0],'Parent', ax2);
plot([startint*tstep, startint*tstep],[-1000,10000], '--k', 'linewidth', 1,'Parent', ax1);
plot([endint*tstep,endint*tstep],[-1000,10000],'--k', 'linewidth', 1,'Parent', ax1);
xlim([(startint-20)*tstep,(startint+200)*tstep]);
xlabel('Time (s)', 'fontsize', fs, 'FontName', 'Times')
ylabel('TIAdj_U_p_p_e_r', 'fontsize', fs, 'FontName', 'Times')
legend([fzlowplot,fzupplot,mxlowplot,mxupplot,tiplot],'Fz_L_o_w_e_r','Fz_U_p_p_e_r','10 x
Mx_L_o_w_e_r','10 x Mx_U_p_p_e_r' ,'TIAdj_U_p_p_e_r','location', 'NorthEast', 'fontsize', fs, 'FontName',
'Times')
box on
set(gcf, 'PaperPositionMode', 'auto')
saveas(gcf,strcat('E:\Sept27Oct4AtdTests\Plots\', file{i}(end-15:end) ,'.bmp'));
clf;
close all
%Check integration with a plot
%plot([0:size(vals,1)-1],vals)
%plot(ploty);
```

```
%print('C:\Users\John Van Tuyl\Documents\ATDTESTWORKING\4integration.jpg');
%hold off

%%saves the data for this file into the big file
j=1;
fprintf(fw,'%f;',(endint-startint)*tstep);

while j<= size(ATDleg,2)
fprintf(fw,'%f;', integral(j));
j=j+1;
end

j=1;
while j<= size(ATDleg,2)
   fprintf(fw,'%f;', ATDleg(maxindex+(startint-1),j)); %%%%%%Switch these two
   %fprintf(fw,'%f;', ATDleg(MaxTIupind,j));
j=j+1;
end

fprintf(fw,'%s \n',file{i});
fprintf(fti,'%f;%f;%f;%f;%f;%f;%f;%f;%f\n',MaxTIup, (MaxTIupind+(startint-1))*tstep,
MaxFzup,MaxFzlow, TIup(MaxFzind+(startint-1)),(MaxFzind+(startint-
1))*tstep,MaxMResup,TIup(MaxMResupind),(MaxMResupind+(startint-1))*tstep);
end

%%close files that were used for reading and writing
fclose('all');
clear;
```

Appendix C- Hybrid III (Denton) Leg Schematic

U.S. Patent Dec. 18, 1984 Sheet 1 of 2 4,488,433

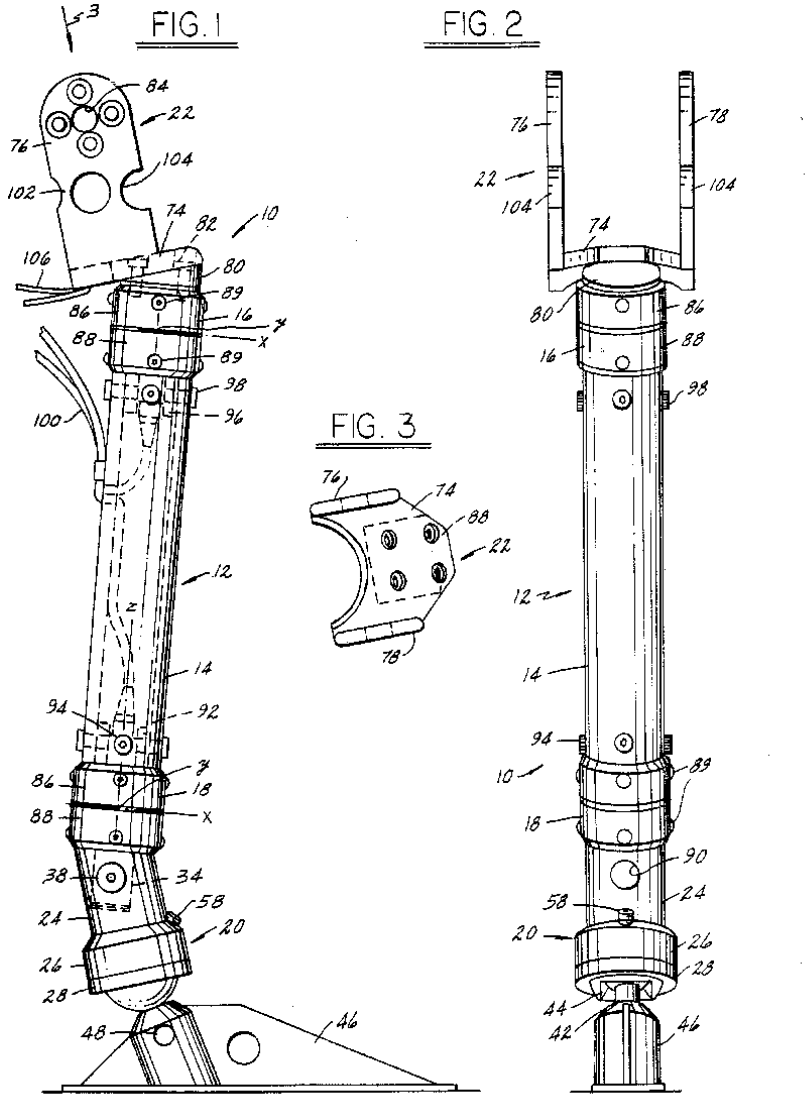

Denton, R. A., & Morgan, C. R. (1984, December 18). Crash test dummy lower leg structure. Google Patents. Retrieved from http://www.google.com/patents/US4488433

Appendix D- Calibration Fixture, Lower Tibia Load Cell

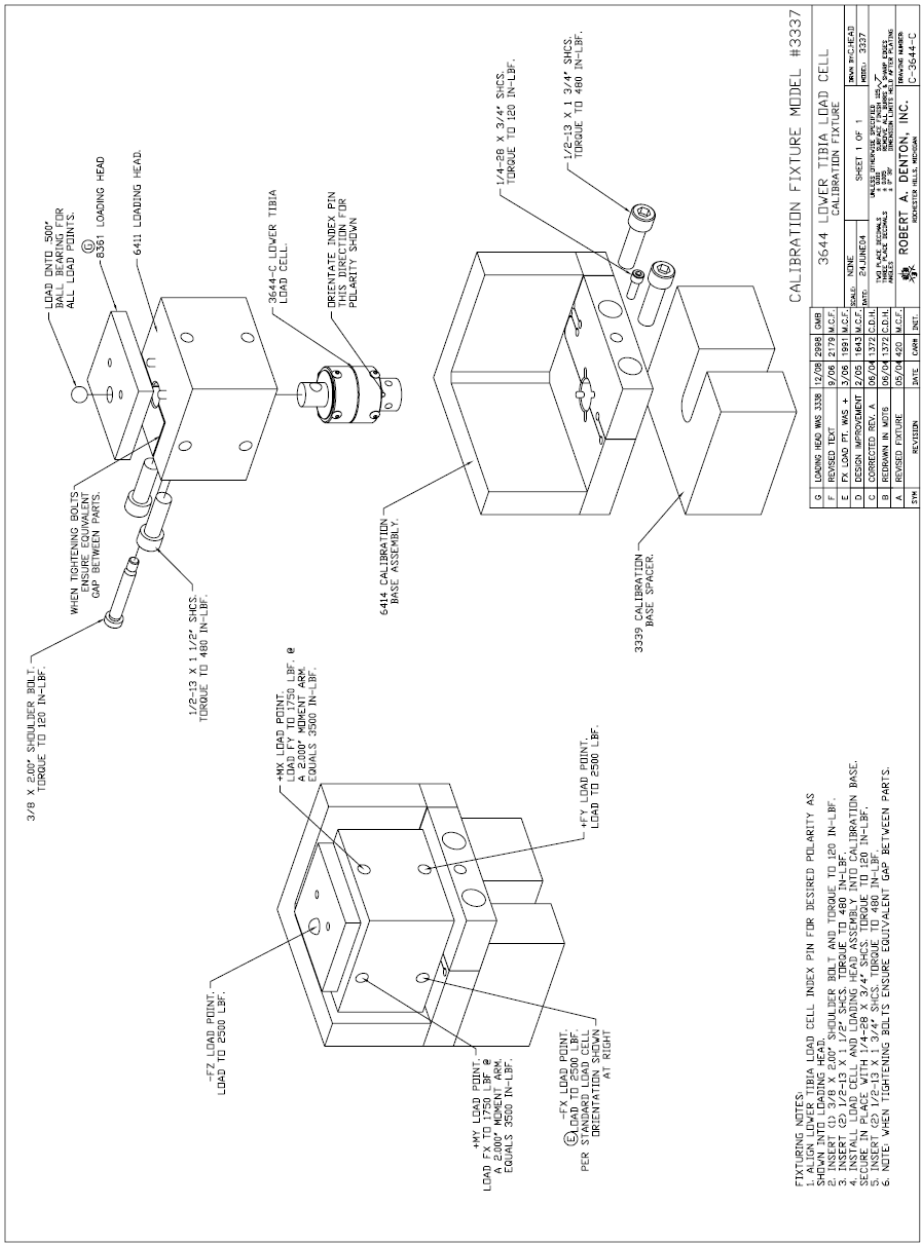

Humanetics Innovative Solutions, personal communication, April 28, 2014

Appendix E- Thor-Lx Lower Tibia Load Cell Diagram

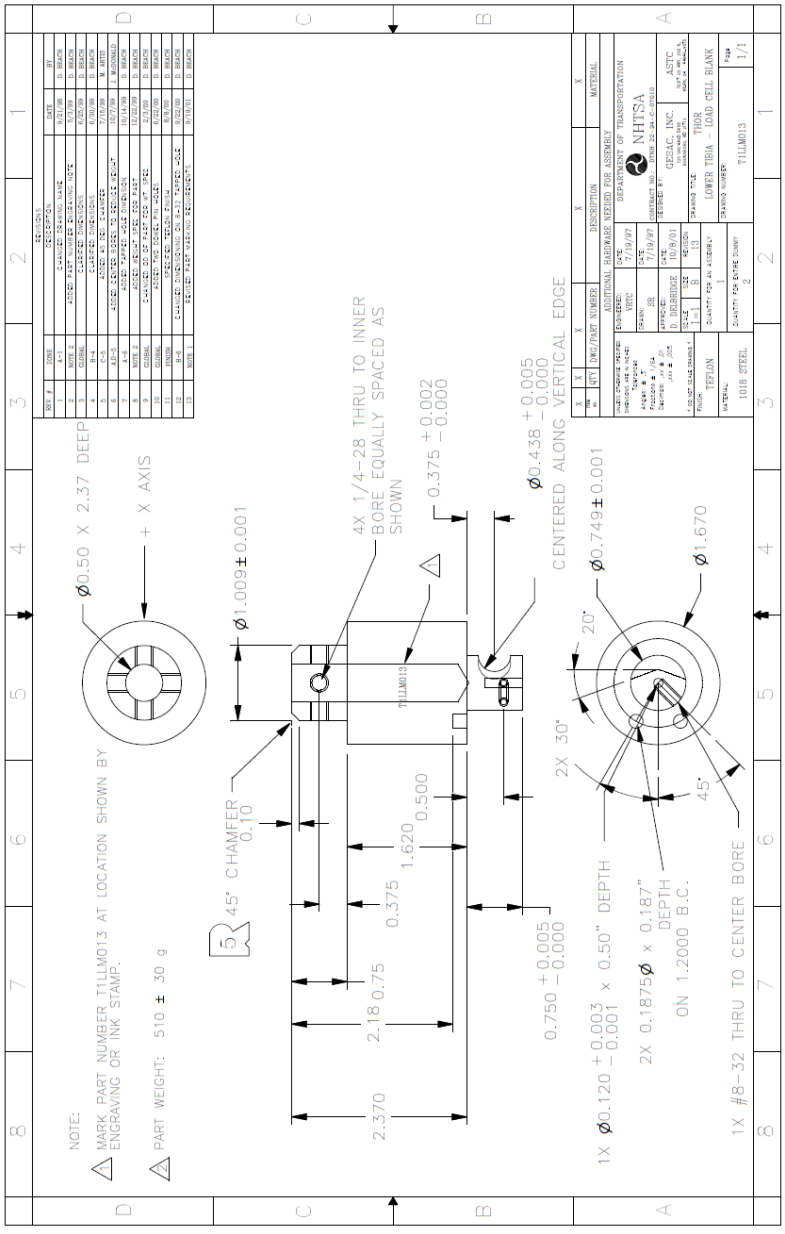

NHTSA. (2002). Thor-Lx Advanced Lower Extremity. Retrieved March 25, 2014, from http://www.nhtsa.gov/Research/Biomechanics+&+Trauma/Thor-Lx(HIIIr)+Advanced+Lower+Extremity

Appendix F- LabView® Data Acquisition Block Diagram for Sensors

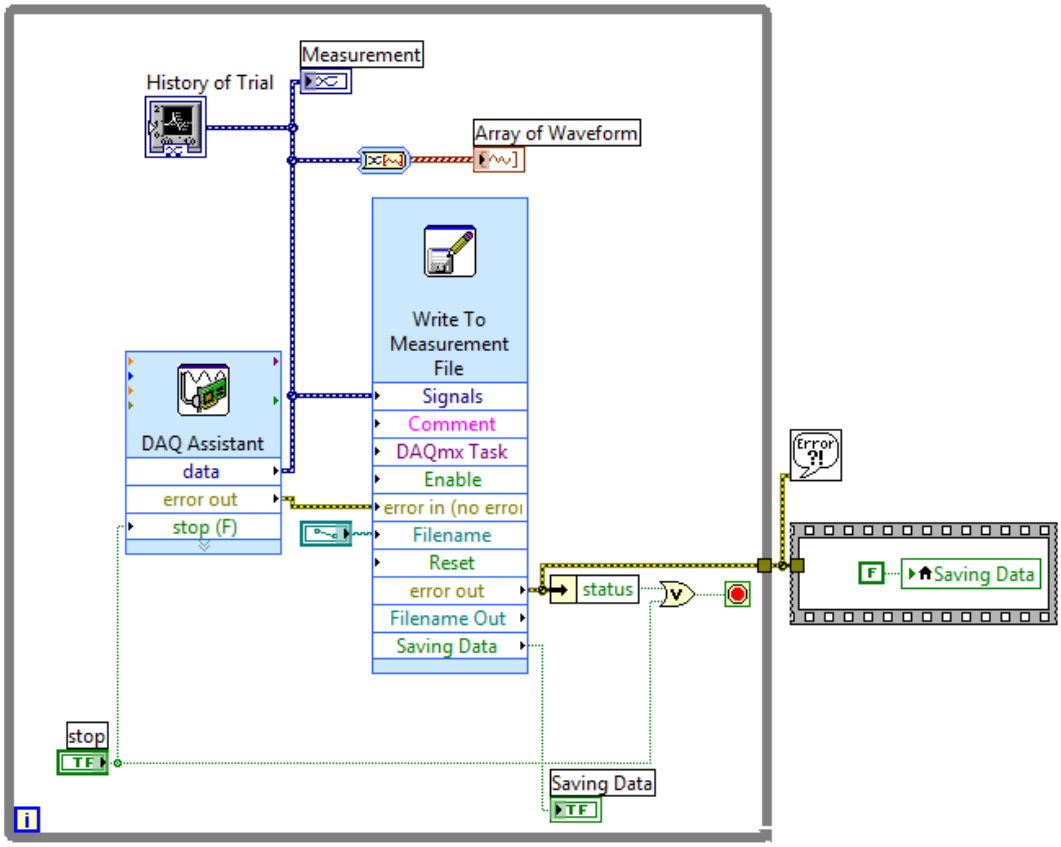

1.

2.

3.

Steps:
1. Use the DAQ Assistant Express VI to create and run task. To edit any Aquisition parameters, double click the DAQ Assistant Express VI
2. Write waveform data to file using the Write LabVIEW Measurement File Express VI. To view and edit any parameters regarding file I/O, double click the Express VI or right-click the Express VI and select "Properties."
3. Check for errors and reinitialize the Saving Data Boolean Indicator

Appendix G- MATLAB® Code For Sensor Calibration Curves

```
% dir /s/b >testerdir.txt
ftester= fopen ('C:\Users\John\Dropbox\Boot Sensor\Results\TestResults\March5\Tester\testerdirlap.txt',
'r');
fpiezo= fopen ('C:\Users\John\Dropbox\Boot
Sensor\Results\TestResults\March5\Labview\labviewdirlap.txt', 'r');
fw= fopen ('C:\Users\John\Dropbox\Boot Sensor\Results\TestResults\calibrationcurves.txt', 'w');

for k=1:24 %24
start=1;
close all;
i=1;
j=1;
voltage=0;
resistance=0;
pressure=0;
f=0;

file{k}= fgets(fpiezo);
file{k}=strcat(file{k});
piezo=lvm_import(file{k},0);

file{k}= fgets(ftester);
file{k}=strcat(file{k});
instron=xlsread(file{k});

t1=[instron(1,1) instron(1,2) instron(1,3)];
t1=(t1(1)*3600) + (t1(2)*60) + t1(3);
t2=[str2double(piezo.Time(1:2)) str2double(piezo.Time(4:5)) str2double(piezo.Time(7:end))];
t2=(t2(1)*3600) + (t2(2)*60) + t2(3);
secel= t1-t2;

legnums=instron(4:end,:);
numpoints=length(legnums);

if str2num(file{k}(end-9)) == 1
pressure=legnums(:,3)/(.04*.05);
area=(.04*.05);
elseif str2num(file{k}(end-9)) == 4
pressure=legnums(:,3)/(.04*.05);
area=(.04*.05);
elseif str2num(file{k}(end-9)) == 6
pressure=legnums(:,3)/(.04*.05);
area=(.04*.05);
```

```
elseif str2num(file{k}(end-9)) == 8
pressure=legnums(:,3)/(.04*.05);
area=(.04*.05)
elseif str2num(file{k}(end-9)) == 2
pressure=legnums(:,3)/(.04*.025);
area=(.04*.025);
elseif str2num(file{k}(end-9)) == 3
pressure=legnums(:,3)/(.04*.025);
area=(.04*.025);
elseif str2num(file{k}(end-9)) == 5
pressure=legnums(:,3)/(.04*.025);
area=(.04*.025);
elseif str2num(file{k}(end-9)) == 7
pressure=legnums(:,3)/(.04*.025);
area=(.04*.025);
end
%time=(0:0.1:piezo.Segment1.data(end,1)-secel)';
%time=time(1:numpoints);
for i=1:(length(piezo.Segment1.data)/100)
   voltage(i)=mean(piezo.Segment1.data(((100*(i-1))+1):(100*i),2));
end

voltage=voltage(round(secel/0.1):end)';
voltage=voltage(1:numpoints);

for i=1:length(voltage)
resistance(i)=(102/(1/voltage(i)-1));
if pressure(i)>.5E4 %4E4
   start(j)=i;
   j=j+1;
end
end
fs=20;
x=resistance(start(1):end);
y=pressure(start(1):end);
figure('Position', [50, 50, 1049, 895]);
s=plot(resistance,pressure,'linewidth', 3 , 'color', 'r');
xlim([0,200])
xlabel('Resistance (\Omega)', 'fontsize', fs, 'FontName', 'Times');
ylabel ('Pressure (Pa)','fontsize', fs, 'FontName', 'Times');
ylim([0, 3.5E5])
set(gca, 'fontsize', fs, 'FontName', 'Times')
f=ezfit(x,y,'((a*x^b)+c);a=6E6; b=-1.5; c=20000'); %(a+(a*x))*exp(-b*x); a=1200')");
showfit(f, 'dispeqboxmode', 'off', 'boxlocation',  [0.60 0.81 0.1 0.1], 'fitlinestyle', '--','fitcolor', 'k',
'fitlinewidth', 3);
%legend([s], 'Sensor', '- Fit', 'fontsize', fs, 'FontName', 'Times')
saveas(gcf,strcat('C:\Users\John\Dropbox\Boot Sensor\Results\TestResults\plate', file{k}(end-9), 'test',
file{k}(end-4), '.bmp'));
fprintf(fw,'%d %d %d %d %d\n',f.m(1), f.m(2), f.m(3), f.r, area);
end
```

Appendix H- MATLAB® Code to Average Multiple Sensor Calibration Curves

```
clear
favcurves= fopen ('C:\Users\John\Dropbox\Boot Sensor\Results\TestResults\avcalibrationcurves.txt', 'w');
curves= dlmread('C:\Users\John\Dropbox\Boot Sensor\Results\TestResults\calibrationcurves.txt');

x=linspace(10,400,1000);

for i=1:3:24
    close all;
    for j=1:length(x)
   y1(j)=(curves(i,1)*x(j)^(curves(i,2)))+curves(i,3);
   y2(j)=(curves(i+1,1)*x(j)^(curves(i+1,2)))+curves(i+1,3);
   y3(j)=(curves(i+2,1)*x(j)^(curves(i+2,2)))+curves(i+2,3);
   y(j)=mean([y1(j),y2(j),y3(j)]);
    end

    fs=20;
    area=curves(i,5);
    figure('Position', [50, 50, 1049, 895]);
    hold on
    one=plot(x,y1,'c', 'linewidth', 2)
    two=plot(x,y2,'g', 'linewidth', 2)
    three=plot(x,y3, 'b', 'linewidth', 2)
    av=plot(x,y,'r', 'linewidth', 2)
    set(gca, 'fontsize', fs, 'FontName', 'Times')
    xlabel('Resistance (\Omega)', 'fontsize', fs, 'FontName', 'Times');
    ylabel ('Pressure (Pa)','fontsize', fs, 'FontName', 'Times');
    xlim([0 200])
    ylim([0 350000])
    legend([one, two, three, av],'Trial 1', 'Trial 2', 'Trial 3', 'Average', 'fontsize', fs, 'FontName', 'Times')
    f=ezfit(x,y,'y(x)=(a*x^n)+c ;a=6E6; n=-1.5; c=20000'); %(a*exp(x*n))-(a*x*exp(x*n)); a=1;n=-1");
    set(gcf, 'PaperPositionMode', 'auto')
    showfit(f,'dispeqboxmode', 'off', 'boxlocation',  [0.60 0.81 0.1 0.1], 'fitlinestyle', '--','fitcolor', 'k',
'fitlinewidth', 3);
    saveas(gcf,strcat('C:\Users\John\Dropbox\Boot Sensor\Results\TestResults\', num2str(i), '.jpg'));
    fprintf(favcurves,'%d %d %d %d %d\n',f.m(1), f.m(2), f.m(3), f.r, area);
end
```

Appendix I- MATLAB® Code to Analyze Quasi-Static Boot Tests

```
ftester= fopen ('E:\March67TestsLondon\Quasi\Instron\testerdirlap.txt', 'r');
fpiezo= fopen ('E:\March67TestsLondon\Quasi\Piezo\piezodirlap.txt', 'r');
fw= fopen ('E:\March67TestsLondon\Quasi\quasiresults.txt', 'w');
curves= dlmread('C:\Users\John\Dropbox\Boot Sensor\Results\TestResults\avcalibrationcurves.txt');
fprintf(fw,'file averageerror slope instronintegral bootintegral percentcap sensav1 senssd1 sensav2 senssd2
sensav3 senssd3 sensav4 senssd4 sensav5 senssd5 sensav6 senssd6 sensav7 senssd7 sensav8 senssd8\n');
rate=2/60; %2mm/min= 2/60 mm/s

for k=1:11 %12 for all, 11 not including the haging boot pre fit
close all;
clf;
i=1;
j=1;
k=1;
in=0;
pks=0;
forcea=0;
force=0;
senper=0;

file{k}= fgets(fpiezo);
file{k}=strcat(file{k});
piezo=lvm_import(file{k},0);
sensors=[piezo.Segment1.data(:,2) piezo.Segment1.data(:,4) piezo.Segment1.data(:,6)
piezo.Segment1.data(:,8) piezo.Segment1.data(:,10) piezo.Segment1.data(:,12) piezo.Segment1.data(:,14)
piezo.Segment1.data(:,16)];
pulse=piezo.Segment1.data(:,18);
%time=piezo.Segment1.data(:,1);

file{k}= fgets(ftester);
file{k}=strcat(file{k});
ATDleg=dlmread(file{k}, '\t');
instron=-ATDleg(:,11);
ATDleg=ATDleg(:,1:10);

numpoints=length(instron);
[pks, in] = findpeaks(-pulse, 'threshold', 0.0075);

%{
hold on
plot(pulse)
plot(in(1), -pks, 'o')
xlim([0,500])
```

```
pause(1) %in seconds
%}

sensors=sensors(in(1):in(1)+numpoints-1, :);

%transform to resistance
for i=1:length(sensors)
   for j=1:8
sensors(i,j)=(102/(1/sensors(i,j)-1));
   end
end

%transfrom to force based on curve
for i=1:8
   for j=1:length(sensors)
   forcea(j,i)=(curves(i,1)*sensors(j,i)^curves(i,3)+curves(i,2))*curves(i,5);
   end
end

%0s the sensor force curves
for j=1:8
   sub=mean(forcea(1:100,j));
   for i=1:length(forcea)
      force(i,j)=forcea(i,j)-sub;
   end
end

%0s the atd leg curves
for j=1:10
   sub=mean(ATDleg(5:10,j));
   for i=1:length(ATDleg)
      ATDleg(i,j)=ATDleg(i,j)-sub;
   end
end

%0s the instron
 sub=mean(instron(5:10));
   for i=1:length(instron)
      instron(i)=instron(i)-sub;
   end

%calcs where the force passed a certain threshold
for i=1:length(instron)
   if instron(i)<1
      startplot=i;
   end
   if instron(i)<50
      startint=i;
   end
end
```

```
%sum across all and calculate some values
totforce=sum(force,2);
[fzmax,fzmaxin]=max(instron);
bootatmax=totforce(fzmaxin);

for i=startint:fzmaxin
averror=abs(instron(i)-totforce(i))/instron(i);
end
averror=mean(averror);

%slope
calcdist=round(length(instron)*.01*rate)/2;
if (fzmaxin-(calcdist/.01*rate))<1
   calcdist=round(length(instron)*.01)/3;
end
activex=((startint*.01*rate):.01*rate:(fzmaxin*.01*rate))';
activey=instron(startint:fzmaxin);
slopein=polyfit(activex,activey,1);

%integrates under load cell curve
intinstron=0;
for w=1:fzmaxin;
   ypos=(instron(w)+instron(w+1))/2;
   sub=abs((ypos)*0.01*rate);
   intinstron=intinstron+sub;
end

%integrates under boot curve
intboot=0;
for w=1:fzmaxin;
   ypos=(totforce(w)+totforce(w+1))/2;
   sub=abs((ypos)*0.01*rate);
   intboot=intboot+sub;
end

%% calculates the % that each sensor contribues to the total
for j=1:8
   for i=startint:length(totforce)
      senper(i,j)=(abs(force(i,j))/totforce(i))*100;
   end
end
avsenper=mean(senper,1);
sdsenper=std(senper,1);

fs=20;
figure('Position', [50, 50, 1049, 895]);
hold on
h1=plot((0:0.01*rate:(length(totforce)-1)*0.01*rate),totforce,'linewidth', 3,'color','r');
%h2=plot((0:0.01*rate:(length(totforce)-1)*0.01*rate),force,'linewidth', .5, 'color','g');
x=(0:0.01*rate:(length(totforce)-1)*0.01*rate);
```

```
y=(slopein(1)*x)+slopein(2);
h3=plot(x,y,'--k','linewidth', 1);
%h4=plot((0:0.01*rate:(length(totforce)-1)*0.01*rate),senper, 'color','m');
ylabel('Force (N)', 'fontsize', fs, 'FontName', 'Times')
xlabel('Position (mm)', 'fontsize', fs, 'FontName', 'Times')
ylim([0, inf])
%ylim([0, 1000])
xlim([startplot*.01*rate, fzmaxin*.01*rate])
hin=plot((0:0.01*rate:(length(instron)-1)*0.01*rate),instron(:),'linewidth', 3,'color','b');
legend([hin, h1], 'Load Cell','Boot Force',  'fontsize', fs, 'FontName', 'Times','location', 'NorthWest')
box on
set(gca, 'fontsize', fs, 'FontName', 'Times')
set(gcf, 'PaperPositionMode', 'auto')
saveas(gcf,strcat('E:\March67TestsLondon\Quasi\test', file{k}(end-10:end),'.bmp'));
fprintf(fw, '%s %d %d %d %d %d %d %d %d %d %d %d %d %d %d %d %d %d %d %d %d
\n',file{k}(end-10:end), averror*100, slopein(1), intinstron, intboot, intboot*100/intinstron,
avsenper(1),sdsenper(1),avsenper(2),sdsenper(2),avsenper(3),sdsenper(3),avsenper(4),sdsenper(4),avsenper
(5), sdsenper(5),avsenper(6),sdsenper(6),avsenper(7),sdsenper(7),avsenper(8),sdsenper(8));
end
close all
```

Appendix J- MATLAB® Code to Analyze Dynamic Boot Tests

```
% dir /s/b >testerdir.txt
%open files for reading
ftester= fopen ('E:\March67TestsLondon\Dynamic\Smasher\smasherdirlap.txt', 'r');
fpiezo= fopen ('E:\March67TestsLondon\Dynamic\Piezo\piezodirlap.txt', 'r');
fw= fopen ('E:\March67TestsLondon\Dynamic\dynamicresults.txt', 'w');
curves= dlmread('C:\Users\John\Dropbox\Boot Sensor\Results\TestResults\avcalibrationcurves.txt');
fprintf(fw,'file, mxmax, mxmin, my, mres, fzmax, maxboot, minbootpre, minbootpost,
fzmax/(abs(minbootpre)+maxboot), p1, p2, p3, p4, p5, p6, p7, p8, duration \n');

format short %double will give larger precision, but increase runtime

for k=1:23 %23 does all the dynamic runs

close all; %some setup stuff
clf;
i=1;
j=1;
in(1)=1;
in2(1)=1;
pks=0;
force=0;
forcea=0;
use1=0;
use2=0;

file{k}= fgets(fpiezo); %reads in the boot files
file{k}=strcat(file{k});
piezo=lvm_import(file{k},0);
sensors=[piezo.Segment1.data(:,2) piezo.Segment1.data(:,4) piezo.Segment1.data(:,6)
piezo.Segment1.data(:,8) piezo.Segment1.data(:,10) piezo.Segment1.data(:,12) piezo.Segment1.data(:,14)
piezo.Segment1.data(:,16)];
pulse=piezo.Segment1.data(:,18);

file{k}= fgets(ftester); %reads in the leg files
file{k}=strcat(file{k});
ATDleg=dlmread(file{k}, '\t');

%%smooths smasher with butterworth filter
normfreq=(1250*2)/(3/length(ATDleg))^-1;
[b,a]=butter(2,normfreq);
filt=filter(b,a,ATDleg);
filtflip=flipud(filt);
```

```
filt2=filter(b,a,filtflip);
ATDleg=flipud(filt2);

%0s the atd leg curves
for j=1:10
   sub=mean(ATDleg(1:100,j));
   for i=1:length(ATDleg)
      ATDleg(i,j)=ATDleg(i,j)-sub;
   end
end

%{
%%smooths with average
average=12;
for i=(1+(average/2)):(length(smasher(:,8))-(average/2))
fz(i)= mean(smasher((i-(average/2)):(i+(average/2)),8));
end
fz=[zeros((average/2),1); fz'];
%}

%%computes the time the impact starts and stops based on a percent of maximum deviations
fz=ATDleg(:,8);
for p= 1:length(fz)
   if abs(fz(p))>(0.1*abs(max(fz))) %goes through rows, records rows when >sensitivity off zero
      impact(p,1)=1;%there is impact here
   else impact(p,1)=0;
   end
end

%%keeps track of each time the impact goes from a certain percent of the abs max down
t=1;
counter=0;
for p= 1:length(fz)-1
      if impact(p+1,1)~=impact(p,1)
         counter(t)=p;
         t=t+1;
      end
end
startint=counter(1)-15;
endint=counter(2)+15;

%transform all the boot infomation to resistance
for i=1:length(sensors)
   for j=1:8
   sensors(i,j)=(102/(1/sensors(i,j)-1));
   end
end

%transfrom to force based on calibration curves, and accounts for the area of the sensors
for i=1:length(sensors)
   for j=1:8
```

```
        forcea(i,j)=(curves(j,1)*sensors(i,j)^curves(j,3)+curves(j,2))*curves(j,5);
    end
end

%0s the sensor force curves
for j=1:8
    sub=mean(forcea(1:100,j));
    for i=1:length(forcea)
        force(i,j)=forcea(i,j)-sub;
    end
end

%%Calculates TI and Mres over impact
myadup=0;
myadlow=0;
mresup=0;
mreslow=0;
TIup=0;
TIlow=0;

for j=1:length(ATDleg)
    myadup(j)=ATDleg(j,5)-(ATDleg(j,3)*0.02832);
    myadlow(j)=ATDleg(j,10)-(ATDleg(j,8)*0.006398);
    mresup(j)=sqrt((myadup(j)^2)+(ATDleg(j,4)^2));
    mreslow(j)=sqrt((myadlow(j)^2)+(ATDleg(j,9)^2));
    TIup(j)=(ATDleg(j,3)/35900)+(mresup(j)/225);
    TIlow(j)=(ATDleg(j,8)/35900)+(mreslow(j)/225);
end

[MaxMxlow,MaxMxlowind]= max(ATDleg((startint:endint),9));
[MinMxlow,MinMxlowind]= min(ATDleg((startint:endint),9));
[MaxMylow,MaxMylowind]= max(ATDleg((startint:endint),10));
[MinMylow,MinMylowind]= min(ATDleg((startint:endint),10));
[MaxFzlow,MaxFzlowind]= max((ATDleg((startint:endint),8)));
[MaxMReslow,MaxMReslowind]= max(mreslow(startint:endint));
[MaxTIlow,MaxTIlowind]=max(TIlow(startint:endint));

%%use this if aligning by pulse
%{
pulse=pulse-mean(pulse(1000:1100));
pulse=[zeros(2000,1);pulse];

for i=(1000+2000):length(pulse)
  if pulse(i)>.08
   in2(1)=i;
   use2=1;
  end
  if pulse(i)<-.08
   in(1)=i;
   use1=1;
  end
```

```
end

if use1==true
   start=in(1);
elseif use2==true
   start=in2(1)-(round(0.98/5.000000E-5));
end
force=force(start:end, :);
%{
hold on
plot(0:(5E-5):((length(pulse)-1)*5E-5), pulse)
plot(in2(1)*5E-5, pulse(in2(1)), 'oy')
plot(in(1)*5E-5, pulse(in(1)), 'og')
plot(start*5E-5,pulse(start), 'or')
xlim([0,2])
ylim([-.25,.25])
saveas(gcf,strcat('E:\March67TestsLondon\Dynamic\start', file{k}(end-10:end),'.jpg'));
hold off
close all
%}
%}

force=[zeros(2000,8); force];
totforce=sum(force,2);
abstotforce=sum(abs(force),2);

%%use this if aligning by peak
[fzmax,fzmaxin]=max(fz(startint:endint));
fzmaxin=startint+fzmaxin;
[maxboot, maxbootin]=max(totforce);
[minbootpre, minbootprein]=min(totforce(1:maxbootin));
[minbootpost, minbootpostin]=min(totforce(maxbootin:(maxbootin+500)));
diff=(fzmaxin*(3/length(fz)))/5E-5;
totforcealigned=totforce(round(maxbootin-diff):end,1);
forcealigned=force(round(maxbootin-diff):end,:);
durationleg=(endint-startint)*3/length(ATDleg);

%% calculates the % that each sensor contribues to the total
for j=1:8
   for i=maxbootin-100:maxbootin+100
senper(i,j)=(abs(force(i,j))/abstotforce(i))*100;
   end
end
 %%output
fs=20;
figure('Position', [50, 50, 1049, 895]);
h1=line(linspace(0,3,length(fz)),fz,'Color',[0 0 1], 'linewidth',3);
mxlowplot=line(linspace(0,3,length(ATDleg)),ATDleg(:,9)*10, 'linewidth', 3,'color', [0 .5 0]);
hold on
xlim([startint*3/length(fz)-.005,startint*3/length(fz)+.025])
ylim([-2000 3500])
```

```
ylabel('ForceZ_L_o_w_e_r (N)', 'fontsize', fs, 'FontName', 'Times')
set(gca,  'fontsize', fs, 'FontName', 'Times')
ax1=gca;
ax2=axes('ylim',[-200
350],'Position',get(ax1,'Position'),'XAxis','bottom','YAxisLocation','right','Color','none','XColor','k','YColor',
'k', 'fontsize', fs, 'FontName', 'Times');
h2=line((0:5E-5:(length(totforcealigned)-1)*5E-5),totforcealigned,'linewidth', 3,'Color',[1 0 0],'Parent',
ax2);
xlim([startint*3/length(fz)-.005,startint*3/length(fz)+.025])
xlabel('Time (s)', 'fontsize', fs, 'FontName', 'Times')
ylabel('Boot Force (N)', 'fontsize', fs, 'FontName', 'Times')
h3=plot([startint*3/length(fz), startint*3/length(fz)], [-4000, 4000], '--k ','Parent', ax1);
h4=plot([endint*3/length(fz), endint*3/length(fz)], [-4000, 4000], '--k','Parent', ax1);
%h5=line((0:5E-5:(length(totforcealigned)-1)*5E-5),forcealigned,'linewidth', 1,'Color',[0 1 0],'Parent', ax2);
%tit=title(file{k}(end-10:end));
legend([h1,mxlowplot, h2], 'Fz_L_o_w_e_r','10 x Mx_L_o_w_e_r','Boot Force', 'fontsize', fs, 'FontName',
'Times');
%set(gcf, 'Position', [100, 100, 1049, 895])
box on
set(gcf, 'PaperPositionMode', 'auto')
saveas(gcf,strcat('E:\March67TestsLondon\Dynamic\SmoothPeak', file{k}(end-10:end),'.bmp'));
%orient landscape
%saveas(gcf,strcat('E:\March67TestsLondon\Dynamic\SmoothPeak', file{k}(end-10:end),'.pdf'));
fprintf(fw, '%s %d %d %d %d %d %d %d %d %d %d %d %d %d %d %d %d %d\n',file{k}(end-
10:end), MaxMxlow, MinMxlow, MaxMylow, MaxMReslow, fzmax, maxboot, minbootpre, minbootpost,
fzmax/(abs(minbootpre)+maxboot), senper(maxbootin,1), senper(maxbootin,2), senper(maxbootin,3),
senper(maxbootin,4),senper(maxbootin,5),senper(maxbootin,6),senper(maxbootin,7),senper(maxbootin,8),
durationleg);
end
 close all
```

Appendix K- Calibration Curve Summary

$$Pressure\ (Pa) = a * Resistance\ (\Omega)^b + c$$

Plate	*a*	*b*	*c*	R^2
1	4.11E+06	-1.22	5.81E+03	0.999
1	4.91E+06	-1.30	5.55E+03	0.999
1	3.21E+06	-1.13	5.08E+03	1.000
2	1.75E+07	-1.45	6.06E+03	0.999
2	2.62E+07	-1.58	4.88E+03	1.000
2	2.30E+07	-1.52	3.87E+03	0.999
3	8.81E+06	-1.26	9.98E+03	0.999
3	9.16E+06	-1.32	1.20E+04	0.998
3	9.86E+06	-1.32	1.15E+04	0.999
4	9.27E+06	-1.47	1.02E+04	0.998
4	5.41E+06	-1.32	8.81E+03	0.998
4	5.83E+06	-1.33	7.70E+03	0.998
5	9.60E+06	-1.32	8.72E+03	0.999
5	1.16E+07	-1.36	8.54E+03	0.999
5	1.06E+07	-1.32	6.39E+03	0.999
6	1.00E+07	-1.40	1.08E+03	1.000
6	1.22E+07	-1.42	4.43E+03	1.000
6	1.69E+07	-1.46	5.71E+03	0.999
7	1.45E+07	-1.38	6.61E+03	1.000
7	9.95E+06	-1.27	7.67E+03	0.999
7	9.85E+06	-1.28	8.85E+03	0.999
8	4.66E+06	-1.36	4.70E+03	0.999
8	6.53E+06	-1.49	7.24E+03	0.999
8	5.37E+06	-1.46	7.59E+03	0.999

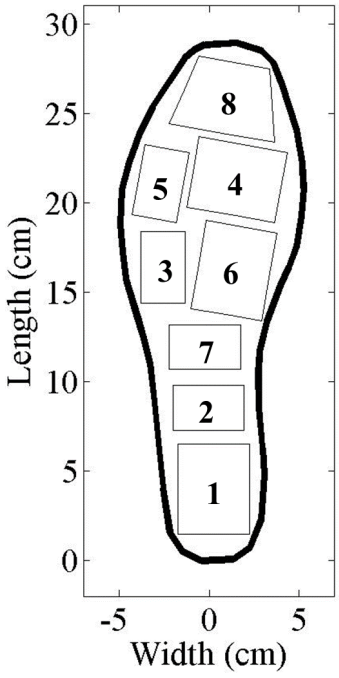

Appendix L- MATLAB® Code for Force Visualization

```
close 'all'
piezo=lvm_import('E:\March67TestsLondon\Dynamic\Piezo\001_002.txt',0);
curves= dlmread('C:\Users\John\Dropbox\Boot Sensor\Results\TestResults\avcalibrationcurves.txt');
num = xlsread('C:\Users\John\Dropbox\Boot
Sensor\DataAquisitionandPlottingprograms\Insole_workpoints.xls');
m=1;

sensors=[piezo.Segment1.data(:,2) piezo.Segment1.data(:,4) piezo.Segment1.data(:,6)
piezo.Segment1.data(:,8) piezo.Segment1.data(:,10) piezo.Segment1.data(:,12) piezo.Segment1.data(:,14)
piezo.Segment1.data(:,16)];

%transform all the boot infomation to resistance
for i=1:length(sensors)
   for j=1:8
   sensors(i,j)=(102/(1/sensors(i,j)-1));
   end
end

%transfrom to force based on calibration curves, and accounts for the area of the sensors
for i=1:length(sensors)
   for j=1:8
      forcea(i,j)=(curves(j,1)*sensors(i,j)^curves(j,3)+curves(j,2))*curves(j,5);
   end
end

%0s the sensor force curves
for j=1:8
   sub=mean(forcea(1:100,j));
   for i=1:length(forcea)
      force(i,j)=forcea(i,j)-sub;
   end
end

[fmax,fmaxin]=max(force(:,1));
[fmin,fminin]=min(force(:,1));

for i=round(linspace((fmaxin-100),(fmaxin+100),50))
  %i=fmaxin
   %(fmaxin-100):100:(fmaxin+100) %this is the number corresponding to the impact, otherwise to many
frames

%%Locations of Sensor Centres and edge points
%x=[0; 0; 0; -2; 2; -4; 3; -1; num(:,1)];
%y=[2; 5; 7; 15; 15 ;20; 20 ;26; num(:,2)];

%%Sensor 8 points
```

```
sens1x=[-2;0;2;2;2;0;-2;-2]-.1;
sens1y=[2;2;2;4.5;7;7;7;4.5]-.4;
sens1force=ones([8,1])*force(i,1);

sens2x=[-2;0;2;2;2;0;-2;-2]+.2;
sens2y=[8;8;8;9.25;10.5;10.5;10.5;9.25]-.6;
sens2force=ones([8,1])*force(i,2);

sens3x=[-2;0;2;2;2;0;-2;-2]+.4;
sens3y=[11.5;11.5;11.5;12.75;14;14;14;12.75]-.7;
sens3force=ones([8,1])*force(i,3);

sens4x=[0;1.25;2.5;2.5;2.5;1.25;0;0]+1.5;
sens4y=[0;0;0;2;4;4;4;2]+14.5;
sens4force=ones([8,1])*force(i,4);

sens5x=[0;1.231;2.462;2.1147;1.7674;.5364;-.6946;-.3473]+2;
sens5y=[0;.2171;.4341;2.4037;4.3734;4.1563;3.939;1.9696]+19;
sens5force=ones([8,1])*force(i,5);

sens6x=[0;2.462;4.924;4.5767;4.2294;1.7674;-.6946;-.3473]-3.5;
sens6y=[0;.4341;.8682;2.8379;4.8075;4.3734;3.9392;1.9696]+19;
sens6force=ones([8,1])*force(i,6);

sens7x=[0;1.9696;3.9392;3.5051;3.071;1.1014;-.86820;-.4341]-2.75;
sens7y=[0;.3473;.6946;3.1566;5.6186;5.2713;4.924;2.462]+13.5;
sens7force=ones([8,1])*force(i,7);

sens8x=[0;2.9544;5.9088;5.0691;4.2294;2.2598;.2902;.1451]-3.5;
sens8y=[0;.5209;1.0419;2.9247;4.8075;4.4602;4.1129;2.0564]+23.5;
sens8force=ones([8,1])*force(i,8);

edgex=num(:,1);
edgey=num(:,2);
edgeforce=zeros(length(num(:,1)),1);

%{
hold on
plot(sens1x,sens1y,'b-o')
plot(sens2x,sens2y,'k-o')
plot(sens3x,sens3y,'g-o')
plot(sens3x,sens3y,'m-o')
plot(sens4x,sens4y,'c-o')
plot(sens5x,sens5y,'b-o')
plot(sens6x,sens6y,'k-o')
plot(sens7x,sens7y,'r-o')
plot(sens8x,sens8y,'r-o')
%}

x=[sens1x;sens2x;sens3x;sens4x;sens5x;sens6x;sens7x;sens8x;edgex];
```

```
y=[sens1y;sens2y;sens3y;sens4y;sens5y;sens6y;sens7y;sens8y;edgey];

sensorforce=[sens1force;sens2force;sens3force;sens4force;sens5force;sens6force;sens7force;sens8force;ed
geforce];
SinglePointsensorforce=[ force(i,1);force(i,2); force(i,3); force(i,4);  force(i,5); force(i,6); force(i,7);
force(i,8)];

%for testing
%sensorforce=[ones([8,1])*2;ones([8,1])*3;ones([8,1])*1;ones([8,1])*5;ones([8,1])*6;ones([8,1])*7;ones([
8,1])*8;ones([8,1])*9;edgeforce];

[qx,qy]=meshgrid((-5:.05:5),(0:.05:30));
F = TriScatteredInterp(x,y,sensorforce,'natural');%vs natural linear nearest
qz = F(qx,qy);

clf;
mesh(qx,qy,qz);
hold on
daspect([1 1 6])
%plot3(x,y,sensorforce,'o');
zoff=ones(length(num),1);
plot3(num(:,1),num(:,2),zoff,'-k','LineWidth',4);
set(gca, 'FontName', 'Times', 'Fontsize', 20)
zlabel('Force (N)')
xlabel('Width (cm)')
ylabel('Length (cm)')
box on
grid off
cb=colorbar('FontName', 'Times', 'Fontsize', 20);
ylabel(cb, 'Force (N)')
caxis([-60, 150]);
zlim([-50,150]);
xlim([-7,7])
ylim([-2,31])
view(2)
time=(i-fmaxin)*5E-5;
file=num2str(time);
saveas(gcf,strcat('E:\March67TestsLondon\Dynamic\ImpactVis\',file,'.jpg' ));
view(3)
qz(isnan(qz)) = 0;
forcesimple=sum(SinglePointsensorforce);
volume=trapz(qx(1,:),trapz(qy(:,1),qz,1),2);
area = trapz(num(21:end-1,2),num(21:end-1,1))+trapz(num(1:20,2),num(1:20,1));
%plot(num(1:20,2),num(1:20,1),'x')
%plot(num(21:end-1,2),num(21:end-1,1),'-o')
forceint=volume/(area);
M(m) = getframe(gcf);
m=m+1;
end
movie(M,1)
movie2avi(M,'E:\March67TestsLondon\Dynamic\ImpactVis\impactfixedscale.avi', 'quality', 75,'fps',4)
```

Appendix M- MATLAB® Code for Piezoresistance Numerical Simulation

```
%%By John Van Tuyl- This code randomly assigns particle positions in a
%%matrix.  It then calculates distances between particles and the cost of
%%each distance wrt electrical resistance.  A shotest path algorith is used
%to determine the optimal path for the current.  A normal and/or shear
%strain can then be applied to see how the electrical reistance changes.

%%%%initializing
clear;
trial=1;
normalforce=0;
output=fopen('C:\Users\John VT\Documents\Sensor\Carbonsim\normaloutput.txt','w');

%%%%physical constants
h=6.626e-34;  %plancks constant
m= 9.109e-31; %electon m
e= 1.602e-19; %electron charge, coulombs; also conversion from eV to joule

%%%%sensor constants
d=500E-9; %conductive particle diameter, m
t=10*d; %film thickness
xdis=6*d; %x dist of sensor,
ydis=6*d; %y dist of sensor

%%%%Material Constants
omega=0.05; %eV, energy barrier to transfer .05 (Zhang)
effar=pi*((d/2)^2); %effective area
volfrac=.28; %.28 given (Khalandari)
YMPE=0.67E9; %compression modulus of polyethylene .67E9

%%%%Calculated Constants
numparticles=round(((xdis*ydis*t)*volfrac)/((4/3)*pi*(d/2)^3));
gam=(4*pi/h)*sqrt(2*m*omega*e);
A=((8*pi*h)/(3*effar*gam*(e^2)));

%%%%Simulation Considerations
maxforce=300000*xdis*ydis;
steps=5;
yshearstrain=0; %0.087488664; %5ish degrees
xshearstrain=0;
negdist=4*d; %checked 4
boundarydist=4*d;%checked 4

%%%%Scaling and Experimental
area=(xdis-(2*boundarydist))*(ydis-(2*boundarydist));
desiredarea=.0127*.0127; %%experimental area
factor=desiredarea/area;
```

```
fprintf('\nnumber of particles is %i\n', numparticles);
fprintf(output,'\n Area;Number of Particles; Volume Fraction; Length;Width;Height; Particle Diameter;
Negligible Distance for Particles; Negligible Distance for Edges; Random Range Used \n');
fprintf(output,'%d;%d;%d;%d;%d;%d;%d;%d;%d;\n\n', area,numparticles, volfrac, xdis, ydis, t, d,negdist/d,
boundarydist/d);
fprintf(output,' Force; Change in Total Resistance;\n');

for trial=1:100

%% Random Particle Position
%%%% preallocates matrices for speed
zo=sort(((t-d)*rand(1,numparticles))+(d/2));
yo=zeros(1,numparticles);
xo=zeros(1,numparticles);

%checks if there is overlap, if there is, it replaces the particle
i=1;
while i<=numparticles;
   yo(i)=rand*ydis;
   xo(i)=rand*xdis;
   for j=1:(i-1)
   if sqrt(((zo(i)-zo(j))^2)+((xo(i)-xo(j))^2)+((yo(i)-yo(j))^2))<d
   i=i-1;
   break
   end
   end
   i=i+1;
end

step=1;
%for yshearstrain=0:(yshearstrain/steps):yshearstrain
for normalforce=0:((maxforce)/steps):(maxforce)
normalstress=normalforce/(xdis*ydis);
normalstrain=normalstress/YMPE;
norm(trial,step)=normalstress;
yshear(trial,step)=yshearstrain;

z=zeros(1,numparticles);
y=zeros(1,numparticles);
x=zeros(1,numparticles);

anz=0;
any=0;
anx=0;
cax=0;
cay=0;
caz=0;

j=1;
```

```
k=1;
m=1;
l=1;

%%applies strains and calcualtes positions of conductors

for i=1:numparticles
z(i)=zo(i)*(1-normalstrain);
y(i)=yo(i)+((yshearstrain)*z(i));
x(i)=xo(i)+((xshearstrain)*z(i));

if y(i)>ydis
   y(i)=y(i)-ydis;
   yov(l)=y(i);
   xov(l)=x(i);
   zov(l)=z(i);
   l=l+1;
end

if x(i)>xdis
   x(i)=x(i)-xdis;
   yov(l)=y(i);
   xov(l)=x(i);
   zov(l)=z(i);
   l=l+1;
end

end

%makes anode points plotted yellow

w=1;
for i=1:length(z)

if z(i)<(negdist) && x(i)<(xdis-boundarydist)&& x(i)>boundarydist && y(i)<(ydis-boundarydist)&&
y(i)>boundarydist
anx(w)=x(i);
any(w)=y(i);
anz(w)=0;
w=w+1;
end

end

%makes cathode points plotted blue

p=1;
for j=1:length(z)
if z(j)>(t-negdist)
cax(p)=x(j);
```

```
cay(p)=y(j);
caz(p)=t*(1-normalstrain);
p=p+1;
end
end

%%builds full matrix

xd=[anx,x,cax];
yd=[any,y,cay];
zd=[anz,z,caz];

%% sets up matrices and finds distances and costs of all the pathways
%s=zeros(nchoosek(length(z),1),1);
%rm=zeros(nchoosek(length(z),1),1);
%node1=zeros(nchoosek(length(z),1),1);
%node2=zeros(nchoosek(length(z),1),1);
node1=0;
node2=0;
rm=0;
s=0;

k=1;
for i=1:length(zd);
   for j=i:length(zd);
      discen=sqrt(((zd(i)-zd(j))^2)+((xd(i)-xd(j))^2)+((yd(i)-yd(j))^2));
      s(k)=discen-d;

      if s(k)<=(negdist) && s(k)>0
      rm(k)=(A*s(k))*exp(gam*s(k)); %resistance
      node1(k)=i;
      node2(k)=j;
      k=k+1;
      elseif s(k)<=0
      rm(k)=0;
      node1(k)=i;
      node2(k)=j;
      k=k+1;
      else
      rm(k)=Inf;
      node1(k)=i;
      node2(k)=j;
      k=k+1;
      end

   end
end

costr=0;
P=0;
cost=0;
```

```
minpath=0;

%%shortest path set up and algorithm
start=1:length(anz);
stop=(length(zd)-length(caz))+1:length(zd);
V=[xd(:) yd(:) zd(:)]; %%all points
xy=[node1(:) node2(:) rm(:)]; %%nodes and cost
[costr,P] = dijkstramod(V,xy,start,stop);
[cost, minpath]=min(costr,[],2);

incostr=1./costr;
totres(trial,step)=sum(sum(incostr,2));
totres(trial,step)=totres(trial,step)^(-1);

h=figure('Position', [100, 100, 1049, 895],'visible','on');
[sx,sy,sz] = sphere;
hold on;
if l~= 1;
plot3(xov, yov, zov, 'om','MarkerSize',4);
end
%plot3(anx,any,anz,'g.');
%plot3(cax,cay,caz,'r.');
for i=start
   index=[P{i,minpath(i)}];
   plot3(xd(index),yd(index),zd(index),'c');
end
for i=start
index=[P{i,minpath(i)}];
lines=plot3(xd(index),yd(index),zd(index),'c','LineWidth', 1);
% fancy plotting
top=fill3([boundarydist xdis-boundarydist xdis-boundarydist boundarydist],[boundarydist boundarydist
ydis-boundarydist ydis-boundarydist],[0 0 0 0],'g','EdgeColor','none');
bot=fill3([0 0 xdis xdis], [0 ydis ydis 0], [t*(1-normalstrain) t*(1-normalstrain) t*(1-normalstrain) t*(1-
normalstrain)],'r','EdgeColor','none');
alpha(top,.01)
alpha(bot,.01)

for f=2:(length(index)-1)
if zd(index(f))~=0
carbpath=surf(sx*(d/2)+xd(index(f)),sy*(d/2)+yd(index(f)),sz*(d/2)+zd(index(f)),'FaceColor','magenta','Ed
geColor','none');
alpha(carbpath,.1);
end
end
end
for i=1:length(x)
carbs=surf(sx*(d/2)+x(i),sy*(d/2)+y(i),sz*(d/2)+z(i),'FaceColor','blue','EdgeColor','none')
alpha(carbs,.1)

end
```

```
%plot3(xd, yd, zd, 'g>','MarkerSize',3); %% turn me off with fancy plotting
view(3);
axis equal;
set(gca,  'fontsize', 20, 'FontName', 'Times')
%title(['Strain=' num2str(normalstrain)]);
ylim([0-d ydis+d]);
xlim([0-d xdis+d]);
zlim([0-d t+d]);
xlabel('X (m)','FontSize', 20, 'FontName', 'Times')
ylabel('Y (m)','FontSize', 20, 'FontName', 'Times')
zlabel('Z (m)','FontSize', 20, 'FontName', 'Times')
f =['C:\Users\John VT\Documents\Sensor\Carbonsim\figure\normala'  'X' num2str(yshearstrain) 'ysh'
num2str(normalforce) 'nrm.jpeg'];
saveas(h,f)
hold off
%close(h)
%clf;
%}
plots(step)=getframe(gcf)
%fprintf(output,'%d;%d;%d;%d;%d;\n',normalforce,yshearstrain,totres(trial,step),delt(trial,step),((1/totres(tr
ial,step))*factor)^-1);
fprintf(output,'%d;%d;\n', norm(trial,step),delt(trial,step));
step=step+1;
end
fprintf('trial number is %f\n', trial);
end
hold off
q=figure('Position', [50, 50, 1049, 895]);
hold on
%title(['Delta Resistance in relation to Normal Force']);
plot( mean(delt,1),mean(norm,1),'k','LineWidth',2)
ylabel('Pressure (Pa)','FontSize', 20, 'FontName', 'Times');
xlabel('R/R_o','FontSize', 20, 'FontName', 'Times');
%xlim([0 1]);
set(gca, 'FontSize', 20, 'FontName', 'Times', 'LineWidth', 2);
set(gca,'XMinorTick','on','YMinorTick','on','TickDir','out')
%set(gcf, 'PaperPositionMode', 'auto');
f =['C:\Users\John VT\Documents\Sensor\Carbonsim\figure\DeltaRvsNormalplot.pdf'];
%print(q,'-dpdf',f)
box on
set(gcf, 'PaperPositionMode', 'auto')
save('C:\Users\John VT\Desktop\normout.mat', 'norm','delt');
csvwrite('C:\Users\John VT\Desktop\normaltotres.txt',totres)
mean(norm,1)'
mean(delt,1)'
```